First MeerKAT HI Survey Results Mapping Large Scale Structures Hidden Behind the Milky Way out to $z = 0.08$

Nadia Steyn

Supervisor: Prof. Renée C. Kraan-Korteweg

Co-Supervisor: Dr. Bradley S. Frank

Department of Astronomy

University of Cape Town

Thesis presented for the degree of Master of Science in Astrophysics

September 2022

Abstract

SKA pathfinders (e.g., ASKAP and MeerKAT) are performing large HI surveys, surpassing previous-generation radio surveys in angular resolution, volume, and depth — going nearly two orders of magnitude deeper. The vast amount of data being produced by these telescopes creates a need for new tools and techniques, such as automated source-extraction. One particular science goal is to trace the large scale structure of galaxies in the local Universe behind the Zone of Avoidance (ZoA). This is difficult to do in the optical and infrared bands because of the thick dust and stellar crowding along the plane of the Milky Way. HI surveys are ideal because the 21 cm spectral line emission of neutral hydrogen (HI) atoms is unaffected by these features.

This dissertation presents two HI surveys in the ZoA: the MeerKAT16 Early Science project, conducted before the completion of the full array, with 16-dish subarrays and the ROACH-32k correlator; and later, the Galactic Plane Legacy Survey (GPS), a larger MeerKAT survey project utilising 60-dish subarrays and the SKARAB-4k correlator.

The motivation of the MeerKAT16 survey was two-fold: serving as a pilot project for the envisioned large MeerKAT64 Vela Supercluster (VSCL) survey; and a test-bed for optimising galaxy identification processes using automated pipelines. The survey aimed to map the rich galaxy cluster VC04, embedded in one of the prospective VSCL walls. We searched two mosaic cubes for HI sources by means of a deep visual search, and then using the Source Finding Application (SoFiA; version 1.3.2). The purpose of using both methods was to understand and optimise the SoFiA pipeline on real data, which is important for the development of source finding strategies for future large surveys. We catalogued 119 reliable galaxy detections (and an additional 37 candidates with lower certainty) within the early science data. SoFiA found galaxies all the way at the VSCL distance ($V_{\rm hel} \approx 18\,000$ km s^{-1}), where we detected hints of two walls, and HI deficiency in the centre of VC04.

GPS surveyed a long narrow strip ($|b| \lesssim 2^\circ$) along the Galactic plane, with the aim of penetrating the most obscured part of the ZoA. A segment of the data spanning $302^\circ \leq \ell \leq 332^\circ$ was reduced, imaged, and analysed as part of this project. This region is

interesting because it encompasses the Great Attractor (GA) — a massive overdensity highly influential to the local flow of galaxies. Aided by the newer version of SoFiA (v2.3.1), we found 477 galaxy candidates, most of which are new discoveries, and performed an in-depth comparison against the largest systematic HI survey covering the *southern* ZoA up to this point — the Parkes HIZOA survey. Additionally, we compared our results to simulations that follow the method used for the SKA HI science case. The GPS redshift distribution reveals a striking overdensity at the GA distance ($V_{\rm hel} \approx 4000\,{\rm km\,s^{-1}}$), inconsistent with a uniform galaxy distribution, whereas the high-redshift end is more underdense than predicted by the simulation.

These deep interferometric HI surveys provided a new glimpse of highly interesting structures crossing the Galactic plane, demonstrating that large scale structure can be mapped even in the deepest part of the ZoA. The success of MeerKAT16 and GPS is a preview of the HI science potential of the upcoming SKA, which will surpass MeerKAT in depth, sensitivity and resolution.

Dedications

A dissertation is not made through the efforts of only one individual, and this work is no exception. I take this opportunity to acknowledge the people who helped me in some way (big or small) during this journey.

Thank you very much to my supervisors Prof. Renée Kraan-Korteweg and Dr. Bradley Frank for getting me through to the finish line. I also sincerely thank my colleagues: Hao Chen, Sambatriniaina Rajohnson, Sushma Kurapati, Vineshree Pillay and Wanga Mulaudzi. Each of you lended me support at some point during the past couple of years.

I am also grateful for our collaborators Paolo Serra, Thijs van der Hulst, Tobias Westmeier and Lister Staveley-Smith for their useful input. I also need to thank the team at Ilifu, who patiently answered my many technical questions.

I gratefully thank my parents for awarding me the privilege to pursue tertiary education in any field I desired. Without their support I would not be in a position to do a Masters degree.

A massive thank you to Trystan Lambert, who selflessly guided me into this scary new role when I felt totally lost. This especially applies to the beginning phase when the Covid pandemic arrived and I could no longer go to campus (only a few short weeks after registration). Without Trystan getting me up to speed with everything, encouraging me and being my unofficial tutor, I can easily imagine a reality where I did not continue with this venture. Thank you, thank you, thank you.

I need to thank Prof. Renée Kraan-Korteweg again, because thanking her once is not enough. A quick search of my inbox uncovers close to 500 emails from her to me. Additionally, I estimate about 100 hours of Zoom meetings. I could not have asked for a more attentive, patient, dedicated, knowledgeable and inspiring supervisor. I will always be grateful for the mentorship.

Author's declaration

I hereby declare that the work in this dissertation is my own, except where indicated by specific reference in the text and that it has not been submitted for any other academic award. Work done in collaboration with, or with the assistance of others, is indicated as such. Any views expressed in the dissertation are those of the author.

SIGNED: Signed by candidate ..... DATE: 31/01/2023 .....

Table of Contents

List of Tables

Table **Page**

List of Figures

Figure **Page**

Chapter 1

Introduction

Astronomical observations of radio sources, in their huge variety, contribute greatly to our knowledge of the Universe on the largest scale. A complete whole-sky map of galaxies is needed in order to test our current model of the Universe, but the region of sky obstructed by the Milky Way is still largely unpopulated.

This thesis aims to unveil the large scale structure along the southern Galactic plane using HI data from the MeerKAT[1] radio telescope. The data presented in this dissertation allow us to probe volumes ($z \leq 0.08$) that have thus far been out of reach. We find HI sources in spectral line data cubes using a combination of visual searching and automated source finding, and the resulting maps uncover structures in astounding detail.

1.1 A Large Scale Perspective

In the past astronomy was dominated by optical observations, representing only a small window of the electromagnetic (EM) spectrum. Through the years scientific breakthroughs have opened up the entire EM spectrum to astronomical exploration, including the radio band from at least as far back as the 1960's; the first major extragalactic milestone being the discovery of the Cosmic Microwave Background (CMB) radiation by Penzias & Wilson (1965).

[1]For more information and the latest MeerKAT developments, see https://www.sarao.ac.za/science/meerkat/

Radio astronomy has matured along with technology, and the current generation of radio telescopes, sensitive to very weak radio signals, are recording radio phenomena in ever-more detail.

In the nineteenth century, John Herschel was the first to describe "large scale structure" of galaxies when he reported in his *General Catalogue of Nebulae* (Herschel, 1864) that a third of the "nebulae" are concentrated in the Virgo constellation, which subtends only an eighth of the area of the sky (Fairall, 1998). He also made the important distinction between the stars in our galaxy, the Milky Way, and the extragalactic "island Universes", that we now call galaxies. The Virgo concentration of galaxies has since been established as the Local Supercluster; a gravitationally bound structure of groups and filaments of galaxies centred around the Virgo cluster, according to de Vaucouleurs (1958).

Over the many decades that followed, more sensitive equipment has allowed for more nearby superclusters and large scale structures to be mapped, giving us a much more complete picture of the local Universe. A few of the superclusters relevant to the southern sky will be discussed in detail in this dissertation: in particular the Vela Supercluster and the Norma Supercluster (also called the Great Attractor) — both partially hidden in the Zone of Avoidance (ZoA).

1.2 The Zone of Avoidance

Richard Proctor (Proctor, 1878) showed that the plane of the Milky Way coincided with a "zone most avoided by nebula" when he produced plots of Herschel's *General Catalogue*. At the time, the reason for the observed absence of nebulae near the Galactic plane was not yet understood and opposing theories were still being debated.

The apparent absence of extragalactic objects in the Galactic plane was officially determined by Trumpler (1930) to be caused by dust obscuration. As the Galactic plane ($\ell = 0°$) is approached, dust obscuration and foreground stars in the Milky Way make objects behind it appear fainter and smaller. Accordingly, the inner $b \sim \pm 15°$ of the Galactic plane became known as the Zone of Avoidance (ZoA) among astronomers — allegedly coined by Edwin Hubble (Jakiel, 2000).

Our galaxy is a system of stars and interstellar dust and gas in the shape of a disk with spiral arms. Figure 1.1 shows the Earth's point of view from inside the disk. The stars are predominantly spread out in a thin band across the sky, concentrated in a bulge at the centre. Optical light emanating from behind the Galactic centre $(\ell,\ b) = (0°, 0°)$ is fully obscured behind the curtain of the Milky Way.

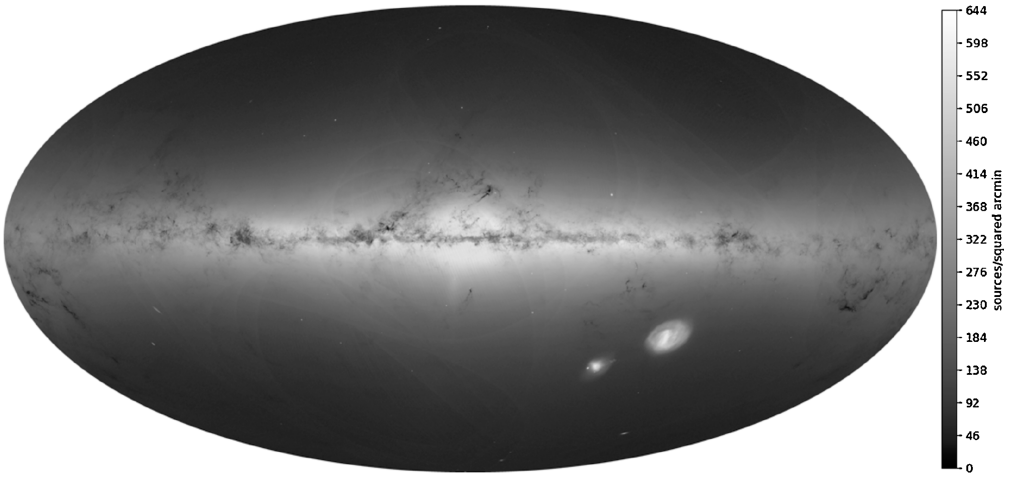

Figure 1.1: All-sky star density map of the Milky Way of the second Gaia data release (DR2). The astrometric data is presented as an equal-area (Hammer) projection in Galactic coordinates — where the Galactic plane runs along the central horizontal axis. Each pixel represents ~5.9 arcmin^2. The shading indicates the number of sources per arcmin^2, in logarithmic scale. The bright patches in the lower right quadrant are the Small and Large Magellanic Clouds. Image created by the Gaia Data Processing and Analysis Consortium (DPAC)[2].

In reality the Galactic plane is not sparsely populated, but detecting galaxies behind the heavy obscuration is a challenge. However, an accurate whole-sky map of galaxies is essential for understanding the dynamics in the local Universe.

1.2.1 Surveying the ZoA in Various Wavelengths

Over the last several decades, astronomers have made substantial progress in narrowing the ZoA through the use of dedicated surveys at various wavelengths (optical, near infrared, far infrared, radio and X-ray), but several technical challenges remain.

Optical surveys are surface-brightness limited. Only the intrinsically largest and brightest galaxies can be detected behind the thick dust walls surrounding the Galactic plane. Even though deep optical surveys have achieved a reduction of >50% in the impact of the optical ZoA (Kraan-Korteweg et al., 1995; Woudt & Kraan-Korteweg, 2001; Kraan-Korteweg, 2005), the optical ZoA still takes up about 20% of the whole-sky map (Kraan-Korteweg, 2005).

Infrared (IR) radiation has longer wavelengths than optical light and can travel through interstellar clouds of dust and gas while suffering less scattering and absorption. However, low Galactic latitudes are heavily crowded with foreground stars which emit their own

radiation. As the Galactic plane is approached, the surface density of stars increases exponentially, leading to a rise in background confusion noise (Jarrett et al., 2000) and making it increasingly difficult to discern the faint light of galaxies. The astrometry data in Fig. 1.1 (collected by the Gaia[3] spacecraft between July 2014 and May 2016) illustrate the "stellar crowding", as well as the trail of dust that accompanies the disk of stars.

The increased stellar density obscures about 10% of the sky according to data from the IRAS Point-Source Catalog (Kraan-Korteweg & Woudt, 1999; Woudt & Kraan-Korteweg, 2001). IRAS (a far-infrared survey) has greatly contributed to filling-in galaxies in the ZoA (e.g., Takata et al., 1996; Saunders et al., 2000), and with the addition of follow-up redshift measurements several connections across the ZoA could be mapped, including Perseus-Pisces, Puppis, Hydra, Centaurus and Norma (Kraan-Korteweg & Woudt, 1999). For an indication of the on-sky positions of these structures, see Fig. 1.2: an Aitoff projection (showing the entire celestial sphere) in Galactic coordinates (lines of longitude and latitude defined with respect to the shape of our galaxy) of the 2MRS source catalog up to redshifts of $z = 0.08$.

The most complete magnitude limited, whole-sky redshift survey is the 2MASS Redshift Survey (2MRS) which used the 2 Micron All Sky Survey (2MASS) extended source catalog (2MASX) as an input mask (Huchra et al., 2012; Macri et al., 2019). 2MASX contains 1.65 million galaxies and other extended sources with magnitudes $K^o < 14$, reaching as close as $5^\circ \leq |b| \leq 8^\circ$ to the Galactic plane, where the completeness drops to $K^o \lesssim 13.5$. 2MRS measured the redshifts of galaxies drawn from 2MASX, with extinction-corrected magnitudes of $K^o < 11.75$, resulting in about 44 000 redshifts (Macri et al., 2019).

Near-infrared (NIR) radiation is the most sensitive to elliptical galaxies, therefore projects such as 2MASS and the Deep Near-Infrared Survey (DENIS; Epchtein et al., 1997) can be complementary to surveys conducted in other parts of the spectrum (such as radio wavelengths). IR is a useful window for extragalactic studies and, compared to optical maps, 2MRS is deeper and unbiased by the patchy distribution of dust, but even this catalog becomes increasingly incomplete towards the Galactic plane (evident in Fig. 1.2).

Rich galaxy clusters tend to be strong X-ray emitters, and luckily the Milky Way is transparent to X-rays above 0.5 – 2.0 keV (Kraan-Korteweg & Woudt, 1999; Ebeling et al., 2002). These X-rays are an optimal window for searching for clusters near the ZoA, especially cores of clusters that have been stripped of gas or that exist predominantly of elliptical galaxies. Therefore, X-ray surveys do not duplicate the results of surveys that

[3] https://www.cosmos.esa.int/web/gaia

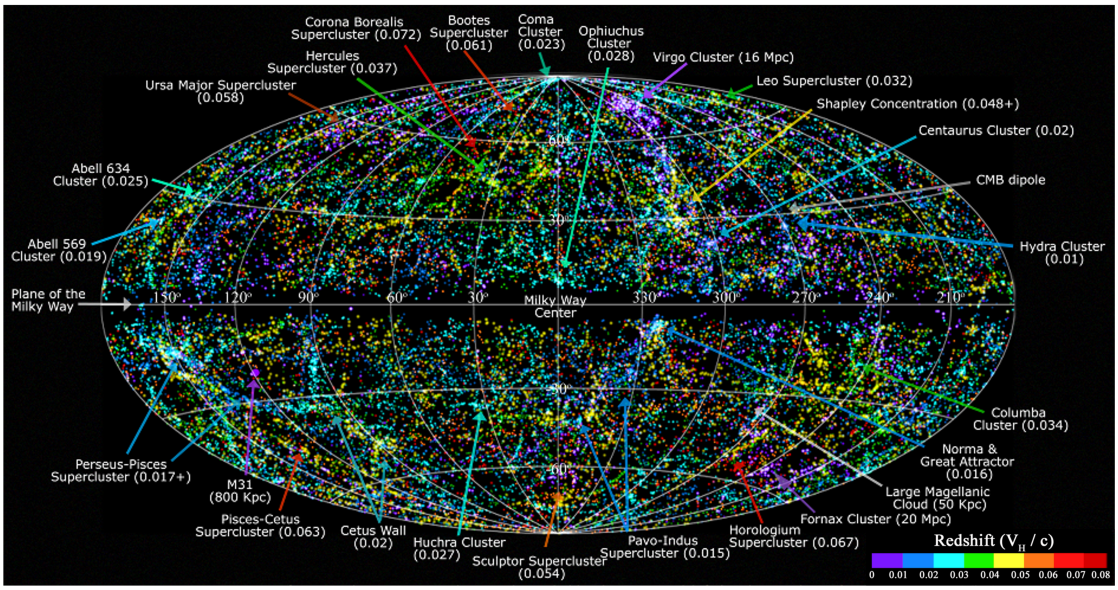

Figure 1.2: All-sky Aitoff projection in Galactic coordinates of 2MASS galaxies, colour-coded by the 2MRS redshift (Huchra et al., 2012), with arrows indicating positions of galaxy clusters and superclusters. [Image by T. Jarrett]

measure gas content; they complement them.

Several successful all-sky surveys ($|b| > 20°$) have been completed in the softer X-ray band $0.1-2.4\,\mathrm{keV}$, for instance the HEAO-1 (also known as Einstein) survey (Wood et al., 1984), the ASCA Galactic Plane Survey (Yamauchi et al., 2002), and the ROSAT All Sky Survey (Ebeling et al., 2000). The ROSAT All Sky Survey classified the Norma cluster/A3627 (discussed in Sect. 1.6.2) as the sixth brightest X-ray cluster in the sky (Boehringer et al., 1996).

The Clusters in the Zone of Avoidance (CIZA) survey was the first systematic search at low Galactic latitudes for clusters in the $0.1-2.4\,\mathrm{keV}$ band, using the ROSAT Bright Source Catalogue (Voges et al., 1999) to select initial targets (Kocevski et al., 2004a,b). Prior to CIZA, $|b| \lesssim 20°$ was avoided because the increasing hydrogen column density creates an "X-ray ZoA".

Deep surveys in the hard X-ray band (above $2-3\,\mathrm{keV}$) only debuted later due to technological limitations. Two powerful X-ray observatories currently operating are the Chandra X-ray Observatory and the European Space Agency's X-ray Multi-Mirror Mission-Newton (XMM-Newton) Space Observatory (Brandt & Yang, 2021). These deep extragalactic surveys are the most sensitive X-ray surveys yet and have revolutionised cosmic X-ray background surveys in the $0.5-10\,\mathrm{keV}$ band.

Surveys with X-ray satellites such as these are excellent tools for unveiling cores of clusters, and considerable multi-wavelength follow-up observations have been pursued on X-ray sources (Brandt & Hasinger, 2005), however, even if more clusters can be located, it is very difficult to measure corresponding redshifts if the galaxies are at extinction levels $A_B \gtrsim 3^m$ (Kraan-Korteweg, 2005).

Obtaining a uniform sample of redshifts in the ZoA is crucial for calculating velocity flow fields of structures behind the ZoA and resolving bulk-flow discrepancies. While optical and IR light are perturbed by the dust and stars in the ZoA, radio wavelengths (~1 mm–10 m) can pierce through this region. In particular, we can measure the 21 cm wavelength radiation emitted by galaxies rich with HI (explained in detail in Sect. 1.4).

1.3 Velocity Flow Fields

In the early twentieth century, Edwin Hubble showed that the distance to an object is linearly proportional to the speed with which it is moving away from us, i.e., its velocity of recession (Hubble, 1929). Soon after this discovery, cosmologists inferred this to be the expansion of the Universe: distances between galaxies are ever increasing because the volume of space containing them is constantly growing. This linear relation is the now famous Hubble Law: $V = H_0 d$, where V is the velocity due to the expansion of the Universe (in $\mathrm{km\,s^{-1}}$), d is the physical distance in Megaparsecs (Mpc) and H_0 is the Hubble constant (taken as $70\,\mathrm{km\,s^{-1}\,Mpc^{-1}}$)[4].

Recessional velocities are often calculated by means of their redshift (z): the spectra of the galaxy is proportionally displaced (Doppler shifted) towards longer wavelengths if the motion is directed away from our local rest frame; or towards shorter wavelengths (blueshifted) if the motion is towards us. Redshift is related to the recessional velocity by the expression $V = cz$ (for non-relativistic velocities). Throughout this dissertation we use the heliocentric velocity convention: the radial velocity relative to the Sun, denoted V_{hel}.

When we can obtain the spatial coordinates as well as the corresponding redshifts, we can describe large scale structure of galaxies as a distribution of points in "redshift space", where the line-of-sight components are the radial velocities (or measured redshifts).

[4]The Hubble constant is taken to be $70\,\mathrm{km\,s^{-1}\,Mpc^{-1}}$ throughout this dissertation in agreement with the standard ΛCDM cosmological model.

1.3.1 Peculiar Velocities and Bulk Flow

The Hubble flow is not the only contribution to the motion of galaxies. In addition to the cosmological velocity of expansion, groups or clusters can be pulled in the direction of strong gravitational potentials. This "peculiar" motion is an additional component of radial motion which, in combination with the Hubble flow, makes up the observed velocity. Therefore, a more accurate expression for recessional velocity is $V = H_0 d + V_{\rm pec}$, where $V_{\rm pec}$ is the component of the peculiar velocity vector along the line-of-sight. Motion perpendicular to our line-of-sight can not be observed directly[5].

For galaxies within close range of the Milky Way, it is possible for $V_{\rm pec}$ to dominate the smooth expansion of the Universe, and at high redshifts the $V_{\rm pec}$ component becomes much smaller than the velocity cause by the Universe's expansion. In order to derive the peculiar velocity of a galaxy, an independent distance measurement is needed. Two reliable techniques are the Tully-Fisher relation for spiral galaxies (Aaronson et al., 1982) and the modified Faber-Jackson relation for elliptical galaxies (Lynden-Bell et al., 1988). From this distance measurement, we can infer the cosmological velocity. Then, comparing this to the observed velocity leads to the peculiar motion of the galaxy.

Peculiar motions (or cosmic flow fields) are interrelated with large scale structure, because (by definition) peculiar motion stems from the non-uniform distribution of mass. Peculiar velocities can thus be considered as a tracer of the underlying mass density in the Universe.

1.3.2 The Peculiar Motion of the Local Group

The Cosmic Microwave Background (CMB) plays a key role in the context of measuring bulk motions because, due to its nature, it can be defined as a rest frame. Accurate measurements of the CMB radiation have determined that our Local Group of galaxies (three large galaxies and about 100 dwarf galaxies) is moving at $V_{\rm pec} \simeq 631 \pm 20\,{\rm km\,s^{-1}}$ with respect to the CMB, in the direction of Centaurus, $(\ell,\ b) \simeq (276^\circ,\ 30^\circ)$ (Hoffman et al., 2017; Lavaux et al., 2010; Kogut et al., 1993). The relative movements among the galaxies surrounding the Local Group are much smaller, implying they must also be moving in this direction. Therefore there is a large scale streaming in effect, which has to be fueled by one or more relatively nearby sources of gravity.

[5]Note, if an object moves at a relativistic velocity, then its velocity component perpendicular to the line-of-sight will result in an observable redshift, because the relativistic Doppler effect does have a transversal component — however, it is difficult to separate out the different components.

The infall towards the Virgo cluster in combination with the apparent repulsion from the our closest void — termed the Local Void — constitutes about 50% of this movement (Tully et al., 2019). Astronomers are looking out to further and further distances to account for the rest of the motion. The next most influential masses are the Shapley Supercluster and the Great Attractor. The Shapley Supercluster is the largest concentration of galaxy clusters out to $200\,h^{-1}$Mpc (Lavaux & Hudson, 2011), although at $cz \approx 15\,000\,\mathrm{km\,s^{-1}}$ (Kocevski et al., 2005) it is located about three times further than the Great Attractor.

Which of the two have the greatest influence is still a topic of debate, in part because the Great Attractor is not fully mapped. Secondly, it is difficult to decouple Shapley's influence from the flow towards the Great Attractor (Lucey et al., 2005). Moreover, there is growing evidence that the Great Attractor itself is moving in the direction of Shapley (Kocevski et al., 2007; Hoffman et al., 2017; Hudson et al., 2004). The model by Smith et al. (2000) shows that these two attractors contribute equal amounts to the Local Group's peculiar velocity. For different theories see, e.g., Hudson et al. (2004), Kocevski & Ebeling (2006), Bolejko & Hellaby (2008).

Tallying the attractions toward known structures in the surrounding redshift space, about 150 $\mathrm{km\,s^{-1}}$ of our Local Group's peculiar velocity remains unaccounted for (Springob et al., 2016). Table 5 in Scrimgeour et al. (2016) shows various bulk flow measurements from literature along with the radius of the volume that was analysed. The source (or sources) responsible for the residual bulk flow is still controversial, but later results point towards a sizeable mass excess behind the southern Galactic plane at $\ell = 270° - 330°$, just beyond the reach of recent whole-sky redshift surveys ($\sim 15\,000 - 16\,000$ $\mathrm{km\,s^{-1}}$; Kraan-Korteweg et al., 2016; Hoffman et al., 2015; Boruah et al., 2020). The Vela Supercluster (VSCL), identified in this region of sky at $cz \approx 18\,000\,\mathrm{km\,s^{-1}}$, was recently determined to contribute $V_{\mathrm{LG}} \geq 50\,\mathrm{km\,s^{-1}}$ to the motion of the Local Group (Kraan-Korteweg et al., 2017), adding another piece to the puzzle, although its full extent is still unknown.

Further clarity will come from building a comprehensive three-dimensional map behind the ZoA, including the Great Attractor region and the VSCL region. Fortunately, HI radiation emitted by galaxies embedded in these structures can travel through the ZoA unhindered and are perceptible by radio telescopes on Earth.

1.4 Probing the ZoA in HI

One of the best-studied radio waves is the spectral line emission from neutral hydrogen (HI). The 21 cm HI line was first detected within our galaxy by Ewen & Purcell (1951)

and first used as an extragalactic probe by Kerr & Hindman (1953) to detect HI emission from the Magellanic Clouds. In the first systematic search for galaxies in the ZoA, Kerr & Henning (1987) demonstrated that optically invisible galaxies near the Galactic plane can be readily detected through their 21 cm HI emission, if the galaxies are rich in neutral hydrogen.

The 21 cm line is an excellent tracer of gas-rich galaxies, and the majority of galaxies detected in HI tend to be star-forming galaxies — which are rich with HI gas because hydrogen is the raw fuel for star formation (e.g., Schmidt, 1959; Maddox et al., 2021).

1.4.1 The 21 cm Spectral Line

Atomic hydrogen is the simplest element, consisting of a single proton with an electron in orbit about it. In the atom's lowest energy state, the proton and the electron have their spins (a quantum property) lined up antiparallel to each other. Atoms can enter an excited energy state (usually through collisional excitation) where the electrons' spin is flipped so that the two spins line up parallel: pointing in the same direction. When the spin of the electron flips back to its original orientation, a photon is released with energy $5.87\,\mu$eV, corresponding to a frequency of 1420.405752 MHz, or a wavelength of ~21 cm, which falls in the radio spectrum (~1 cm – 1 km).

This drop from the high energy state to the low energy state, called a "spin-flip" transition, is extremely rare; a spontaneous decay occurring once every 1.1×10^7 years (Field, 1958). Furthermore, the HI emission line is intrinsically faint. Fortunately, because of the abundance of hydrogen atoms in the Universe combined with frequent collisions, enough spin-flip transitions occur in the interstellar medium to be detectable from Earth using sensitive receivers.

Radio telescopes measure HI radiation with a multi-channel receiver, where each channel is tuned to a slightly lower frequency (longer wavelength), and records signals simultaneously. After a set integration time, the data gathered by the telescope are converted into a digital "data cube"; a cube of three-dimensional pixels where the x and y axes represent on-sky position and the spectral channels form the z-axis, which corresponds to frequency. When searching the data cube for emission lines, each of the spectral channels (z channels) represent a higher redshift (or further distance). Source finding can be carried out by eye or through the help of automated source finders (explained in Chapter 2).

HI surveys offer many unique advantages. They allow astronomers to peer through dust obscured regions — even the most opaque part of the ZoA — unbiased by the foreground

extinction (Kraan-Korteweg, 2005). Another major advantage of emission line astronomy is that redshift and rotational velocity information (cf. Sect. 2.3) can be immediately extracted (Kraan-Korteweg et al., 2003).

In terms of extragalactic research, systematic HI surveys can contribute significantly towards many closely related topics in cosmology. HI is an excellent environmental tracer, and it is known that galaxy formation and evolution differs in dense regions compared to voids (e.g., Giovanelli & Haynes, 2015). Furthermore, new information can be compared to current cosmological models of the Universe, for example, by putting constraints on the cosmological parameter Ω_0 (Kraan-Korteweg & Lahav, 2000; Macri et al., 2019). Knowledge of the distribution of mass and velocity fields are also tracers of dark matter, since peculiar velocities arise from the combined distribution of all matter — luminous and dark matter (Macri et al., 2019; Boruah et al., 2020).

1.4.2 Limitations and Difficulties of HI surveys

HI surveys are affected by a number of systematic issues. Being sensitivity or flux limited, there is normally a bias towards detecting objects with more HI (at a given z) — therefore a bias towards gas-rich galaxies. This indirectly gives rise to a dependence on morphological type, specifically an observational bias towards spiral galaxies, HI rich dwarfs and groups, but not ellipticals or cores of dense clusters. This can be remedied by combining HI data with complementary surveys; for example, NIR observations are sensitive to early-type galaxies and large clusters (Kraan-Korteweg, 2005) and X-ray surveys can measure hot gas in rich galaxy clusters.

Frequency dependent artifacts in the spectral line cubes can arise from several processes — e.g., unmodelled radio continuum emission or radio frequency interference (RFI): either from satellites, man-made terrestrial emission, or solar RFI. Real data is likely to have at least some artifacts, and careful subtraction is required during the data reduction phase. The larger and more sensitive the survey, the more difficult this procedure becomes. These issues are explored in more detail in Chapter. 4.

The Milky Way has its own HI gas that dominates the spectral line emission at $z = 0$ ($\sim$1420.4 MHz) in a spectral line data cube. When the focus of a survey is extragalactic objects, the starting frequency is usually set at $\sim$1419.5 MHz (or $V_{\rm hel} \approx 200\,{\rm km\,s^{-1}}$) because it can be tricky to separate out Galactic gas velocities and nearby HI galaxies, especially in lower resolution data.

Besides the well-known factors mentioned above, of which to remain cautious, HI surveys suffer no other selection effects (Kraan-Korteweg et al., 2008b).

The previous generation of HI surveys were limited by high rms and low spatial resolution — especially in the case of single-dish telescopes — and as a result have been quite shallow (Kraan-Korteweg et al., 2008b). Going deeper at these resolutions would only lead to confusion problems; sources close together would not be resolved due to the large beam size.

The Square Kilometre Array (SKA) precursor arrays[6] offer a wider instantaneous bandwidth, and a much improved spatial resolution, for instance, compared to the HI Zone of Avoidance survey (HIZOA; Staveley-Smith et al., 2016) conducted with the 64 m Parkes telescope and a beam size of $15.5'$ (discussed in detail in Chapter 4). The higher sensitivity that was required is now achievable. For example, the 60-dish MeerKAT configurations used for the Galactic Plane Legacy (GPS) survey (analysed in Chapter 4) are predicted to reach an rms sensitivity of $\sim$0.3 mJy beam^{-1}. This is considerably lower than HIZOA, where the sensitivity was limited by a 6 mJy beam^{-1} rms.

1.5 SKA Pathfinders

The next generation of radio telescopes (e.g., the SKA pathfinders) will exploit advances in technology and computing capacity to achieve parameter space and redshift ranges that were previously unattainable (Maddox et al., 2021). Several precursors and pathfinders to the SKA already have HI surveys underway, for example, the Widefield ASKAP L-band Legacy All-sky Blind surveY (WALLABY; Koribalski et al., 2020; Koribalski, 2012). The Australian SKA Pathfinder (ASKAP; Johnston et al., 2008) has launched a new receiver design that covers a field of view of 30 deg^2, allowing WALLABY to survey the entire southern sky with superior spectral sensitivity and spatial resolution compared to the existing HI Parkes All Sky Survey (HIPASS; Barnes et al., 2001; Koribalski et al., 2004; Meyer et al., 2004) data (Maddox et al., 2021).

The South African SKA pathfinder array, MeerKAT, situated in the Northern Cape of South Africa, will form part of the international SKA, an endeavour to build the largest radio telescope in the world (Driessen, 2020).

[6] A precursor was defined by the SKA Science and Engineering Committee as a telescope on one of the SKA candidate sites, carrying out SKA-related science and operations.

1.5.1 MeerKAT

The MeerKAT interferometer, currently the most sensitive centimetre-wavelength radio telescope in the southern hemisphere (Booth & Jonas, 2012), is a precursor for the SKA1-mid array, which will survey the mid-frequency band of 350 MHz – 15.3 GHz. Including MeerKAT, the SKA phase 1 array will have a total of 197 dishes in South Africa, with baselines up to 150 km.

MeerKAT consists of 64 offset Gregorian dishes, each 13.5 metres in diameter (Booth & Jonas, 2012). The maximum baseline is 8 km, with 70% of the elements situated within a 1 km core. The dense central configuration gives excellent sensitivity, making MeerKAT ideal for imaging extended emission, meanwhile the longer baselines produce high resolution.

MeerKAT and the other SKA pathfinders (ASKAP, MWA and HERA) are already hitting new milestones in radio astronomy, exceeding past interferometers in sensitivity by an order of magnitude. Scheduled to be operational in the mid 2020's, the SKA phase 1 array will increase sensitivity by yet another order of magnitude (Weltman et al., 2020).

Exploring the structures hidden behind the veil of the Milky Way are now feasible with MeerKAT's dedicated HI surveys and open call proposals. MeerKAT has recently completed observations for the GPS HI survey (see Chapter 4) and has several ongoing large survey projects investigating the HI content in galaxies, including the MeerKAT International GHz Tiered Extragalactic Exploration Survey (MIGHTEE; Jarvis et al., 2016; Maddox et al., 2021) and Looking At the Distant Universe with the MeerKAT Array (LADUMA; Blyth et al., 2016).

1.6 Structures in the ZoA Surveyed with MeerKAT

The centre of the ZoA is fully transparent in the L-band, and HI surveys have proven the most effective at tracing gas-rich galaxies in the heaviest dust-obscured and star-crowded regions (Kraan-Korteweg et al., 2002). By chance, some of the largest mass concentrations in the local Universe ($z \approx 0$) lie behind the ZoA (Macri et al., 2019). This dissertation focuses on two of these dynamically important structures: the Vela Supercluster (VSCL) and the Great Attractor (GA).

1.6.1 Vela Supercluster

Spectroscopic observations of a series of clusters in the constellation of Vela were obtained with the Southern African Large Telescope (SALT) between 2012 and 2014, followed

by further spectroscopy with AAOmega+2dF on the Anglo-Australian Telescope (AAT; Kraan-Korteweg et al., 2015). These several thousand measurements confirmed the existence of a previously unknown supercluster, partially obscured by the ZoA (Kraan-Korteweg et al., 2017). The massive ~25°×20° overdensity, named the Vela Supercluster (VSCL), extends across the ZoA, appearing most prominently in the region $(\ell,\ b) = (285° - 255°,\ \pm 10°)$ at a mean redshift of $\sim 18\,000\,\mathrm{km\,s^{-1}}$ (Kraan-Korteweg et al., 2015, 2017).

An analysis of the bulk flow was performed in 2019, using the peculiar velocities from the unobscured data in the vicinity of the supercluster, which re-confirmed the existence of the massive and dynamically significant VSCL (Courtois et al., 2019). The contribution of this superstructure to the Local Group's velocity (according to a rough calculation based on linear perturbation theory) is estimated as $V_{\mathrm{LG}} \simeq 50\,\mathrm{km\,s^{-1}}$, as mentioned in Sect. 1.3.2.

The main features of VSCL are two wall-like structures — one at $V_{\mathrm{hel}} \approx 18000\,\mathrm{km\,s^{-1}}$, and one at higher redshifts — which appear to be merging into one wall in the central ZoA (Kraan-Korteweg et al., 2017). This multi-branching morphology — characteristic of a large supercluster — will be explored in-depth in the upcoming MeerKAT64 VSCL survey.

The core of the VSCL has remained uncharted, since optical spectroscopy is ineffective at the most obscured part of the ZoA. To penetrate the thick dust column density and obtain an estimate of the mass of VSCL, we need systematic HI surveys. A pilot project was pursued with MeerKAT as an early science commissioning project (Kraan-Korteweg et al., 2016) to confirm if a larger survey would be feasible on reasonable timescales. Referred to as the MeerKAT16 Early Science Project, HI data were captured around the newly identified galaxy cluster VC04, residing within the main wall of VSCL (Kraan-Korteweg et al., 2017). The analysis of this survey is presented in Chapter 3.

1.6.2 The Great Attractor

While VSCL is a recent discovery, the Great Attractor (also called the Norma Supercluster) became apparent to Dressler et al. (1987) through a study of the peculiar velocities of ~400 elliptical galaxies, when the results showed a large scale infall towards a mysterious gravitational potential. The galaxies in the sample seemed to be flowing towards $(\ell,\ b,\ V) \approx (307°,\ 9°,\ \sim 4350 \pm 350\,\mathrm{km\,s^{-1}})$ (Lynden-Bell et al., 1988).

Several dedicated galaxy searches have been done around the GA region in an attempt to learn more about this gravitational anomaly, including radio, optical, NIR, FIR and X-

ray observations (for a review see Kraan-Korteweg & Lahav, 2000), and various interlinked structures and filaments have been uncovered.

Kraan-Korteweg et al. (1996) argued that the prominent Norma cluster (A3627) at (ℓ, b, V) = (325°, -7°, ~4882 km s^{-1}) likely marks the bottom of the potential well of the Great Attractor, and forms part of a much larger "great-wall" structure. The Norma cluster was first discovered through visual examination of film copies of sky surveys (Abell et al., 1989). A subsequent deep optical search for partially obscured galaxies recorded >4000 galaxies within ($318° \lesssim \ell \lesssim 340°$; $|b| \leq 10°$; Woudt et al., 1999). Redshifts could be obtained for a fraction of this sample; resulting in the addition of 265 new velocities to literature, where only 44 had been previously recorded in this region. The Norma cluster was also independently confirmed to be an X-ray bright cluster by ROSAT observations (Boehringer et al., 1996).

A blind HI survey in the southern ZoA with the Parkes radio telescope (discussed in detail in Chapter 4) began in 1997 (running for several years) and results were analysed at various stages (e.g., Henning et al., 2000; Juraszek et al., 2000). These HIZOA observations were done in parallel with the (shallower) HIPASS survey (Meyer et al., 2004), which surveyed declinations -90° to 25° at an rms of 13 mJy. Results from the Parkes multi-beam surveys (HIPASS and HIZOA) have uncovered over four thousand galaxies (Meyer et al., 2004; Staveley-Smith et al., 2016), making the biggest contribution towards mapping galaxies in the GA region in the southern ZoA. Both HIPASS and HIZOA also have extensions to the north (HIPASS-NE and HIZOA-NE; Wong et al., 2006; Donley et al., 2005, respectively).

The emerging, general view of the GA is that it is a very extended region ($\sim 40° \times 40°$) of moderately enhanced galaxy density centred on (ℓ, b, V) ≈ (320°, 0°, 4500 km s^{-1}), stretching both above and below the Galactic plane (Kolatt et al., 1995; Kraan-Korteweg, 2005; Radburn-Smith et al., 2006; Staveley-Smith et al., 2016). Although there is a broad consensus, the core of the GA is still uncharted and more detailed mapping is needed.

1.6.3 Related Structures

Even superclusters are not gravitationally isolated from each other and it is therefore imperative to mention other major clusters along $\ell \sim 270° - 360°$, which will form part of the overall discussion.

Just above the Galactic plane at (ℓ, b, V) ≈ (306°, 6°, 6200 km s^{-1}) sits the Centaurus-Crux cluster, suspected to form part of the GA overdensity (Woudt & Kraan-Korteweg, 2001). Also found at higher latitudes is the Centaurus cluster at ≈ (302°, 22°, 3418 km s^{-1} ;

Woudt et al., 2008), the Hydra cluster at ≈ (267°, 27°, 3777 km s^{-1} ; Woudt et al., 2008) and the Ophiuchus cluster at ≈ (0.5°, 9.5°, 8500 km s^{-1} ; Wakamatsu et al., 2005).

In the southern Galactic hemisphere is the Pavo supercluster at ≈ (332°, -24°, 4500 km s^{-1} ; Juraszek et al., 2000), connecting to the Pavo-Indus filamentary structure. In the same area of sky as Norma, less prominent but still significant, is the Ara cluster located at ≈ (329°, -9°, 15 000 km s^{-1} ; Woudt et al., 1999).

The above-mentioned structures are labelled in Fig. 1.2. Voids, on the other hand, are not marked in the figure, however, they are equally important as dense regions in the context of flow fields. The Local Void encompasses a longitude range of ~ 330° – 45° (Kraan-Korteweg et al., 2008a), starting at a distance of ~1 Mpc (Tully et al., 2019) and extending into the ZoA. Further discussion on voids can be found in Sect. 4.11.

1.7 Thesis Outline

The introduction highlighted the importance of hidden galaxy structures that remain uncharted behind the deepest layers of obscuration of the Milky Way, while emphasising at the same time the power of HI surveys in penetrating this so-called Zone of Avoidance. Existing ZoA HI surveys have so far revealed new insights, but remain quite shallow. The new generation of SKA Pathfinders, however, open up new opportunities that will probe an order of magnitude deeper (higher sensitivity) at higher angular resolution (early HI studies are mostly single-dish data), and will go out to considerably larger distances. In this dissertation I investigated these possibilities using MeerKAT data to probe two different areas in the ZoA to search for hidden galaxies through their HI emission.

The remainder of this thesis is arranged as follows. Automated source finding in spectral line data cubes is introduced in Chapter 2. This is accompanied by descriptions of relevant HI parameters, related methodology, and data visualisation. Chapters 3 and 4 focus on two distinct HI surveys. Chapter 3 presents the MeerKAT16 HI Early Science project directed at the Vela Supercluster region, with an emphasis on testing and optimising the SoFiA pipeline. Chapter 4 utilises the HI line component of the MeerKAT Galactic Plane Legacy Survey (GPS) to map galaxies in the vicinity of the Great Attractor. Large scale structures identified in the data are compared to literature and discussed in detail. Chapter 5 is a final discussion, closing with future perspectives. The full galaxy catalogues for Chapters 3 and 4 are given in Appendices A and B.

Chapter 2

Automated Source Finding and Parametrisation

This section presents an overview of the automated source finding pipeline, SoFiA (Serra et al., 2015; Westmeier et al., 2021), with an emphasis on the outputs and reliability criteria that are relevant for the surveys analysed in this dissertation (presented in Chapters 3 and 4). Following this is a description of how galaxy candidates can be visualised (e.g., through HI profiles and moment maps).

2.1 SoFiA

This work utilises the publicly available software application SoFiA (Source Finding Application[1]) as the tool for automated galaxy identification and parametrisation. When applied on an HI data cube with numerous optional parameter settings, SoFiA will return a catalog of HI galaxy detections along with an extensive range of output products for scientific analyses.

Reliability and completeness are two basic indicators of how well the source finder is performing. The reliability[2] of a source finder (or a particular catalog) is the percentage of sources in the catalog that are genuine sources. The completeness is defined as the percentage of all real sources within the data cube that was successfully detected (Westmeier et al., 2021). A (hypothetical) perfect source finder will achieve 100% reliability and 100% completeness. In reality, reliability and completeness approach 100% with increasing

[1]Source code of SoFiA is available on GitHub: https://https://github.com/SoFiA-Admin/SoFiA-2

[2]Not to be confused with SoFiA's reliability filter, described in Sect. 2.1.3.

signal-to-noise ratios (SNR) of sources. Using WALLABY data, Westmeier et al. (2021) demonstrated that SoFiA achieves almost 100% completeness for a SNR of 5–6 if the data are free of major artifacts. This encouraging result suggests we should be able to achieve the anticipated detection rates from the MeerKAT spectral line data utilised in this work.

2.1.1 Inputs

A data cube is made up of three dimensions, with the x and y axis representing spatial coordinates (either in Right-Ascension/Declination or Galactic longitude/latitude) and the z-axis representing redshift distance — as either frequency or recessional velocity for a given spectral line. The SoFiA pipeline begins by reading in a chosen data cube in Flexible Image Transport System (FITS) format (Pence et al., 2010). This is the first step in the process, as can be seen from the diagram in Fig. 2.1, which outlines the main steps in the SoFiA software (Serra et al., 2015). Another required input is a parameter file (in .txt format) tailored to the data and the type of sources that are anticipated to be found. If a parameter is not specified, SoFiA will use the default parameter setting. The default settings have been "proven to be useful in most situations" according to the SoFiA group.

Optional inputs include an associated noise cube (a FITS cube containing the noise levels throughout the data cube) or a weights cube (a FITS file that assigns weightings to all coordinates). Adding a noise cube to SoFiA means the data cube will be divided by the noise in order to normalise the noise level across the cube. Analogously, if a weights cube is applied, the data cube will be multiplied by the square root of the weights cube (Westmeier, 2021). This step removes the noise variations attributed to the primary beam attenuation corrections (Ramatsoku et al., 2016). The source-finding algorithm (described in Sect. 2.1.2 below) assume that the noise level is uniform across the data cube (Serra et al., 2015). Therefore, minimising noise variation with either a noise or weights cube makes the use of a constant source finding threshold more appropriate.

2.1.2 Source Finder

SoFiA 's Smooth and Clip algorithm (S+C finder) is used for source finding (see 'S+C finder' component in Fig. 2.1). It starts by identifying all voxels (the three dimensional version of a pixel) in the data cube with an absolute flux value above a user-defined threshold, SCFIND.THRESHOLD. A typical threshold is 4σ (in this context σ represents the mean noise level). After the voxels above the threshold are identified, SoFiA smooths the data cube and repeats the process. The number of S+C smoothing iterations and sizes of the smoothing kernels are user defined.

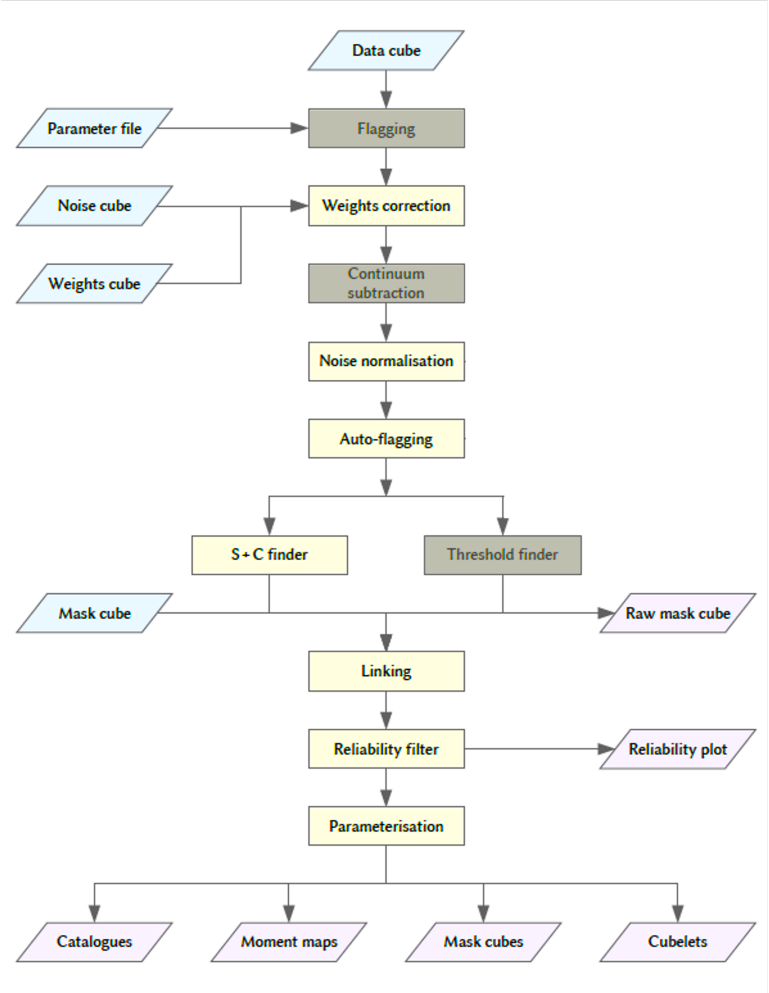

Figure 2.1: Flow chart of the SoFiA pipeline — a simplified version of Fig. 1 in Westmeier (2021). Yellow blocks are the individual algorithms, blue blocks are the possible inputs and purple blocks are the outputs that can be generated. Greyed-out steps are not being used in this work.

Neighbouring voxels detected by the S+C finder who's absolute flux exceeds the flux threshold are grouped together. This is completed during the algorithm's Linking phase (cf. Fig. 2.1), using a basic friends-of-friends algorithm. All objects are then tested against user-specified minimum and maximum linking lengths: LINKER.MINSIZEXY and LINKER.MAXSIZEXY (for the spatial dimension), and LINKER.MINSIZEZ and LINKER.MAXSIZEZ (for the spectral dimension). If an object falls below (or above) the given minimum (or maximum) size criteria, it is rejected. SoFiA keeps the remaining objects — including objects with negative flux and objects with positive flux. These objects

are used for the reliability calculation, explained in the following section.

2.1.3 Reliability Analysis

Each positive detection generated in the Linking step is assigned a reliability[3] score (R) between 0 and 1. R is determined using the negative-source method described in Serra et al. (2012). This method operates under two assumptions: 1) that true sources always have positive total flux, and 2) that the noise in the data cube is symmetric. The user defines a multi-dimensional parameter space within which to determine R. This work utilises the mean, summed and peak flux densities, which are divided by the global rms noise level and then logarithmised, denoted as s_{mean}, s_{sum} and s_{max}.

To compute this reliability space, consider the list of positive objects and negative objects separately. Within the parameter space (s_{mean}, s_{sum} and s_{max}) the objects have a discrete and irregular distribution (for visual aid refer to Figs. 3.5 & 3.7 in Chapter 3). During SoFiA 's reliability calculation, the distribution of positive detections is convolved with a Gaussian kernel, transforming the discrete data set into a positive density field, where each 'bin' represents a value P. This process is repeated for the negative detections, resulting in a negative density field, where bins represent N values. Now the 3D parameter space can be probed at any location to obtain a P and N value. Finally, the reliability at that position can be determined by the reliability metric (Serra et al., 2012):

$$R = \begin{cases} \frac{P-N}{P}, & \text{if } P > N, \\ 0, & \text{otherwise.} \end{cases} \tag{2.1}$$

Detections that receive an R value above the user-defined reliability threshold will be catalogued by SoFiA , and the rest rejected.

A final 3D distribution representing the reliability density field can be created using equation 2.1. Examples of the parameter space with the discrete points and the density fields that result from the Gaussian kernel density estimation are illustrated in Figs. 3.5 – 3.10 (as a two-dimensional projection).

2.1.4 Output Products

Masks

SoFiA produces two types of masks. The raw mask, produced by the source finder, is a

[3]Note that 'reliability' in this context is unrelated to the overall reliability of the source finder defined in Sect. 2.1.

binary mask composed of all detected voxels, i.e., voxels with flux density greater than the threshold. The object mask is a mask of the detections in the final source catalog. Voxels that form part of an object have a value corresponding to the ID number of their detection, and all non-detected voxels have a value of 0. These masks can be used as input for subsequent SoFiA runs, allowing for re-parametrisation of sources without the initial source finding step, which greatly reduces the overall run-time.

Catalogs

The main output product is the final source catalog: a compilation of detections each assigned with a unique ID, their positions in the data cube and a choice of over 50 other parameters (e.g., total flux and local rms noise). The parameters most significant to this work are described in Sect. 2.2.

During the Linking step, SoFiA collects all positive objects and all negative objects in the data cube. SoFiA can output these additional catalogs to the user for diagnostic purposes. It is important to keep in mind that the final source catalog is a subset of the catalog of all positive objects. The catalogs of all objects contain the parameters used for the reliability calculation (explained in Sect. 2.1.3). These extended lists can be used to scrutinise SoFiA 's performance (as in Chapter 3).

Cubelets

If prompted, SoFiA can produce small FITS files of each individual detection in the following forms: 3D cut-outs from the original cube, 3D binary masks or 2D images of moment maps (defined in Sect. 2.3).

2.1.5 Versions

The descriptions above give a general summary of the SoFiA software. Note, however, that two versions exist. The original software (henceforth referred to as SoFiA 1[4]) is written in several programming languages, including a large portion in Python. This leads to problems often associated with the Python programming language including, but not limited to, long execution times, large memory consumption and difficulty with long-term maintenance. For these reasons, the SoFiA team developed a faster version written in the C programming language (Westmeier et al., 2021), henceforth referred to as SoFiA 2. The pipelines are essentially the same, with minor differences in parameters, but the later

[4]As of November 2022, SoFiA 1 is no longer maintained.

version is considerably faster and requires about half the memory. Both SoFiA 1 and SoFiA 2 were used in this research.

2.2 HI Parameters Derived from SoFiA

As mentioned in Sect. 2.1, SoFiA returns a wide variety of output products, predominantly HI parameters of each detection, which are calculated during the parametrisation step (see last yellow block in Fig. 2.1). HI parameters refer to a range of basic measurements of an HI source measured by SoFiA during the parametrisation step (indicated in Fig. 2.1). Some of the most fundamental parameters are the line width, the peak flux density, and the integrated flux density. In turn, these values allow the derivation of another key parameter — the HI mass (see Sect. 2.2.1).

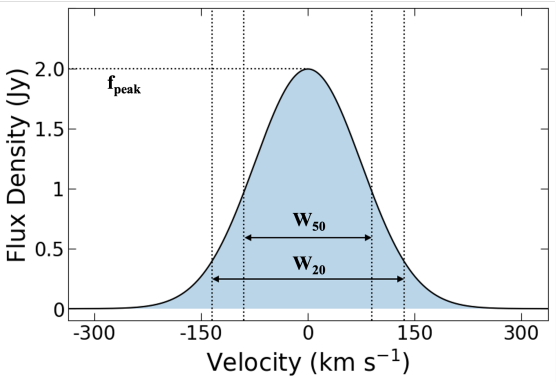

Figure 2.2: A spectral HI profile of a hypothetical SoFiA detection, indicating the line width measurements (W_{20} and W_{50}) and peak flux ($f_{\rm peak}$). The integrated flux ($f_{\rm int}$) is represented by the shaded region.

Figure 2.2 shows an idealised HI spectral line profile of a galaxy. The line width of a galaxy detection is measured at two places on the profile: where the flux density is at 20% of the peak (W_{20} in Fig. 2.2) or at 50% of the peak (W_{50} in Fig. 2.2; also known as the Full Width Half Maximum). The peak flux density ($f_{\rm peak}$ in Fig. 2.2) is the maximum flux density of the source in units of Jy, and the integrated flux ($f_{\rm int}$) is the sum of the flux values of all the voxels that make up the source, in units of Jy km s^{-1} (or Jy beam^{-1} km s^{-1}). In Fig 2.2, $f_{\rm int}$ is represented by the blue shaded region.

When PARAMETER.PHYSICAL is set to True in the parameter file, SoFiA will convert parameters to physical units using keywords from the FITS header. This process includes converting channel widths to frequency (or velocity) units and dividing spatially integrated parameters by the solid angle of the beam ($\Omega_{\rm beam}$). In this way, integrated flux units are

converted from $\mathrm{Jy\,beam^{-1}\,km\,s^{-1}}$ to $\mathrm{Jy\,km\,s^{-1}}$. Fluxes corrected for the beam area will be denoted by $S_{\rm int}$:

$$S_{\rm int} = \frac{f_{\rm int}}{\Omega_{\rm beam}} \ , \tag{2.2}$$

where

$$\begin{aligned} \Omega_{\rm beam} &= \frac{\pi\theta_a\theta_b}{4\ln 2} \\ &= \frac{\pi}{4\ln 2}\left(\frac{\rm B_{maj}}{\rm pix}\right)\left(\frac{\rm B_{min}}{\rm pix}\right) \end{aligned} \tag{2.3}$$

and $\rm B_{maj}$ and $\rm B_{min}$ are the major and minor axes of the beam, respectively, and pix is the spatial pixel size. $\rm B_{maj}$, $\rm B_{min}$ and pix must have the same units.

2.2.1 HI mass limit

The integrated flux density ($S_{\rm int}$) can be used to calculate the detected HI mass ($M_{\rm HI}$):

$$M_{\rm HI} = \frac{2.356\times10^5}{1+z} D^2 S_{\rm int} \tag{2.4}$$

in units of $M_{\rm HI}/M_\odot$, where z is the redshift, D is the approximate luminosity distance in Mpc, calculated directly from the heliocentric velocity $V_{\rm hel}$ (given in the optical convention throughout this dissertation):

$$D = \frac{V_{\rm hel}}{H_0} \ . \tag{2.5}$$

The Hubble constant (H_0) is taken as 70 $\mathrm{km\,s^{-1}Mpc^{-1}}$ throughout this dissertation. It is also possible to estimate the theoretical flux density limit ($S'_{\rm int}$) of a detection with a user-defined SNR ($\sigma_{\rm thresh}$) by multiplying the mean rms of the survey with the theoretical line width (W):

$$S'_{\rm int} = \sigma_{\rm thresh}\,{\rm rms}\left(W\times\sqrt{\Delta z/W}\right) \ , \tag{2.6}$$

where W is scaled by the number of spectral channels (the square-root term). Note eq. 2.6 assumes a point source.

We can plot the theoretical HI mass limit ($M'_{\rm HI}$) as a function of $V_{\rm hel}$ for the full velocity range — this is called the flux density sensitivity curve. To do this, we replace $S_{\rm int}$ in equation 2.4 with $S'_{\rm int}$. Then the sensitivity curve for a detection in a given survey is:

$$\begin{aligned} M'_{\rm HI} &= (2.356\times10^5)D^2S'_{\rm int} \\ &= (2.356\times10^5)\left(\frac{V_{\rm hel}}{H_0}\right)^2\left(\sigma_{\rm thresh}\,{\rm rms}\,W\sqrt{\Delta z/W}\right). \end{aligned} \tag{2.7}$$

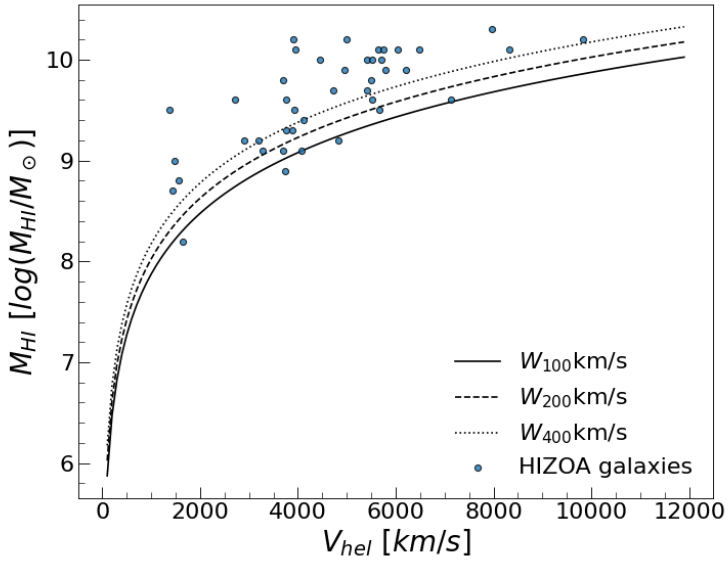

Figure 2.3: HI mass ($M_{\rm HI}$) as a function of heliocentric velocity ($V_{\rm hel}$) for the 42 HIZOA detections (blue dots) that fall within the on-sky search area relevant for Chapter 4 ($302^\circ \le \ell \le 332^\circ$ and $-1.5^\circ \le b \le 1.5^\circ$). The theoretical sensitivity $M'_{\rm HI}$ ($M_{\rm HI}$ limit) is plotted for line widths of 100, 200 and 400 km s^{-1} at a 5σ threshold (black lines).

In Fig. 2.3, sensitivity curves for the HIZOA survey (Staveley-Smith et al., 2016) are generated for 5σ detections (i.e., detections with a SNR of 5) with line widths of 100, 200 and 400 km s^{-1}, respectively, for a survey with an rms of 6 mJy. The curves represent the lower limit of the HI mass of a 5σ galaxy for an assumed linewidth of W detectable by the survey. The dependence on W means a different completeness is expected for every line width. The blue points represent the measured HI masses of the subset of HIZOA galaxies that coincide with the on-sky search area defined later, in Chapter 4. The blue dots that fall below the lowest curve represent galaxy detections with $W<100$ km s^{-1} and/or a SNR of $<5\sigma$.

2.3 Moment-maps

There are several ways of representing 3-dimensional data in 2-dimensional space. A 2D projection of a single spectral channel, where the x and y-axes are the spatial axes, is referred to as a channel map. Conversely, when a slice of data are extracted along the spectral (velocity) axis, it is called a position-velocity (pv) map.

Moment-maps are useful analysis tools for studying spatially resolved spectral line emission. The moment-0 map describes the amount of HI flux (S) at each pixel (equivalent to the column density) when integrated over the spectral axis of a cube:

$$M_0 = \int S \mathrm{d}v, \tag{2.8}$$

where $\mathrm{d}v$ represents increments in the spectral domain (velocity or frequency increments). A moment-0 map is sometimes called an intensity map since it represents the total, integrated flux density detected in an observation.

The moment-1 map describes the kinematics within a data cube (or more commonly within a small sub-cube around a detection). Mathematically, it is the intensity-weighted velocity along the line of sight:

$$M_1 = \frac{\int v S \mathrm{d}v}{\int S \mathrm{d}v} \tag{2.9}$$

Creating a moment-0 map around a detection describes the galaxy's structure and intensity, whereas a moment-1 map can be used to analyse the local motions of the HI gas along the line of sight. From this reference frame, gas moving away from the observer will be redshifted and gas moving towards the observer will be blueshifted. When a galaxy is redshifted on one side and blueshifted on the other side, it is an indication of a rotating disk.

The kinematics we observe in a moment-1 map is dependent on the inclination of the galaxy along the line-of-sight to the observer. A galaxy has an inclination of 0° if the plane of the galaxy is face-on, and an inclination of 90° if the plane of the galaxy is edge-on. The gas in a galaxy exhibits a combination of ordered motion (rotation) and random motion (dispersion), and the ratio of these that we measure is dependent on the viewing angle. Dispersion is the dominant factor in face-on galaxies, and as the inclination is increased, the rotational motion begins to dominate, reaching a maximum in edge-on

galaxies, where the tangential motion due to rotation is most accentuated with respect to the observer. If we observe a galaxy face-on, its HI profile will resemble a Gaussian. If the galaxy is slightly angled it could result in a 'flat-topped' profile, whereas an edge-on galaxy will give rise to a double-horn profile (Kovač et al., 2009). See illustrations in Fig. 2.4.

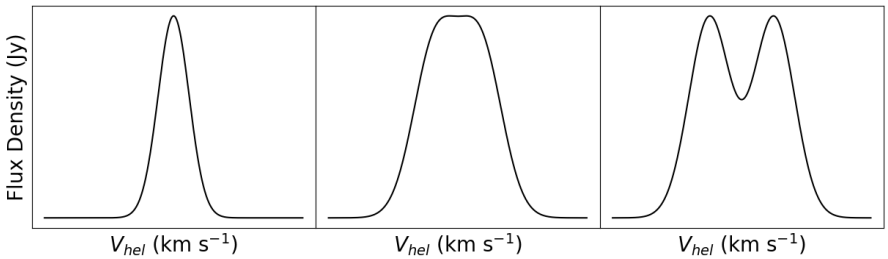

Figure 2.4: Idealised spectral HI profile shapes: Gaussian (left), flat-topped (middle) and double-horned (right).

In summary, SoFiA is used for source finding and parametrisation of sources (SoFiA 1 in Chapter 3 and SoFiA 2 in Chapter 4) and 2D projections of data (channel maps, pv maps and moment maps) are used to verify these sources visually. Several HI parameters were presented in this section, which are all used extensively for analysis in Chapters 3 and 4.

Chapter 3

MeerKAT16 Pilot Project

The MeerKAT16 HI observations presented here served as a testing and commissioning project for a planned larger HI survey to map the extent of the Vela Supercluster (VSCL; Kraan-Korteweg et al., 2017) across the fully opaque part of the Zone of Avoidance (ZoA). Pilot projects such as MeerKAT16 allow scientists to test technology and pipelines (such as SoFiA) that will be used by the SKA pathfinders.

The VSCL is believed to consist of a broad primary wall at $V_{\rm hel} \approx 18\,000\,{\rm km\,s^{-1}}$, which extends above and below the Galactic plane, and a secondary smaller wall at higher redshifts, showing up below the Galactic plane (Kraan-Korteweg et al., 2017). This Early Science data aimed to map the galaxy cluster VC04, embedded in the main VSCL wall.

3.1 Data Collection and Reduction

The galaxy cluster VC04 ($\ell \sim 272.25°$, $b \sim$-9.0°, $cz \sim 18\,000\,{\rm km\,s^{-1}}$; Kraan-Korteweg et al., 2017), and its immediate environment along the wall in which it is embedded, was observed in HI through six pointings. The coordinates of the pointings are listed in Table 3.1. At the time of the observations, 16-dish subarrays were available for operation, with a maximum baseline of 1 km. Data were collected in May 2018 over two nights using two different MeerKAT16 subarrays. Both runs cycled through three pointings, resulting in six fields, each with ~three hours on-source integration (excluding overhead).

According to simulations based on the HI mass function (HIMF) from Zwaan et al. (2005), four hours observation time (including overhead) per pointing would be enough

time to detect all galaxies with HI masses ($M_{\rm HI}$) half an order of magnitude below the characteristic $M_{\rm HI}$ $\log M^*_{\rm HI} = 9.86\,M_\odot\,h_{70}$ (Zwaan et al., 2005) at the VSCL distance, and allow us to obtain adequate statistics to map the overdensity at and around the VC04 cluster (Kraan-Korteweg et al., 2016).

Run	Max baseline (km)	RA (J2000)	Dec (J2000)	l (deg)	b (deg)	Measured rms (mJy beam^{-1})
1	1	08:35:42	-55:52:56	272.25	-9.10	1.13
1	1	08:31:52	-55:17:53	271.45	-9.20	1.20
1	1	08:39:38	-55:17:19	272.10	-8.30	1.22
2	0.5	08:35:14	-54:46:12	271.30	-8.50	1.21
2	0.5	08:44:09	-54:44:05	272.05	-7.45	1.20
2	0.5	08:39:40	-54:17:41	271.30	-7.70	1.24

Table 3.1: The on-sky coordinates and mean rms of the six pointings (courtesy P. Serra) observed for the MeerKAT16 Early Science Program. The first three pointings were combined into Mosaic 1 and the last three pointings were combined into Mosaic 2.

The initial data reduction was completed in July 2018 with the CARACal pipeline (previously called the MeerKATHI pipeline; Józsa et al., 2020). The data were obtained with the MeerKAT L-band and the ROACH2[1] 32k correlator. The 32k configuration provides 32 768 channels over 856 MHz, yielding a channel resolution of ∼26 kHz, which corresponds to a Doppler-shifted velocity width of $\sim 5\,{\rm km\,s^{-1}}$ for HI at $z = 0$. A 110 MHz bandwidth, encompassing a frequency range ∼1308 – 1418 MHz (averaging over every two channels), was processed by our collaborator P. Serra. This frequency range was chosen deliberately to exclude well-known recurring and strong RFI below the low frequency cut-off as well as Milky Way HI emission beyond the high-frequency cut-off. The corresponding heliocentric recessional velocity range is $V_{\rm hel}$ = ∼600 to ∼23 000 $\rm km\,s^{-1}$ ($z \lesssim 0.077$).

3.2 Imaging and Mosaicking

The HI imaging was done with WSClean using natural weighting and no constraints to the beam (PSF) shape. The individual images have a field of view of $2^\circ \times 2^\circ$ on-sky. Run 1 had a maximum baseline of 500 m, while run 2 had a maximum baseline of 1 km, and as a result the three images from run 1 have a larger beam size and a lower angular resolution than the run 2 images. The three run 1 images and the three run 2 images were mosaicked

[1]Reconfigurable Open Architecture Computing Hardware

into Mosaic 1 and Mosaic 2 respectively, using the Maximum Entropy Method described in Cornwell (1988). The mosaics are pictured in Fig. 3.1.

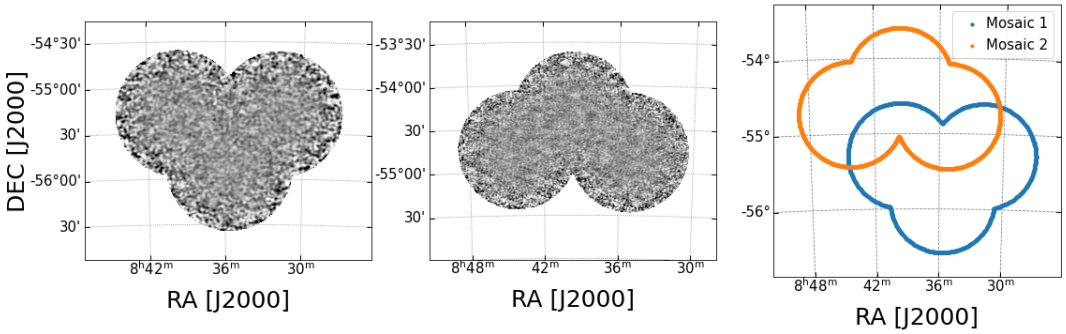

Figure 3.1: On-sky projections of the HI data cubes Mosaic 1 (left) and Mosaic 2 (middle). The grey colour scale indicates the noise variations (mean rms 1.2 mJy beam^{-1}). Note Mosaic 1 has a larger pixel size than Mosaic 2, and therefore has a grainier appearance. Right: The on-sky projections of the outer-edges of Mosaic 1 (blue) and Mosaic 2 (orange), showing the notable overlap between the mosaics.

Mosaicking cubes together offers many advantages, including combining fluxes in overlapping regions, which reduces the noise, resulting in increased sensitivity. It also aids in removing the "edge-effects" in primary-beam corrected images. Furthermore, any regions of overlap between mosaics are useful for verification purposes and quantification of results because sources residing here are derived from two distinct observations.

The mosaicking for MeerKAT16 was done with natural weighting and without CLEANing (Högbom, 1974). The UV-coverage and low PSF sidelobes means that deconvolution is unnecessary for this data. As displayed in Fig. 3.1, both final mosaics comprise three circular fields with on-sky diameters of $\sim 1.4°$. After applying the primary beam correction, the rms increases with radius from the centre, therefore the data are truncated at 1.4°, where the sensitivity becomes too low for analysis and any sources that reside there will be overwhelmed by noise.

The longer baselines for Mosaic 2 resulted in a higher spatial resolution, which allowed for finer gridding (smaller pixels) compared to Mosaic 1. This is evident in the channel maps in Fig. 3.1. Despite this difference, the integrated flux of a source will ultimately measure the same on both mosaics, and both the mosaics have a mean rms of 1.2 mJy beam^{-1}, as measured in a central plane. The specifications are summarised in Table 3.2.

Mosaic	Max baseline (km)	Beam size (")	Spatial res. (")	Spectral res. ($km\,s^{-1}$)	Measured rms ($mJy\,beam^{-1}$)
1	~0.5	132×102	24	11	1.2
2	~1.0	68×55	16	11	1.2

Table 3.2: Specifications of the two MeerKAT16 mosaics. The given beam size is the median beam size of the three individual pointings of the respective mosaic. The rms values are measured in a central plane across the full frequency range (1308 – 1418 MHz) and are given per 11 $km\,s^{-1}$ channel.

3.3 Source Finding

3.3.1 Visual Searching

Another advantage of mosaicking adjacent fields is that it results in a larger field with uniform sensitivity which is convenient for source finding. A deep visual search was carried out on both mosaics at the end of 2019 by two members of the UCT Astronomy Department: Prof. R. Kraan-Korteweg and V. Pillay (Pillay, 2020). The search was executed as deep as possible, as the goal was to use the list for an in-depth comparison with the automated source finder. The visual lists were merged and adjudicated by an independent third person (M. Ramatsoku).

The visual search was conducted with the visualisation tool KVIS from the Karma software suite (Gooch, 1996). The data cubes were viewed from the z-y axis (velocity-Dec) and the users browsed through the x channels (RA), because from this perspective real galaxies appear horizontally elongated. Figure 3.2, saved directly from KVIS, demonstrates how a real source was located. The top image shows a single slice of the data cube zoomed into a detection (appearing in white), and the bottom image shows the accompanying line profile along the z (velocity) axis.

Visual searchers scan the data for bright groups of pixels (such as the centre of the image in Fig. 3.2) and then consider factors that point towards it being a real source, as opposed to a false positive; for example, real galaxy detections tend to be more extended in the velocity (frequency) axis, due to the motion of the gas around the centre of the galaxy. Therefore, the object should be visible over at least a few consecutive spectral channels and, additionally, the velocity profile should be consistent with a known HI shape, namely double-horned, flat-topped, or Gaussian (cf. Fig. 2.2). A double-horn profile indicates an edge-on galaxy (ordered rotation) whereas the high degree of random motion in face-on galaxy results in a more Gaussian-like shape (cf. Sect. 2.3).

Bright objects encountered on the outer-edge of a mosaic are more likely to be false

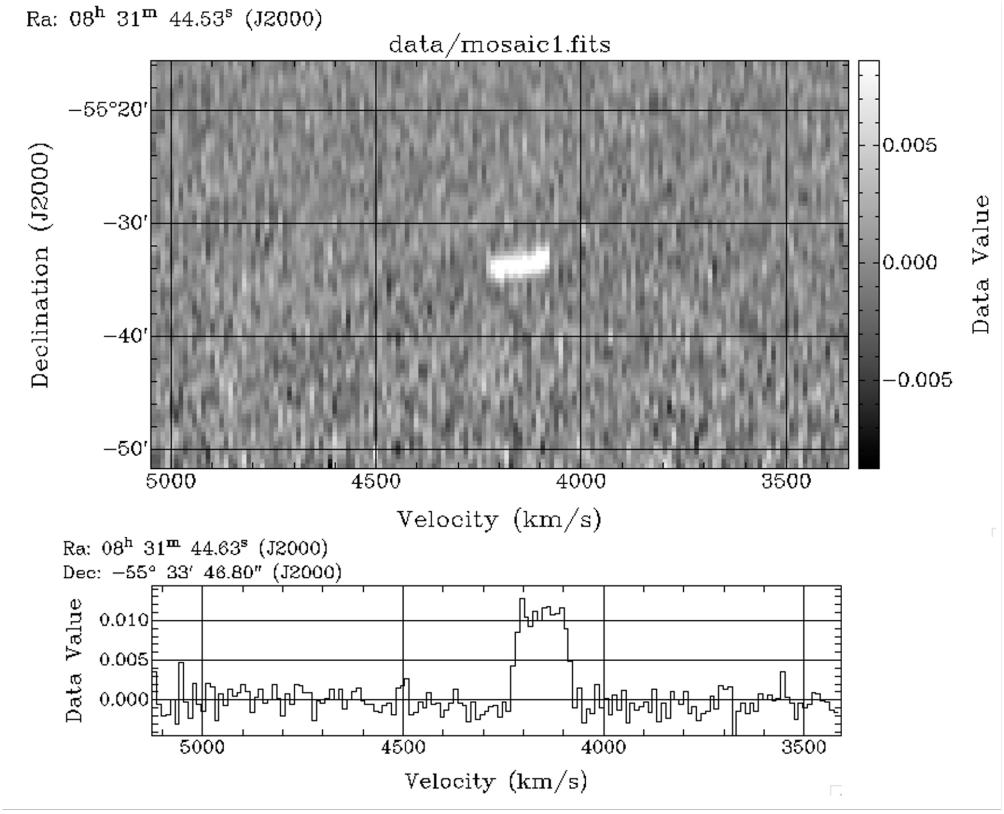

Figure 3.2: The user interface of KVIS. Top: A slice of the data cube through the ZY axis, showing a real galaxy detection in the centre (white group of pixels). Bottom: the HI line profile (along the z-axis) through the centre of the source.

because these areas have a higher noise level. Furthermore, positive spikes that have many similar neighbouring spikes (positive or negative) are considered more dubious. Visual detections are catalogued when the signal can clearly be spotted above the noise; with an HI profile distinct from the baseline (as in the bottom panel of Fig. 3.2).

After the adjudication and additional checks and corrections, close to 200 galaxy candidates were recorded in the visual list. Following the visual search, automated galaxy searching and parametrisation was implemented with SoFiA (introduced in Chapter 2). In Sect. 3.3.4, with the aid of the HI parameters provided by SoFiA , the detections are classified according to their credibility, and the weakest visual detections are rejected.

3.3.2 Cross-matching with the SoFiA Catalogs

An independent search for HI sources in the two data cubes was completed with SoFiA . Several combinations of control parameters and software versions were tested by myself and collaborators P. Serra and J.M. van der Hulst (who have extensive experience using SoFiA), and all output catalogs were compared to the visual detection list. To determine which of the settings are optimal for our data, we need to cross-match the various SoFiA results with the visual galaxy catalog and identify common galaxies. For this I devised a cross-matching strategy using the Python package `Cross_Matching`[2].

To cross-match catalog A (e.g., the SoFiA sources) with catalog B (e.g., the visual sources), the user inputs the two positional catalogs and defines an appropriate on-sky limit (xy limit) and a line-of-sight limit (z limit). For each entry in catalog A, a search through catalog B is performed to collect all the entries that fall within the limits. If there is more than one possible match, the closest on-sky match is selected.

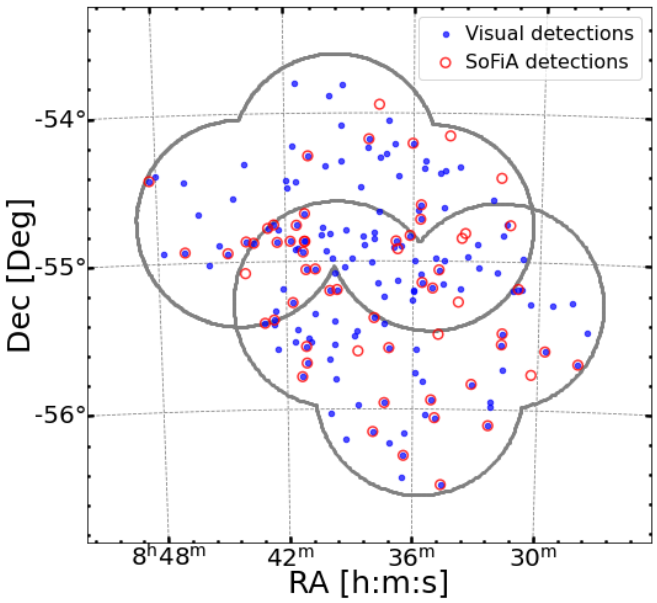

Figure 3.3: The on-sky projections of the outer-edges of the two mosaics (grey outlines). Blue markers represent visual detections and red circles indicate all SoFiA galaxy detections (which will be assessed for credibility).

The on-sky separation and the velocity (line-of-sight) separation was chosen as 120" and 400 km s^{-1} respectively. If two detections are separated by less than this, they are

[2]Code available at https://github.com/TrystanScottLambert/Cross_Matching

potential counterparts. The centre coordinates of a source as calculated by an algorithm can differ significantly from the centre which was picked by eye, therefore these thresholds are large enough to ensure we do not miss a potential match.

After cross-matching the visual list with the output of several different SoFiA runs, the run that recovered the most visual galaxies was the software version 1.3.2, using the parameter settings listed in Appendix A — which included a flux threshold (SCFIND.THRESHOLD) of 3.5σ for Mosaic 1 and 4.0σ for Mosaic 2. In Mosaic 1, SoFiA catalogued 40 detections in total, of which 31 have visual counterparts. In Mosaic 2, SoFiA catalogued 26 detections in total, of which 19 have visual counterparts. The visual galaxy candidates and the SoFiA detections are shown in Fig. 3.3.

3.3.3 Positive Signals Catalog

It was found that many of the visual sources have no counterpart in the SoFiA galaxy source list (blue dots in Fig. 3.3). These could be low signal-to-noise (SNR) sources or false sources. To understand and quantify why some sources were not identified as likely galaxy candidates in the SoFiA run, we require the HI parameters of the visual sources. As mentioned in Chapter 2.1.2, a high number of positive signals (including the detections on the output catalog) are saved in a catalog (SoFiA 's Positive Logarithm Catalog) which we dubbed the Positive Signals Catalog. It was expected that many real sources would have been captured in this catalog, but failed the reliability criteria (which includes a user-defined threshold of $R \geq 0.7$). In an effort to retrieve these sources, a cross-match was performed between the visual sources with no SoFiA counterparts and SoFiA 's Positive Signals Catalogs. After this approach, an additional 70 parametrised galaxy candidates were 'rescued' from the data cubes.

The remaining ~ 50 visual detections still left unaccounted for were re-checked in KVIS and confirmed as weak candidates — mostly only visible in very few voxels. These were henceforth marked as rejects. The fact that they are absent from the Positive Signals Catalogs means they fell below the flux threshold and were not linked together into an object during SoFiA 's Linking step (cf. Fig. 2.1), which attests to the fact that they are weak or erroneous candidates. Without the parameters returned by SoFiA , it would be complicated to include these weak objects in the analysis (elaborate hand-parametrisation would be required) and, even then, there is no guarantee that the measurements would be comparable to SoFiA 's other parametrisation results. Furthermore, rejecting these low-confidence objects does not impact the goals of this project.

One final cross-match was required to eliminate duplicate galaxy detections from

the overlap area between the two mosaics (see Fig. 3.1). Eight galaxy candidates were identified twice in this region. To free the list of duplicate entries, only one of each doubly-detected source is selected, opting for the choice that lies further away from the edge of its respective mosaic. The source lists from the two mosaics (all of which now have SoFiA parameters) were combined into one duplicate-free catalog of 156 galaxy candidates. A further verification process has been pursued to classify these detections according to their credibility.

3.3.4 Classification of Sources

Extensive manual verification was carried out to assess the validity of each of the 156 galaxy candidates. Using Python packages such as `SpectralCube`, we produced moment-0 maps and global HI line profiles of all galaxy candidates in order to inspect them individually. A key indicator of a reliable detection is the integrated flux density signal-to-noise ratio (SNR). It is calculated as:

$$\mathrm{SNR} = \frac{S_{\mathrm{int}}}{\mathrm{rms} \times W_{20} \times \sqrt{\Delta z \,/\, W_{20}}} \ , \tag{3.1}$$

where S_{int} is the integrated flux in $\mathrm{Jy\,km\,s^{-1}}$, rms is the measured rms in the data (in $\mathrm{Jy\,beam^{-1}}$), W_{20} is the line width at 20% (in $\mathrm{km\,s^{-1}}$) and Δz is the spectral channel width of 11 $\mathrm{km\,s^{-1}}$.

As a final verification process of the galaxy candidates, we assessed the moment-0 maps, HI profiles, SNR, line widths of each galaxy candidate and classified them into three categories: category 1 detections show strong evidence of being real (well-defined moment-0 maps and HI profiles); category 2 detections are likely real, but with reduced confidence because of factors such as high local noise; and category 3 are weak candidates, most of which have a SNR less than about 2.5 (i.e., $\lesssim 2.5\sigma$).

Figure 3.4 shows W_{20} versus SNR (calculated using equation 3.1). This plot demonstrates that the category 3 detections (red dots) are small detections with low SNR.

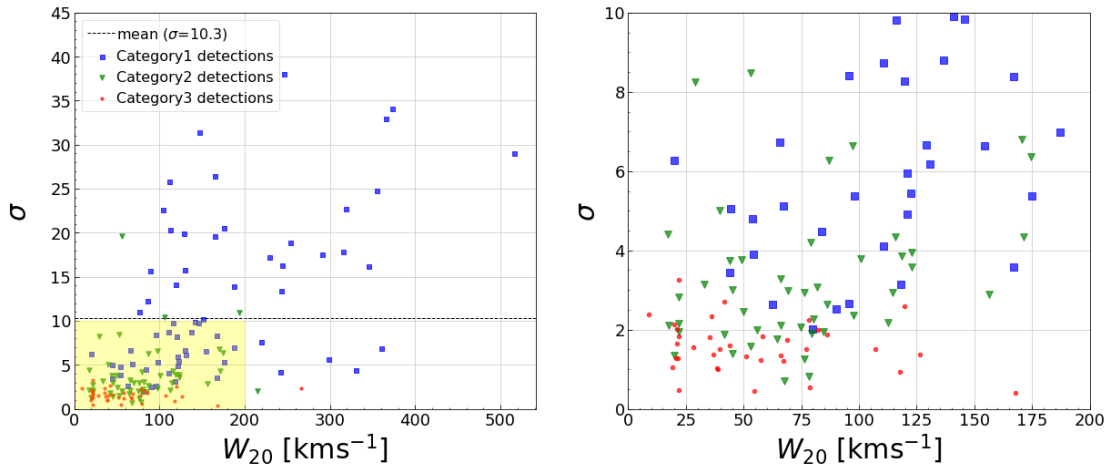

Figure 3.4: Left: Line width at 20% (W_{20}) versus SNR of all 156 MeerKAT16 detections. Three sources with SNR >45 are not shown. Right: zoom-in of SNR <10 & $W_{20}<200$ km s^{-1} detections (yellow shaded region on left image). SNR was calculated with equation 3.1 using the mean mosaic rms of 1.2 mJy beam^{-1}. Category 3 detections (red markers) were determined to have a low likelihood of being real and are omitted from further analysis.

	SoFiA Catalog			**Other SoFiA detections**			**Total**
	Mosaic1	Mosaic2	All	Mosaic1	Mosaic2	All	
All	40	26	66	63	47	110	176
Duplicates ignored	1	4	5	1	2	3	8
Rejected for analysis	9	3	12	22	15	37	49
Accepted for analysis	30	19	49	40	30	70	**119**

Table 3.3: Final tally of the detections in the MeerKAT16 survey. 'Duplicates' refers to (reliable) detections that were found in both mosaics.

3.4 MeerKAT16 Results

One key part of this analysis is to get a better understanding of the parameter space of sources that SoFiA did not identify as reliable, compared to the sources it did. If quantifiable, this could be used as feedback to improve on future SoFiA versions. We pose the question whether this outcome can be improved. In addition, we investigate the HI galaxy distribution around the VC04 cluster to learn more about the properties of the cluster.

3.4.1 MeerKAT16 Galaxy Catalog

An extract of the MeerKAT16 galaxy catalog is displayed in Table 3.4, and the full catalog is available in Table A1, Appendix A. The columns are as follows:
– (1) MeerKAT16 identifier, reflecting the equatorial coordinates [MK16-Jhhmmss ± ddmmss].
– (2) Mosaic (1 or 2).
– (3) Galactic longitude [deg].
– (4) Galactic latitude [deg].
– (5) Integrated flux [$\mathrm{Jy\,km\,s^{-1}}$].
– (6) Local rms [$\mathrm{Jy\,beam^{-1}}$].
– (7) Heliocentric velocity [$\mathrm{km\,s^{-1}}$].
– (8) Line width at 20% of the peak flux [$\mathrm{km\,s^{-1}}$].
– (9) Line width at 50% of the peak flux [$\mathrm{km\,s^{-1}}$].
– (10) Reliability R (between 0 and 1) [unitless].
– (11) Mean flux density, divided by the global rms noise level and then logarithmised s_{mean} [unitless].
– (12) Summed flux density, divided by the global rms noise level and then logarithmised, s_{sum} [unitless].
– (13) Peak flux density, divided by the global rms noise level and then logarithmised, s_{max} [unitless].
– (14) SNR, as calculated with the local rms [unitless].
– (15) SNR, as calculated with the mosaic rms (1.2 $\mathrm{mJy\,beam^{-1}}$) [unitless].
– (16) HI mass – calculated with eq. 2.4 [$\log(M_{\mathrm{HI}}/M_{\odot})$]. HI masses have not been corrected to the barycentre of the Local Group (V_{LG}).
– (17) Flag [category 1, 2 or 3, from highest confidence to lowest confidence respectively].

An atlas of moment-0 maps is provided: the first page is in Appendix A, and the full atlas is available on Google Drive.

For the remainder of the analysis we leave out the lower-confidence galaxy candidates classified as category 3, to ensure the final results are not unnecessarily contaminated with spurious detections. The total number of category 1 and 2 detections is 119 — see breakdown in Table 3.3. To investigate the HI properties of the final 119 galaxy detections, the distributions of several of their measured HI parameters are plotted: peak flux, integrated flux, line widths, local rms, SNR, and M_{HI}.

Table 3.4: An extract of the MeerKAT16 catalog. The full catalog is in Appendix A.

name	Mosaic	ℓ	b	$S_{\rm int}$	Local rms	$V_{\rm hel}$	W_{20}	W_{50}	R	$s_{\rm mean}$	$s_{\rm sum}$	$s_{\rm max}$	$SNR_{\rm indiv}$	$SNR_{\rm mean}$	$M_{\rm HI}$	flag
J2000	1/2	deg	deg	Jy*km/s	mJy/beam	km/s	km/s	km/s							$\log(M_{\rm HI}/M_\odot)$	1/2/3
(1)	(2)	(3)	(4)	(5)	(6)	(7)	(8)	(9)	(10)	(11)	(12)	(13)	(14)	(15)	(16)	(17)
J082742-552757	1	271.25	-9.78	0.25	3.4	12909	53	30	0.04	0.01	2.21	0.48	3.0	8.5	9.3	2
J082805-554052	1	271.46	-9.86	2.62	3.8	13651	373	323	1.00	0.13	3.18	0.66	10.7	34.1	10.4	1
J082827-551605	1	271.14	-9.58	0.16	2.2	16338	84	49	0.15	0.09	2.24	0.58	2.5	4.5	9.3	1
J082922-551707	1	271.23	-9.48	0.17	1.7	16639	123	100	0.27	0.14	2.41	0.61	2.8	3.9	9.4	2
J082940-553558	1	271.52	-9.63	5.52	2.1	4134	185	152	1.00	0.43	3.81	1.26	57.5	101.8	9.7	1
J083027-551702	1	271.32	-9.36	0.03	1.3	11960	78	32	0.03	0.28	1.79	0.50	0.7	0.8	8.3	2
J083050-545830	1	271.10	-9.13	0.11	1.6	13189	120	12	0.05	0.26	2.22	0.53	1.9	2.6	9.0	3
J083052-551059	1	271.27	-9.25	0.03	1.4	4343	28	14	0.04	0.39	1.80	0.50	1.3	1.5	7.5	3
J083101-551056	1	271.28	-9.23	0.28	1.2	9632	175	96	0.83	0.04	2.75	0.71	5.4	5.4	9.1	1
J083117-551150	1	271.32	-9.21	0.02	1.4	2545	39	26	0.09	0.30	1.70	0.52	0.9	1.0	6.9	3
J083137-544434	1	270.97	-8.91	0.23	2.7	21762	171	13	0.28	0.22	2.30	0.61	1.9	4.4	9.7	2
J083143-554337	1	271.79	-9.47	0.14	1.8	17511	118	102	0.20	0.17	2.30	0.58	2.1	3.1	9.3	1
J083144-552903	1	271.59	-9.32	0.36	1.2	13245	120	56	0.82	0.03	2.86	0.58	8.0	8.3	9.5	1
J083146-553331	1	271.66	-9.36	1.51	1.4	4145	146	131	1.00	0.49	3.43	1.03	26.3	31.4	9.1	1
J083148-544906	2	271.05	-8.93	0.08	2.5	13928	78	59	0.18	0.01	1.70	0.56	1.1	2.2	8.9	3
J083203-550416	1	271.28	-9.05	0.10	1.3	14113	69	23	0.42	0.22	2.26	0.55	2.7	3.0	9.0	2
J083215-555856	1	272.05	-9.55	0.08	2.2	16345	62	55	0.00	0.36	1.98	0.65	1.4	2.6	9.0	1
J083217-543458	2	270.89	-8.74	0.10	2.4	22359	96	81	0.17	0.16	1.87	0.54	1.3	2.7	9.4	1
J083217-555643	1	272.02	-9.53	0.23	2.0	17409	87	26	0.02	0.12	2.47	0.58	3.8	6.3	9.5	2
J083221-560623	1	272.16	-9.61	1.35	2.3	20625	165	135	0.97	-0.01	3.15	0.62	13.6	26.5	10.4	1
J083254-550228	1	271.32	-8.93	0.06	1.4	9305	69	16	0.17	0.05	1.97	0.55	1.4	1.7	8.4	3
J083258-545313	1	271.20	-8.83	0.03	2.5	12520	21	13	0.00	0.32	1.56	0.57	0.8	1.6	8.4	3
J083311-554946	1	272.00	-9.36	1.20	1.4	16933	253	204	1.00	0.10	3.32	0.72	16.4	19.0	10.2	1
J083326-545809	1	271.31	-8.83	0.11	1.8	17132	82	53	0.16	0.19	2.16	0.48	2.1	3.1	9.2	2
J083347-551116	2	271.52	-8.91	0.03	2.3	2547	22	22	0.38	0.01	1.48	0.53	1.0	1.8	7.0	3
J083350-542139	2	270.84	-8.42	0.02	2.2	13485	22	18	0.20	0.39	1.35	0.50	0.7	1.3	8.3	3
J083430-542309	2	270.92	-8.36	0.07	2.0	22077	66	17	0.34	0.16	1.76	0.59	1.3	2.1	9.2	2
J083431-545944	1	271.42	-8.72	0.60	2.4	7375	193	88	0.64	-0.01	2.79	0.58	5.5	10.9	9.2	2
J083435-543811	2	271.13	-8.50	0.07	1.3	17826	50	35	0.07	0.19	1.93	0.60	2.2	2.5	9.0	2
J083435-550905	1	271.56	-8.80	0.03	1.8	22768	37	24	0.00	0.27	1.64	0.48	0.9	1.4	8.9	3
J083437-563033	1	272.68	-9.59	0.59	4.3	4129	89	61	0.99	0.31	2.55	0.73	4.4	15.7	8.7	1
J083446-542418	2	270.96	-8.34	0.04	1.6	18137	21	9	0.37	0.24	1.66	0.57	1.5	2.0	8.8	3
J083447-550331	1	271.50	-8.72	12.87	2.3	4036	286	237	1.00	0.48	4.11	1.40	101.1	191.3	10.0	1
J083455-545851	1	271.45	-8.66	0.05	2.8	6652	42	24	0.04	0.29	1.61	0.45	0.8	1.9	8.0	2
J083456-560327	1	272.33	-9.29	0.83	1.3	8717	243	157	1.00	0.01	3.21	0.64	12.7	13.4	9.5	1
J083504-551055	1	271.62	-8.76	2.37	2.0	4280	246	217	1.00	0.19	3.41	0.83	22.8	38.0	9.3	1
J083507-555614	1	272.25	-9.20	0.33	1.1	4625	154	109	0.85	0.05	2.86	0.65	7.4	6.6	8.5	1
J083524-560214	1	272.35	-9.22	0.08	1.3	2810	80	36	0.39	0.23	2.24	0.57	2.1	2.3	7.5	2
J083526-541935	2	270.95	-8.22	0.06	1.8	17025	107	102	0.00	0.14	1.72	0.49	1.0	1.5	8.9	3

3.4.2 Reliability Space

Using the SoFiA output, we can plot the reliability space described by equation 2.1. Consider the positive and negative objects in the cube separately, as in Figs. 3.5 & 3.7. The results from Mosaic 1 with $R \geq 0.9$ are used for this demonstration. The objects naturally have a discrete and irregular distribution. In SoFiA 's reliability step, the distribution is convolved with a Gaussian kernel, transforming the discrete data sets into a positive and a negative density field (Figs. 3.6 & 3.8, respectively). These (three-dimensional) positive and negative density fields can be probed at any location to obtain a positive-density value P and a negative-density value N. The reliability at that location is calculated by $R = \frac{P-N}{P}$ (equation 2.1).

Figure 3.10 illustrates (in two-dimensions) the result when transforming the original cube into the reliability space. The darker purple areas are regions with higher reliability and the yellow crosses mark the objects in Mosaic 1 with $R > 0.9$. By definition, all the objects with high R values reside in areas of high reliability density.

3.4.3 Distributions of HI parameters

By looking at the distributions of various parameters, we can look for possible trends and relationships that could potentially reveal biases within SoFiA . Using equation 2.3, the beam area (Ω) for Mosaic 1 and Mosaic 2 is calculated as 26.5 and 16.6, respectively. Correcting for the beam and multiplying by the channel width (Δz) of 11 $\mathrm{km\,s^{-1}}$, the integrated flux (S_{int}) of a source is given by:

$$S_{\mathrm{int}}(\mathrm{Mosaic\ 1}) = f_{\mathrm{int}} \times \frac{\Delta z}{\Omega_1} = f_{\mathrm{int}} \times 0.417 \tag{3.2}$$

$$S_{\mathrm{int}}(\mathrm{Mosaic\ 2}) = f_{\mathrm{int}} \times \frac{\Delta z}{\Omega_2} = f_{\mathrm{int}} \times 0.666 \tag{3.3}$$

Similarly, the peak flux density (f_{peak}) of the object can be corrected for the beam and converted to S_{peak}.

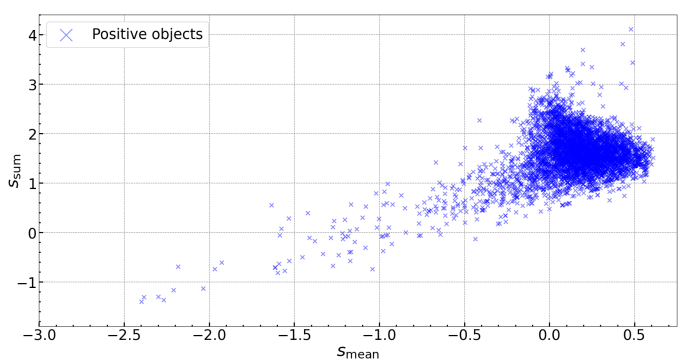

Figure 3.5: Distribution of objects with positive flux in the parameter space used by SoFiA.

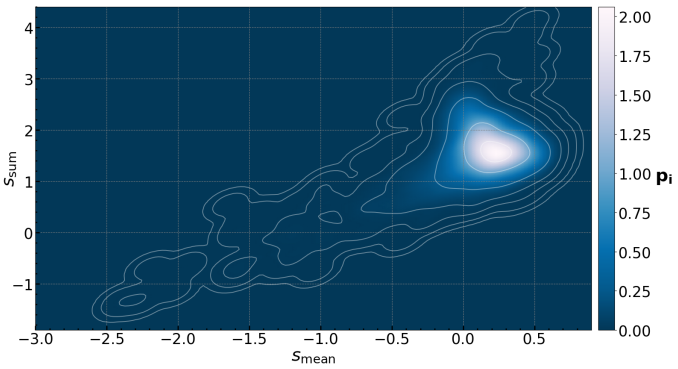

Figure 3.6: Density of objects with positive flux in the parameter space used by SoFiA. Contour levels: 1e-4, 1e-3, 0.01, 0.05, 0.25, 1.0, 1.75

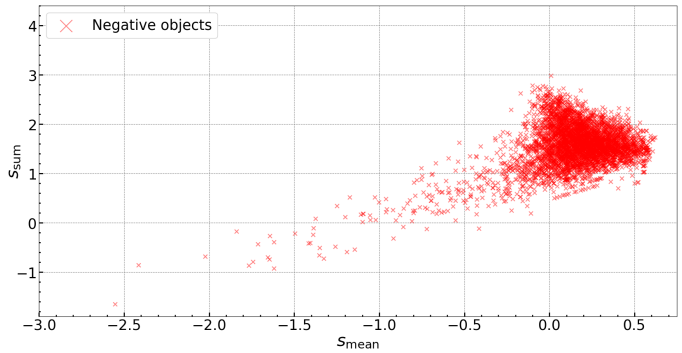

Figure 3.7: Distribution of objects with negative flux in the parameter space used by SoFiA.

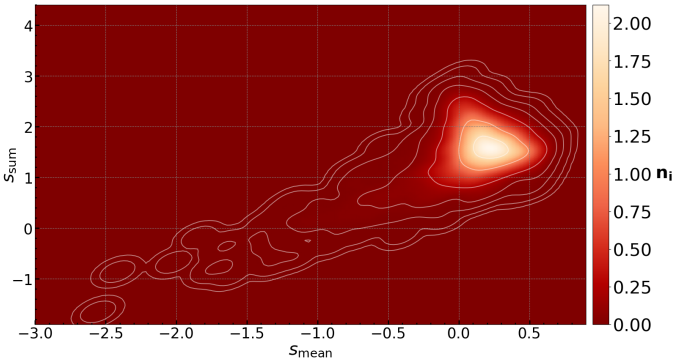

Figure 3.8: Density of objects with negative flux in the parameter space used by SoFiA. Contour levels: 1e-4, 1e-3, 0.01, 0.05, 0.25, 1.0, 1.75

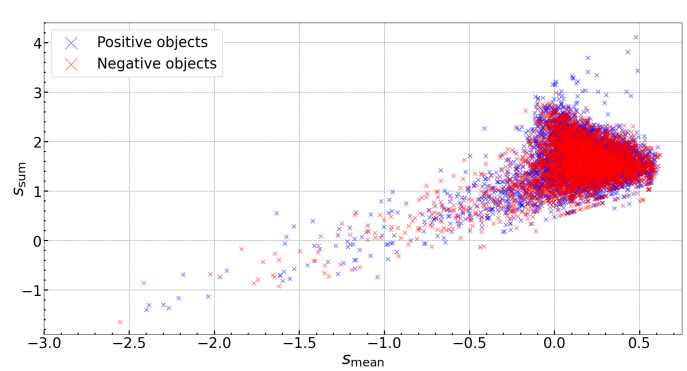

Figure 3.9: Distribution of positive and negative objects in the parameter space used by SoFiA.

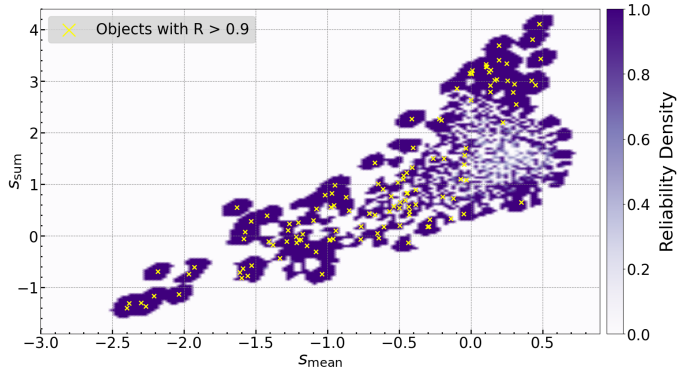

Figure 3.10: Reliability density in the parameter space used by SoFiA.

Figure 3.11 shows the distributions of various parameters of the 119 galaxy candidates (the galaxy candidates classified as category 1 or 2): panels A-D show $S_{\rm peak}$, $S_{\rm int}$, W_{20}, and local rms (measured by SoFiA) around the source. Detections that SoFiA catalogued as real are shown in red and additional detections that were retrieved (explained in Sect. 3.3.3) are in green.

Panel A shows the detections are evenly dispersed in terms of $S_{\rm peak}$, meaning that SoFiA showed no noticeable dependency on this parameter. On the other hand, panel B reveals that SoFiA shows a bias towards galaxies with higher $S_{\rm int}$. The histogram shows a sharp divide between detections that SoFiA catalogued as real (red) and the remaining objects that received a reliability of $R < 0.7$ (green). This is a good result because $S_{\rm peak}$ is biased towards noise peaks, while $S_{\rm int}$ is more likely to be associated with real sources.

Panel C suggests there is also a dependency on line width. A large fraction of the low line width galaxies were rejected by SoFiA . It appears as though SoFiA 's sensitivity to HI sources depends on the velocity width and the integrated flux (which are related parameters).

Panel D reveals that the majority of the sources have a local rms higher than the global mosaic rms of 1.2 mJy beam^{-1} (marked by the black dashed line).

The analysis of the local rms noise around the sources can be taken further by looking at the SNR distribution. Figure 3.12 compares the SNR when calculated with the global rms of 1.2 mJy beam^{-1} (left panel) versus the local rms (right panel). When measuring the completeness of SoFiA using the global rms, at first it might appear that SoFiA did not meet the criteria of finding all sources above $5-6\sigma$ ($5\times$ rms noise; Westmeier et al., 2021); however, the higher local rms is a factor that would appear to underestimate the true completeness — which would be higher if the SNR calculation used the local rms instead of the global mosaic rms (right panel). Looking at the green distribution, when assuming an rms of 1.2 mJy beam^{-1} for all detections (left panel), 21 detections above 5σ escaped the final SoFiA catalog. When the variable local rms is taken into account (right panel), SoFiA came considerably closer to the completion target: missing only 7 (5.9%) sources of 5σ or higher (and only two sources $\geq 6\sigma$).

There are two possible explanations for the higher local rms values. Firstly, recall from Sect. 3.1, our search area extends further than the nominal HPBW (to an on-sky radius of $\sim 0.67°$), and because we included detections from these noisier edge-regions, the average local rms will be somewhat higher than the typical rms of the mosaics (which is measured within a central box). Secondly, a high local rms could be an indication that source flux has inadvertently been added to the measurement of the noise flux. Indeed, in the Chapter 4 analysis, it was found that SoFiA 2 tends to overestimate the local rms.

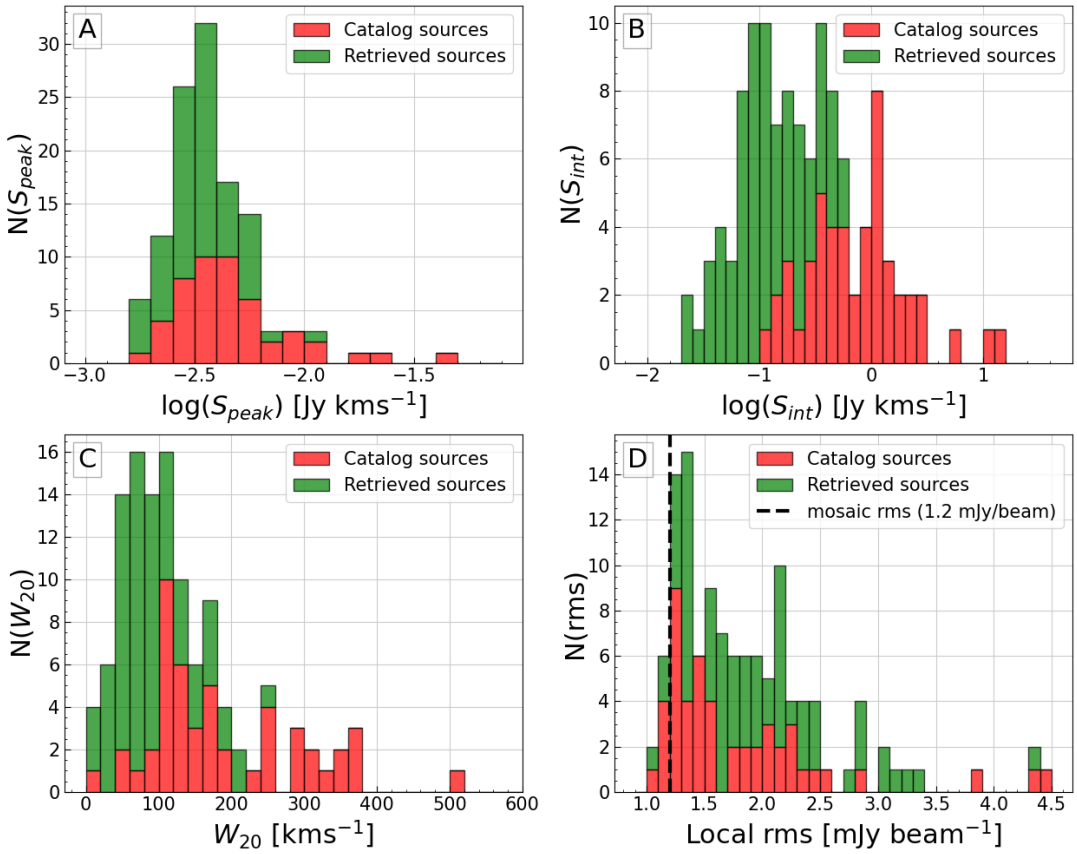

Figure 3.11: Distributions of parameters of the 119 reliable galaxy candidates. Top left/panel A: peak flux ($S_{\rm peak}$) in logarithmic scale. Top right/panel B: integrated flux ($S_{\rm int}$) in logarithmic scale. Bottom left/panel C: line widths at 20% of the peak flux (W_{20}). Bottom right/panel D: local rms around the source (as measured by SoFiA).

Therefore I want to issue a word of caution: although this chapter makes use of SoFiA 1, it is possible that the local rms measurements described above are roughly 10% too high.

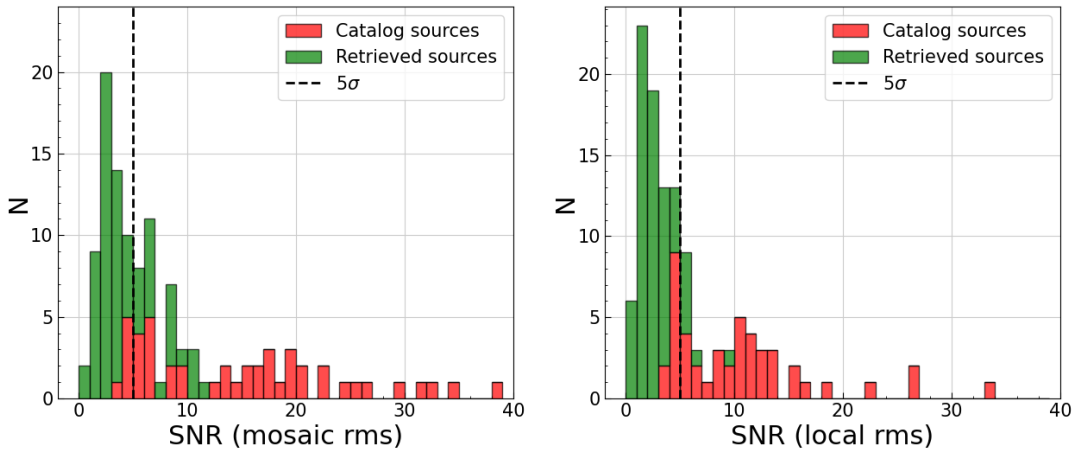

Figure 3.12: Signal-to-noise ratio (SNR) of the detections calculated with the global measured rms of 1.2 mJy beam^{-1} (left) and with the local rms of the individual sources (right).

3.4.4 Large Scale Structure in the MeerKAT16 Data

As a secondary analysis, we again use the 119 strongest detections (category 1 & 2) to look at the distribution of HI gas detected around the galaxy cluster VC04 (Kraan-Korteweg et al., 2017) and interpret the structure.

Figure 3.13 shows the redshift distribution of the galaxy detections, with a corresponding wedge diagram beneath that shows Galactic longitude. The green data show a sample of galaxies which are centred on the VC04 cluster (ℓ, b, cz) $\approx$ (272.25°, -9.0°, 18 000 km s^{-1}), taken by the Infrared Survey Facility (IRSF), hosted by the South African Astronomical Observatory (SAAO) in Sutherland and have optical redshifts measured with the AAOmega instrument on the Anglo-Australian Telescope (courtesy Hatamkhami, 2022).

Even though 119 is a relatively small sample, this plot reveals regions of spectral overdensities, separated by a region almost completely devoid of HI detections at $cz \sim$14 000 km s^{-1}. The black histogram shows a peak around $cz \sim$18 000 km s^{-1} — a signature of the main VSCL wall (Kraan-Korteweg et al., 2016, 2017). The group of galaxies around $cz \sim$21 000 km s^{-1} is likely associated with the secondary wall.

The IRSF sample shows that VC04 is clearly a rich cluster, independently supported by the fact that no HI detections are found within one Abell radius (cross-matching with the MeerKAT16 catalog returns no matches). The discernible lack of HI galaxies around the core of VC04 can be explained by intra-cluster movement. The interactions of galaxies with each other in a dense environment has caused them to be stripped of their gas. There

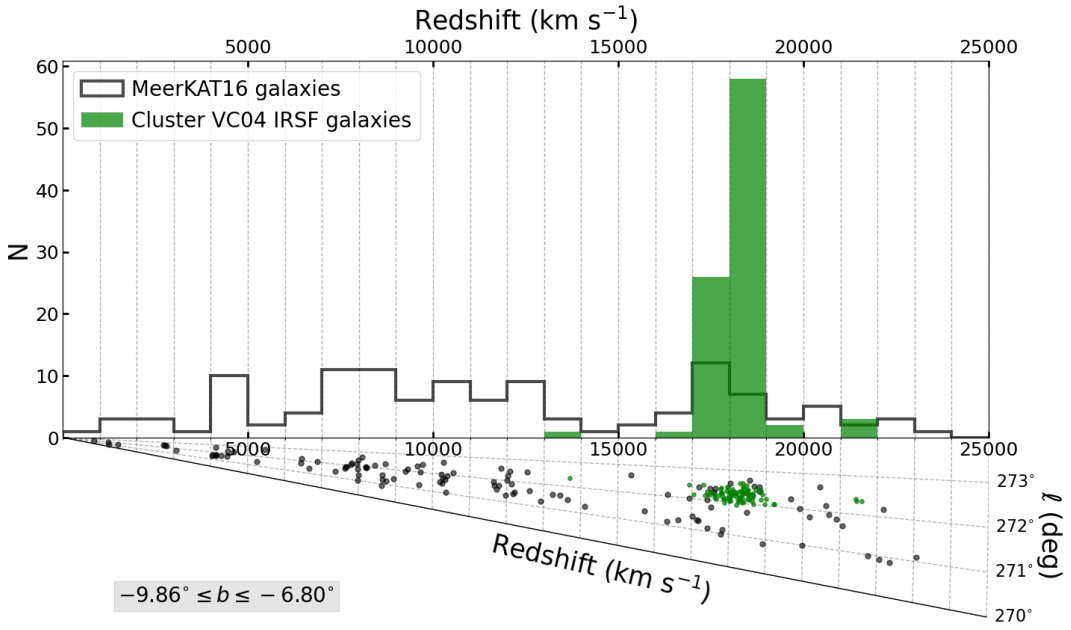

Figure 3.13: Velocity (redshift) distribution (top) with corresponding wedge diagram (bottom) revealing the Galactic longitude distribution with redshift. The 119 reliable MeerKAT16 galaxy detections are shown in black. In green is a sample of IRSF galaxies with known redshifts within one Abell radius of the cluster VC04 (courtesy, Hatamkhami, 2022).

would still be some HI gas inside the cluster, but it is possible that the sensitivity limit of the survey is too high to detect the low column density gas.

In the next section, we will extend this picture further by considering not only the positions of the galaxies, but also their $M_{\rm HI}$.

3.4.5 HI-Mass Distribution

The distribution of the derived HI masses ($M_{\rm HI}$) as a function of heliocentric velocity ($V_{\rm hel}$) is presented in Fig. 3.14. Sensitivity curves are generated for assumed line widths of 100, 200 and 400 km s^{-1} using equation 2.7, where the SNR is chosen as 5σ, the rms is the global measured rms of 1.2 mJy beam^{-1} and the spectral channel width (Δz) is 11 km s^{-1}. The sensitivity curves represent the theoretical $M_{\rm HI}$ sensitivity limit ($M'_{\rm HI}$) of the MeerKAT16 survey with respect to a 5σ HI detection.

The distribution around the mean mass of 1.2×10^9 $M_\odot$ (right hand panel) is explained by the Malmquist bias (Gould, 1993): the nearby volume is dominated by low $M_{\rm HI}$ galaxies,

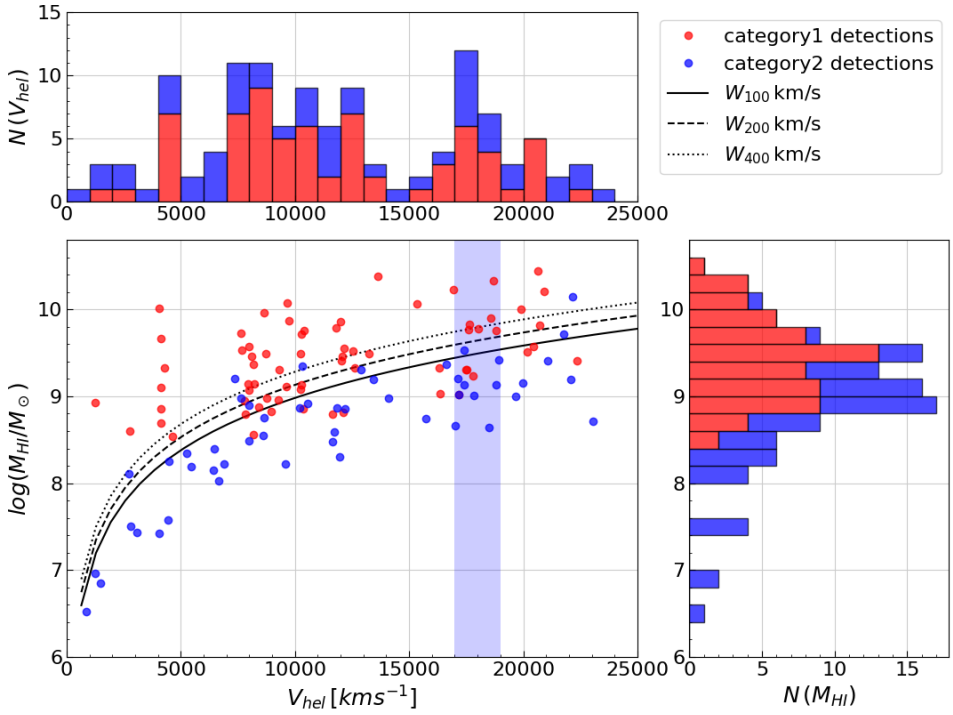

Figure 3.14: Main panel: the distribution of the logarithmic HI masses as a function of heliocentric velocity ($V_{\rm hel}$) for the 119 reliable galaxy detections, showing sensitivity curves at W_{50} = 100, 200 and 400 km s^{-1} with rms = 1.2 mJy beam^{-1} and assuming a 5σ detection. The shaded region indicates the Vela distance. Top panel: distribution of $V_{\rm hel}$. Right panel: distribution of the logarithm of the HI masses.

with high-$M_{\rm HI}$ galaxies being relatively rare, whilst the distant volume is dominated by intrinsically high $M_{\rm HI}$ galaxies, due to the inability of HI-sensitivity limited surveys to detect low $M_{\rm HI}$ galaxies at far distances. The increasing search volume with distance also presents more opportunity to detect galaxies towards the far end of the survey. These factors result in the reasonably symmetric distribution around the mean $M_{\rm HI}$, with just seven dwarfs with low $M_{\rm HI}$ ($< 10^8\,M_\odot$) detected in the local volume.

In the main panel in Fig. 3.14, the category 1 detections (red) and the category 2 detections (blue) are bisected by the sensitivity curves, with category 1 and category 2 detections falling above and below the curves respectively. This meets expectation and bodes well for our preceding classification strategy. The velocity detection distribution shows uniform coverage across the survey bandwidth, including nineteen galaxy candidates at the VSCL distance (the blue shaded region; 17 000 – 19 000 km s^{-1}).

The target sensitivity of the survey was to reach a 5σ $M_{\rm HI}$ completion limit of

$\log M_{\rm HI} = 9.5\,M_\odot$ for a typical line width of 200 $\rm km\,s^{-1}$ at the Vela distance (cz ~18 000 $\rm km\,s^{-1}$ or 260 Mpc; Kraan-Korteweg et al., 2016), indicated by the middle sensitivity curve in Fig. 3.14. This limit is a factor ~2.5 less than the characteristic $M_{\rm HI}$ of $\log \rm M^*_{HI} = 9.86\,M_\odot\,h_{70}$, as derived by Zwaan et al. (2005) by fitting a Schecter function to the HIPASS data (Meyer et al., 2004).

The $M_{\rm HI}$ limit around the position of VC04 (blue shaded region) is high ($\gtrsim 10^{9.5}\,M_\odot$), and since cluster members typically have lower $M_{\rm HI}$ compared to field galaxies (due to tidal stripping of their HI gas; Lah et al., 2009), this could be a contributing factor to the lack of detections close to the cluster center (cf. Fig.3.13).

Figure 3.14 shows that roughly half of the galaxy detections fall below the $M_{\rm HI}$ completion limit for a 5σ detection. Some of these lower points are $<5\sigma$ detections, since the galaxy search intentionally went very deep. Another factor that contributes to this outcome is the line width parameter. The sensitivity curves are dependent on line width, and about a third of the W_{20} values are <75 $\rm km\,s^{-1}$ (as measured by SoFiA), which would place the points below the 100 $\rm km\,s^{-1}$ sensitivity curve.

3.4.6 MeerKAT16 Summary

A concerted effort has been made to generate a robust and reliable source catalog from the MeerKAT16 HI line data. A visual detection method was invoked involving two persons and an independent adjudicator. The visual detections underwent several cycles of verification and updates, resulting in a well constructed catalog. The method of visually identifying HI sources results in a high level of accuracy but a major drawback of this method is the time it takes to process a data cube thoroughly. As technology improves and data cubes become larger, identifying sources visually becomes impractical. Now that astronomy has entered the age of "big data", astronomers are heavily relying on automated source finders.

The visual source list underwent a quantitative comparison with the results from the automated source finder SoFiA . The cross-comparison procedure (Sect. 3.3.2) found that 41% of the 119 final galaxy detections had counterparts in the SoFiA catalog. The other 59% did not pass the algorithm's reliability criteria (but were retrieved for analysis through the use of SoFiA 's diagnostic tools). Looking at the detections that failed SoFiA 's reliability threshold (Fig. 3.11), their distributions lean towards lower integrated flux ($S_{\rm int}$) and lower line widths (W_{20}), perhaps indicating that SoFiA 's algorithms are not well matched for dwarf galaxies, or low column-density detections.

Numerous quality assurance checks were performed in order to confirm the accuracy

of the cross-matching technique and the appropriateness of the chosen tolerances (120" and 400 km s^{-1}). Cross-matching positional data can be surprisingly complicated. Even if a single algorithm could be devised that is optimum in all situations and for all coordinate systems, the number of matches is still dependent on user-selected tolerances, and hence will always have a degree of randomness. Another important factor to recognise is that a strict one-to-one match-up is not guaranteed. Sources in catalog A can have multiple acceptable matches in catalog B and vice versa. For example, in the Mosaic 2 cross-match, 21 visual detections matched to 19 unique SoFiA detections. Several factors, including but not limited to the ones just mentioned, cause cross-matching positional data to have an intrinsic uncertainty.

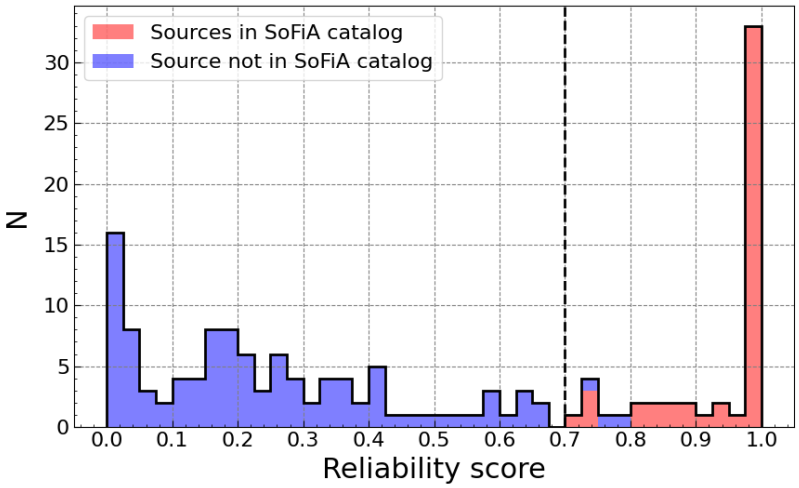

Figure 3.15: The distribution of the reliability scores (R) of the 119 MeerKAT16 detections. The dotted line indicates the user-defined reliability threshold $R = 0.7$, below which all objects are discarded. ~ 79% of the sources have R<0.4 and ~ 67% have R<0.3.

As described in Chapter 1, SoFiA assigns all individual detections a reliability score R between 0 and 1. The ideal scenario would be for all real sources to pass the reliability criteria to make it to the final catalog. Our results show the majority of the visual detections did not pass the reliability filter. While it might be instinctive to lower the reliability cut-off to let more "real" sources cross the threshold, unfortunately this logic is incorrect; as shown in Fig. 3.15, close to 80% of the sources in our final catalog have $R < 0.4$. This proves that a lower R cut-off does not guarantee a higher completeness. This is a consequence of the negative-source method for determining reliability (Serra et al., 2012, described in Sects. 2.1.3 & 3.4.2). There are too many negative sources in the same region of reliability space (s_{mean}, s_{sum} and s_{max}) where these fainter, visually-found objects

reside, and therefore, their reliability is low. The root of this problem is that the noise in the data is not perfectly Gaussian (as assumed by SoFiA) and it is impossible to correct for this by adjusting parameter settings (private communication: J.M. van der Hulst). The only way to improve upon this issue is to correct for artifacts or flag bad data prior to running the S+C finder.

This MeerKAT16 pilot project has provided important insight into the source finding strategies for future surveys and served as a precursor project for subsequent HI MeerKAT Large Survey Projects (e.g., Fornax and Laduma). Techniques, procedures and computational methods established in this analysis are factored into the second part of my research, pertaining to the MeerKAT Galactic Plane Legacy Survey (GPS), in Chapter 4.

Chapter 4

MeerKAT GPS – the Great Attractor Connection

With the goal of mapping the large scale structure of galaxies behind the Zone of Avoidance (ZoA), we present here the 21 cm HI spectral line observations taken by the MeerKAT Galactic Plane Legacy Survey (henceforth GPS). Of particular interest is the dynamically important Great Attractor (GA) region — a nearby ($\sim$4500 km s^{-1}; Kraan-Korteweg et al., 1996) wall-like supercluster originally inferred from a strong inflow of galaxies (Dressler et al., 1987; Lynden-Bell et al., 1988; Dekel, 1994), and later confirmed through observational evidence (Kraan-Korteweg et al., 1996; Juraszek et al., 2000; Woudt & Kraan-Korteweg, 2001).

4.1 GPS Specifications and Predictions

From July 2018 to the end of 2019, GPS surveyed the innermost strip of $\Delta b \simeq 3^\circ$ along the southern Galactic plane ($248^\circ \leq \ell \leq 60^\circ$), with the main scientific goal to study Galactic objects. However, here we are exploiting GPS to trace the large scale distribution of gas-rich galaxies located behind the Milky Way out to $z \lesssim 0.08$ (respectively $V_{\rm hel} < 25\,000$ km s^{-1}).

Numerical simulations for the GPS survey were obtained courtesy of L. Staveley-Smith. These simulations use the same code as for the SKA HI science case (Staveley-Smith & Oosterloo, 2015), but tuned to the GPS specifications: including an rms of 0.45 mJy beam^{-1}, a beam size of 23", 4k velocity resolution and an on-sky area of 528 deg^2.

The predictions are based purely on cosmological constraints, and galaxies are distributed randomly with a space density determined by the HI mass function (HIMF)

derived by Zwaan et al. (2005). This HIMF is the 2D HI mass-velocity width function derived from HIPASS data. Galaxy sizes were assigned using the HI mass-size relation.

The simulations predict GPS to be sensitive to all normal spirals at the GA distance, furthermore reaching into the dwarf regime: a 5σ galaxy detection of line width $80\,\mathrm{km\,s^{-1}}$ results in $M_{\mathrm{HI}} = 10^8\,M_\odot$ at $V_{\mathrm{hel}} = 4000\,\mathrm{km\,s^{-1}}$. Out to the full distance we are complete to $M_{\mathrm{HI}} \gtrsim 10^{10}\,M_\odot$. Therefore, GPS offers great potential for tracing interesting hidden structures, such as the crossing of the GA wall, the boundaries of the Local Void and possible links emerging from the Ara and Triangulum-Australis clusters ($\sim$15 000 $\mathrm{km\,s^{-1}}$; Kraan-Korteweg & Woudt, 1999; Woudt & Kraan-Korteweg, 2001).

4.2 Aim

For my analysis of GPS, we constrained the on-sky survey region to $302^\circ \leq \ell \leq 332^\circ$; $-1.5^\circ \leq b \leq 1.5^\circ$ within the volume $0 < V_{\mathrm{hel}} < 25\,000$ $\mathrm{km\,s^{-1}}$, with particular focus on the GA distance range ($\sim$3000 – 7000 $\mathrm{km\,s^{-1}}$; Woudt et al., 2008).

This chapter contains a brief description of the data reduction and imaging process, followed by an assessment of the data quality. The data analysis involves a source-finding procedure with the Source Finding Application (SoFiA; Serra et al., 2015; Westmeier et al., 2021), in combination with visual verification, to generate a robust catalog of galaxy candidates. Galaxies published in HIZOA (Staveley-Smith et al., 2016) are compared in detail to their GPS counterparts and used for a verification of GPS HI parameters. Finally, we interpret the large scale structures revealed by the GPS data.

4.3 A Deeper HI Survey of the Inner ZoA

Until now the deepest systematic HI survey of the *southern* Galactic plane has been done using the Multibeam Receiver on the 64 m Parkes radio telescope (Staveley-Smith et al., 2016). Conducted between between 1997 and 2000, the Parkes deep HI Zone of Avoidance survey (henceforth HIZOA) surveyed the southern ZoA between $|b| \leq 5^\circ$ and $212^\circ \leq \ell \leq 36^\circ$ with an rms sensitivity of 6 mJy beam^{-1}, a 15.5' beam size, a 4' pixel size and a maximum recessional velocity of $cz \simeq 12\,700\,\mathrm{km\,s^{-1}}$. The detection rate decreases rapidly after the GA distance, and at velocities further than $7000\,\mathrm{km\,s^{-1}}$ HIZOA detected mostly HI-massive galaxies ($\gtrsim 5 \times 10^9\,M_\odot$).

The low resolution resulting from single-dish data makes it difficult to separate out HI detections when the number density of galaxies is high — such as in the GA region or areas filled with continuum emission — which leads to confusion between galaxies in the

beam. These confusion problems intensify with increasing survey depth (Kraan-Korteweg et al., 2008b), therefore there is a notable trade-off between depth and resolving ability.

Designed to detect typical spiral galaxies at the distance of the GA, HIZOA had a detection rate of 1 galaxy per 2 deg^2 on average, cataloging a total of 883 galaxies. Current surveys with the full MeerKAT array, such as GPS, goes more than an order of magnitude deeper and, being an interferometer, at much better spatial resolution.

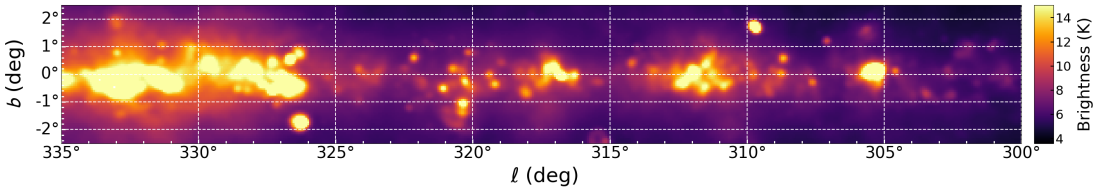

Figure 4.1: The 1.4 GHz radio continuum image based on the HI Parkes All-Sky Survey (HIPASS) data, dubbed as CHIPASS (Calabretta et al., 2014). The colour gradient corresponds to temperature in units of K.

The inner ZoA is subject to strong background continuum radiation which further increases towards the Galactic bulge ($\sim 30^\circ > \ell > 350^\circ$). Bright continuum reduces detectability through raising the receiver temperature and inducing waves into the spectral baseline (Staveley-Smith et al., 2016). The temperature of the background continuum for the L-band between $300^\circ < \ell < 350^\circ$ is displayed in Fig. 4.1, taken from Calabretta et al. (2014). This map shows a steep rise occurring at $\ell \gtrsim 325^\circ$. The HIZOA detection rate was diminished by high continuum temperature, with detection rates starting to drop from $T_B > 7$K and reaching zero above $T_B \sim 16$ K (see Fig. 7 in Staveley-Smith et al., 2016).

Flux originating from HI galaxies compete with the bright radio continuum shown in Fig. 4.1, therefore meticulous continuum subtraction is required as part of the GPS data reduction.

4.4 GPS Data Collection and Reduction

The GPS observations relevant to the GA region were carried out between July and December 2018 using MeerKAT's L-band receiver. The survey typically utilised 60-dish MeerKAT64 subarrays in conjunction with the SKARAB-4k correlator, providing 4096 channels across the bandpass and a channel width of 209 kHz (44.1 km s^{-1} at $z = 0$). The channel resolution is coarse in comparison to the 11 km s^{-1} resolution of the MeerKAT16

pilot project (detailed in Chapter 3), while the one of HIZOA is 27 $\mathrm{km\,s^{-1}}$ after Hanning smoothing.

The observational parameters for the $30° \times 3°$ GPS region analysed in this chapter (henceforth called the GA-GPS region) are compared to the HIZOA survey parameters in Table 4.1.

Parameter	GPS (GA region)	HIZOA
Date of observations	2018 – 2019	1997 – 2000
Galactic longitude	$302° \leq \ell \leq 332°$	$212° \leq \ell \leq 36°$
Galactic latitude	$-1.5° \leq b \leq 1.5°$	$-5° \leq b \leq 5°$
Velocity range	$cz \leq 25\,000$ $\mathrm{km\,s^{-1}}$	$cz \leq 12\,740$ $\mathrm{km\,s^{-1}}$
Velocity resolution	44.1 $\mathrm{km\,s^{-1}}$	27 $\mathrm{km\,s^{-1}}$*
Beam size	~31" × ~26"	15.5'
Pixel size	3"	4'
Integration time	~3600 s	25 min
Measured rms	0.3 – 0.5 mJy	6 mJy

*after Hanning smoothing

Table 4.1: Observational parameters for the MeerKAT GPS survey and the HIZOA survey (Staveley-Smith et al., 2016).

Calibration, imaging and mosaicking of the GA-GPS data were completed by me on the Ilifu cloud computing facility,[1] hosted by the Inter-University Institute for Data Intensive Astronomy (IDIA)[2]. The frequency range between 1308 and 1430 MHz was processed, excluding the band of Milky Way emission (1419.46 – 1421.35 MHz). This range constitutes a mostly RFI-free range over the MeerKAT bandwidth of the L-band receiver. In velocity terms, this means probing distances out to ~25 000 $\mathrm{km\,s^{-1}}$: far enough that it includes the volume most relevant to bulk flow analysis, with excellent sensitivity at the distance of the GA overdensity (~3000 – 7000 $\mathrm{km\,s^{-1}}$).

The visibility data were transferred from the SARAO archive to Ilifu and reduced with CARACal[3], an automated end-to-end pipeline for the reduction of radio interferometry data (Józsa et al., 2020). CARACal makes use of commonly-used radio interferometry software packages, such as CASA, WSClean and Montage. The general strategy for the data reduction includes flagging bad data (e.g., RFI), cross-calibration, self-calibration, direction dependent calibration, Doppler-tracking correction, and continuum fitting and subtraction. An in-depth description of the reduction process will be presented in Chen et

[1] www.Ilifu.ac.za

[2] www.idia.ac.za

[3] Containerized Automated Radio Astronomy Calibration; https://caracal.readthedocs.io/

al., (in prep). The pertinent steps of the HI and continuum imaging and the mosaicking process is described in the next section.

4.5 Imaging and Mosaicking

The HI data were imaged with WSClean within the CARACal pipeline using a pixel scale of 3" and a Briggs robust weighting of $r = 0$. Since we chose not to deconvolve the data, the point spread functions (PSF's, or 'dirty beams') have 'side-lobes' next to the main lobe. To achieve a more Gaussian-like PSF, we employed a UV-tapering of 15", which increases the beam size from $\sim 11 \times 9$ arcsec^2 to an average of $\sim 31 \times 26$ arcsec^2. The decrease in angular resolution does not affect our science goals — the data are sensitive to nearby galaxies as well as the more distant (more high column-density) galaxies at larger distances.

Figure 4.2 compares the PSF resulting from no tapering, to the PSF resulting from a 15" taper. Flux derivation assumes a Gaussian beam, therefore the presence of side-lobes, as seen in the left panels of Fig. 4.2, can lead to large errors when deriving flux values.

A total of 157 partly overlapping dirty HI cubes were constructed. The borders of the field-of-view was defined at 20% sensitivity, fixing the radius of each individual pointing at $\sim 0.8°$. Following this, the images were corrected for primary beam attenuation using the method described in Mauch et al. (2020).

The CARACal pipeline was implemented again to construct ten HI mosaics ('T10' through 'T19' according to GPS nomenclature), each consisting of 22 pointings. The central $\Delta\ell \approx 3°$ will be used for analysis, as this strip has near uniform sensitivity given the hexagonal sampling pattern and small offsets between pointings. The GPS continuum data were likewise imaged with a pixel size of 3" and constructed into two-dimensional mosaics of 22 pointings, complementary to the HI mosaics. An example of one continuum mosaic and the corresponding HI mosaic (one plane) is shown in Fig. 4.3. Despite the numerous continuum sources visible in the left panel, the rms noise is quite homogeneous over the central image, albeit with some residual baseline ripples.

Each mosaic spans an on-sky area of $\sim 5° \times 3.5°$ (edge-to-edge) and overlap each other by a generous $\Delta\ell \approx 2.5°$. The large overlaps ensure extended sources are not intersected at the borders and, in addition, the overlap area provides opportunity to compare source-finding results from neighbouring mosaics.

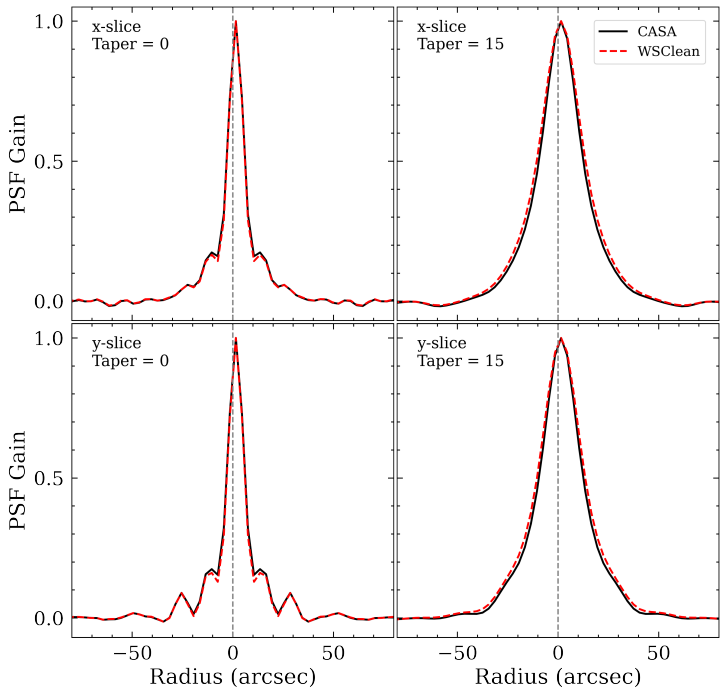

Figure 4.2: Left panels: dirty PSF resulting from robust 0, without a taper. FWHM is ~12" but wavy side-lobes are present next to the main lobe. Right panels: dirty PSF resulting from robust 0 and a 15" taper" resembles a more Gaussian distribution, with a FWHM of ~31" × ~26". (Figure courtesy of S. Rajohnson).

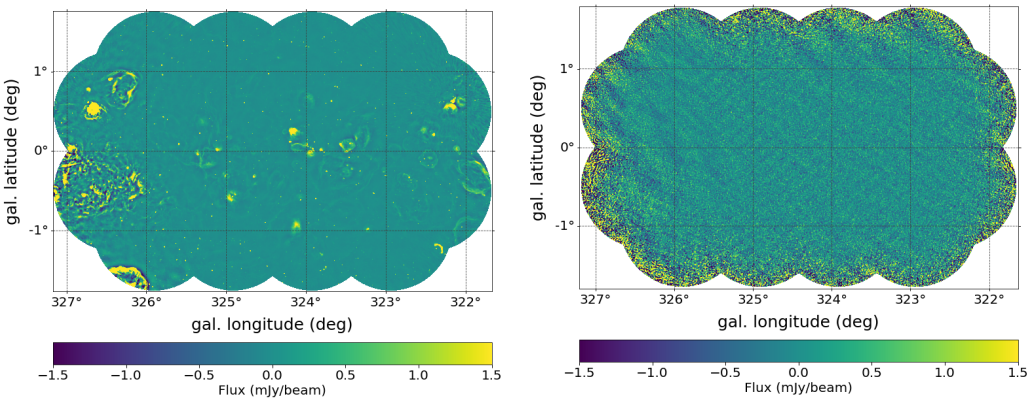

Figure 4.3: Left: A continuum mosaic (T12), containing some compact continuum sources as well as diffuse continuum – particularly around $\sim 326^\circ - 327^\circ$. Right: A channel map of an HI mosaic (T12), the green-hued colour scale indicates the noise variations (mean rms = 0.42 mJy beam^{-1}).

CARACal produced all mosaic cubes in equatorial coordinates. However, because GPS runs directly along $b = 0°$, display and analysis along the Galactic plane is more straight forward. Additionally, when the mosaics are oriented in terms of Galactic longitude/latitude, it allows us to define a rectangular search area in Cartesian coordinates (further explanation in Sect. 4.7.1). Therefore, all mosaics were converted to Galactic coordinates using CASA.

The mosaics did not go through any CLEANing procedures (Högbom, 1974). The UV-coverage is uniform and dense enough to produce a Gaussian-like PSF (cf. Fig. 4.2). CLEANing is more feasible for targeted surveys of small fields away from the Galactic plane, as opposed to large-area blind surveys with locally varying noise properties. The dirty tapered HI mosaics are sufficient for the science goals of this project, which is predominantly a quantitative study of large scale structure and the properties of this sample. Moreover, as shown in Sect. 4.10, the fluxes published by the HIZOA survey were reliably reproduced by our GPS detections.

4.6 Data Quality

In order to verify whether we are detecting and measuring HI flux accurately, several data quality assurance checks were carried out throughout the imaging process, both on the individual images and the mosaic cubes. One of the steps includes measuring the rms of all data cubes. The rms or 'root-mean-square' of the flux across the full velocity (or frequency) range, as measured within a large central plane, is calculated mathematically as $\sqrt{\sum x_i^2/N}$, in units of $\mathrm{Jy\,beam^{-1}}$.

Fig. 4.4 shows the individual HI fields as 0.5°-radii circles. The top panel shows the positions of the pointings with respect to the continuum background (the same CHIPASS image shown in Fig. 4.1). In the bottom panel the circles are coloured according to their measured rms, the mean of which is 0.51 mJy. There is a clear correlation between the regions of higher rms and the regions with stronger background continuum when comparing the top and bottom panels.

After the continuum subtraction in the imaging process, it was found that compact sources were well subtracted, but large scale variable continuum sources caused an increase in the noise of the resultant HI cubes. This effect is undesirable but typical of the Galactic plane. A representative case of such continuum can be seen in Fig. 4.3 around $\ell \sim 326.5°$.

Table 4.2 shows the variation in rms noise among the ten mosaics. The mean measured rms is 0.47 mJy, ranging from 0.39 – 0.53 mJy. The noise is higher than the theoretical

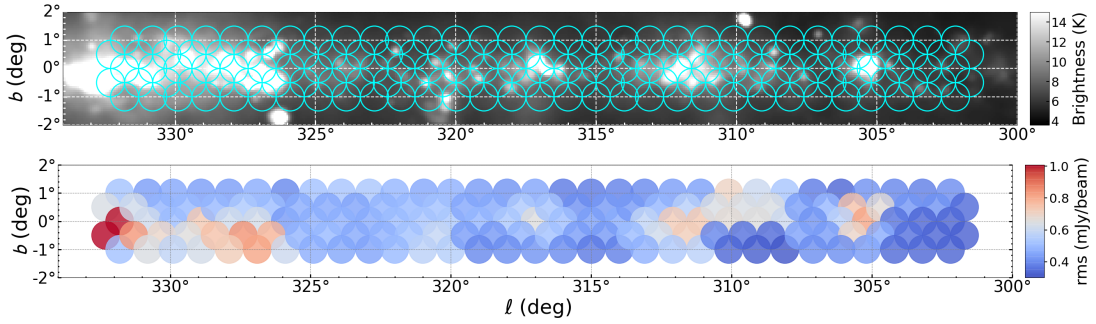

Figure 4.4: Top: CHIPASS 1.4 GHz radio continuum image (Calabretta et al., 2014) with the positions of the GA-GPS pointings overlaid in cyan, with given radii of 0.5°. Bottom: the GA-GPS fields with colours representing the measured rms of each field. Redder colours indicate a higher rms.

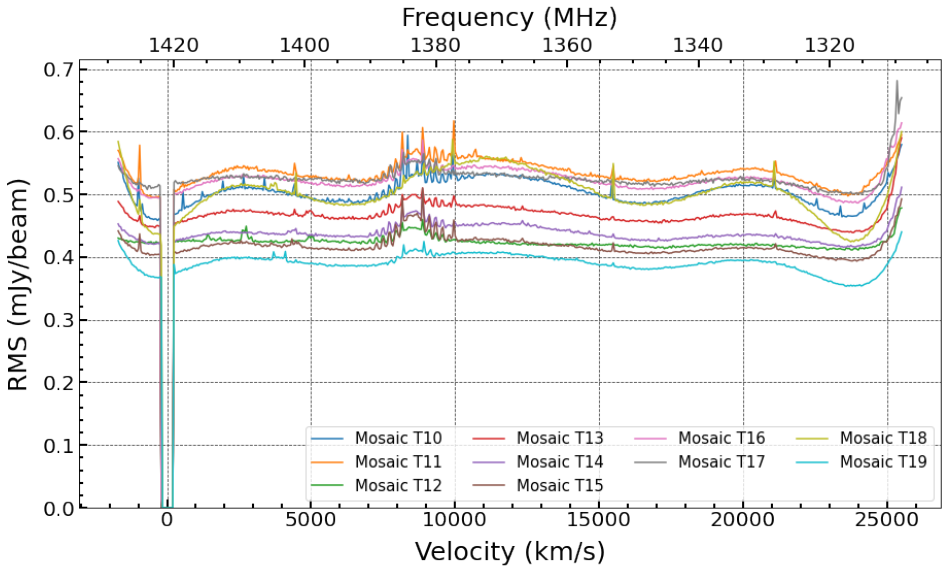

Figure 4.5: rms versus velocity in km s^{-1} (bottom axis) and frequency in MHz (top axis) as measured through the centres of the ten HI mosaics. Interference from Global Positioning Satellites can be seen in the frequency band ~1375 – 1387 MHz. Note the Milky Way band 1419.46 – 1421.35 MHz (where rms = 0) is excluded from the overall rms measurements.

rms of ~0.25 mJy (as calculated using the radiometer equation[4] and assuming natural weighting) due to a combination of the robust 0 weighting applied in the imaging step and the varying continuum background temperature (cf. Fig. 4.1).

Figure 4.5 is a plot of the measured rms throughout each mosaic, as calculated within

[4]Online noise calculator available at: https://hifi.icrar.org/

a large central plane. The band from 1376 – 1386 MHz is contaminated with RFI from Global Positioning Satellites (documented in SARAO's RFI database[5]), introducing noise peaks at this distance. With the large number of GPS satellites circling the Earth, interference has become inevitable. Automated RFI flagging as well as various other mitigation processes is standard practice in the data reduction process (e.g. Mauch et al., 2020) and works generally quite well except for GPS RFI, which has a strong signal when on. Besides these irregularities, along with some other smaller spikes, the rms is fairly consistent and the baselines are reasonably flat throughout the cubes up to ~25 000 km s^{-1} .

mosaic	ℓ	beam size	measured rms
TXX	deg	arcsecs	mJy/beam
T10	~302 – 305	28.8" × 26.1"	0.50 ± 0.019
T11	~305 – 308	28.5" × 25.3"	0.53 ± 0.016
T12	~308 – 311	32.5" × 25.9"	0.42 ± 0.005
T13	~311 – 314	33.3" × 26.6"	0.47 ± 0.012
T14	~314 – 317	32.2" × 26.3"	0.44 ± 0.010
T15	~317 – 320	30.3" × 25.9"	0.41 ± 0.009
T16	~320 – 323	30.9" × 26.4"	0.52 ± 0.015
T17	~323 – 326	32.9" × 25.2"	0.52 ± 0.009
T18	~326 – 329	30.4" × 26.1"	0.50 ± 0.033
T19	~329 – 332	29.3" × 24.5"	0.39 ± 0.013
mean		**30.9" × 25.8"**	**0.47 ± 0.014**

Table 4.2: Specifications of the ten GA-GPS mosaics ('T10' – 'T19'): positions in longitude, median beam size, and mean rms (measured within a central plane).

Another aspect of data quality assurance is inspecting the data visually for artifacts and residual continuum sources. This was done by plotting channel maps (e.g., right panel in Fig. 4.3) and position-velocity (pv) maps at various positions in the data cubes and scanning these images by eye. Most of the data have approximately uniform noise; however, since the data are known to contain some residual continuum and spectral ripples, a pv-map can expose a stripe that could hamper source extraction (a particularly pronounced stripe is captured in Fig. 4.7, Sect. 4.7.3). Although there are intricate methods available for eliminating artifacts (e.g., fitting and subtracting a high-order polynomial), they would be very time-intensive considering the large size of GPS and the

[5] https://skaafrica.atlassian.net/wiki/spaces/ESDKB/pages/305332225/Radio+Frequency+Interference+RFI

benefit to our results would be minimal. Our overall data quality is sufficient for source finding and HI parametrisation.

4.7 Source Finding

The use of an automated method of source identification is essential for the ~65 GB mosaicked data cubes. The large file-size of the GPS mosaics mean employing SoFiA 1 is not realistic because the jobs require more memory than what the Ilifu computer cluster can provide. Additionally, SoFiA 2 is much faster than the Python-based SoFiA 1. Therefore, source finding for GA-GPS was achieved with SoFiA v2.3.1 in combination with a visual search that I performed on a single mosaic — used as a template to optimise the SoFiA parameter settings for this particular survey.

4.7.1 On-sky Search Area

As is expected from the primary beam correction, the edges of the mosaics are noisy. Searching for reliable sources in these regions of high rms is not practicable, therefore an optimal search area was defined which aims to maximise coverage of the sky while evading the noisy edges.

Each mosaic was assigned a search area spanning 3° in longitude, and extended further by 0.25° on each side in order to create overlap between adjacent search areas. In latitude, the boxes were confined to $b = \pm 1.5°$. This $3.5° \times 3°$ mosaic configuration will be kept constant for the GA region and throughout the rest of the GPS strip (currently being investigated by other team members). Figure 4.6 shows an HI-plane of two super-imposed adjacent mosaics, with their respective search areas drawn in dashed lines. Note: the outer edges of the mosaics are visible in this diagram, but source-finding is performed on the mosaics individually, where the search area is uniform.

The combined search area of the ten mosaics results in a strip spanning $302° \leq \ell \leq 332°$ and $-1.5° \leq b \leq 1.5°$ — with an additional $\Delta\ell = 0.25°$ extension on each end. The highest and lowest latitudes ($b \simeq \pm 1°$–$1.5°$) do encroach upon sensitivities of <100%, but the generous overlap between mosaics means we can elude the high noise borders along the vertical edges entirely. This results in smooth fields with high sensitivity for source finding.

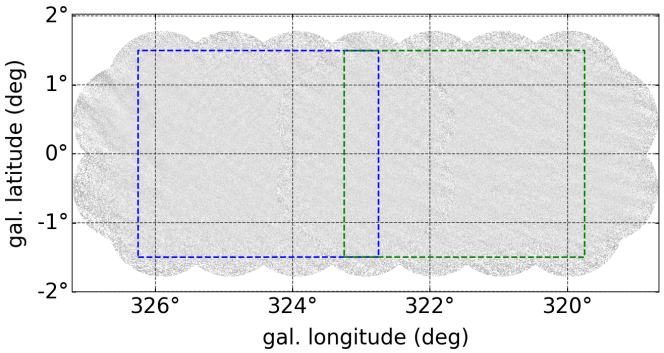

Figure 4.6: A channel map of two super-imposed adjacent mosaics (T12 and T13), illustrating the search area used for source finding (blue and green dashed lines). All the search areas cover latitudes $b \pm 1.5°$. In longitude, they each span a full 3° with an extension of 0.25° to the left and right to create overlap.

4.7.2 Visual Search of a GPS Mosaic

Searching $\sim 3.5° \times 3°$ mosaics of 570 spectral channels by eye in a consistent and timely manner is not feasible. On the other hand, for the process of optimising the SoFiA parameters, it is very advantageous to have a set of sources that have already been identified visually.

The parameters used for the MeerKAT16 survey (Chapter 3) could not be directly transferred to the GPS data for several reasons. Firstly, SoFiA v2.3.1 has undergone several changes in code and parameters compared to v1.3.2 used for MeerKAT16. Secondly, the GPS data have smaller beam sizes, smaller pixel sizes, and different noise properties. Nevertheless, working with SoFiA v1.3.2 brought about valuable understanding regarding how to fine-tune the parameters.

T12 was chosen as the representative case for the visual search because of its close proximity to the Norma Cluster ($\ell \sim 325°$) and the GA Wall (also called the Norma Wall) crossing. Therefore, it is the most likely to contain a large number of HI detections. Moreover, T12 should reveal 12 (nine inside the search area) of the 42 HIZOA galaxies in the GA-GPS region.

The visual search was executed in CARTA[6]: a remote image visualization and analysis tool (Comrie et al., 2021). Ninety-three (93) visual sources were cataloged within the search area of mosaic T12. Their positions are marked with black dots in Fig. 4.8. After cataloging the visual detections, consecutive SoFiA runs were executed on T12, adapting the parameters each time, with the aim of recovering as many of the visually-deemed reliable sources as possible.

[6]Cube Analysis and Rendering Tool for Astronomy; https://carta.readthedocs.io/en/latest/

4.7.3 Optimising SoFiA Parameters

Three of the parameters most pivotal to the success of a SoFiA run are the flux threshold (SCFIND.THRESHOLD) and the smoothing kernels (SCFIND.KERNELSXY and SCFIND.KERNELSZ). These parameters are called during the 'smooth+clip' algorithm (S+C finder, introduced in Sect. 2.1.2), when the cube is systematically smoothed spatially and spectrally with user-defined Gaussian and boxcar kernels respectively. After each smoothing iteration the global rms noise level of the smoothed cube is determined, and voxels below the user-specified flux threshold are discarded (Westmeier, 2021). The user can customise the resolution to match the size of the objects they are seeking. Furthermore, smoothing the original data cube to lower resolutions enhances the column density sensitivity, making it possible to extract fainter and more extended emission which would not have passed the flux threshold in the original cube, and thereby increasing the completeness (Serra et al., 2015).

Optimising the pipeline for the GA-GPS data involved altering the input parameters systematically and comparing each output to the list generated by the visual search. The comparisons involved a standard cross-match between the SoFiA catalog and the 93 visual sources. One SoFiA result was considered more successful than another if more of the visual sources were recovered.

Smoothing kernels are given in pixel units, therefore a beamsize of ~ 30" and a pixel size of 3" means GPS has a beamsize of roughly 10 pixels. Values for the spatial (XY) kernels were chosen in multiples of this beamsize: 0, 10, 20, 30 (where 0 means no smoothing). These kernel sizes were tested against the default kernel sizes (0, 3, 6) and produced more successful results. Three spectral (z) kernels — 0, 3 and 7 channels — were applied, corresponding to no smoothing (44 $\mathrm{km\,s^{-1}}$), ~132 $\mathrm{km\,s^{-1}}$ and ~309 $\mathrm{km\,s^{-1}}$.

During the testing of kernel sizes, the SoFiA job would sometimes terminate with a memory error. The cause was discovered to be streaks of leftover continuum that persist through the majority of the spectral axis of the mosaic. A particularly bad example is shown in Fig. 4.7, where a thin band of data is rendered unusable. Mistaking it for HI sources, SoFiA tries to parametrise these abnormally large objects and a spike in memory usage causes the job to terminate. To prevent this, the maximum z-length (LINKER.MAXSIZEZ parameter) was set to 21 pixels.

At this stage of the fine-tuning, with the kernel sizes optimised and the z-length of objects restricted, 83 of the 93 visual detections have been recovered by SoFiA . This (intermediate) result is shown in the left panel of Fig. 4.8 as orange circles. The green

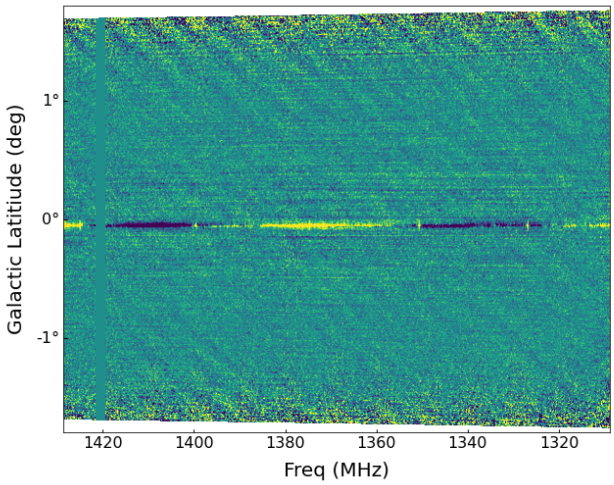

Figure 4.7: A position-velocity (pv) slice of mosaic T14 through Galactic longitude 316.8°, showing a significant stripe of continuum over the full bandwidth that is likely to cause false SoFiA detections. Any sources identified by SoFiA along this stripe cannot be trusted and must be removed from the catalog.

triangles on the same plot represent the visual detections that were recovered when increasing the maximum z-length from 21 to 31 channels; two additional visual detections were recovered, however, one detection fell away. For this reason it was decided that two SoFiA runs were necessary to maximise the detection rate of galaxies; setting a maximum z-length of 21, followed by an increase to 31. The red diamonds in the right panel of Fig. 4.8 are the visual galaxies recovered when combining the results of these two runs. Larger maxSizeZ values were tested but the results did not improve.

While optimising the settings above, the flux threshold (scfind.threshold) had been kept constant at 4.0σ — chosen as a starting value since it was found to be successful for the MeerKAT16 data (Chapter 3). As a final endeavour to recover more of the T12 visual sources, I tested flux thresholds of 3.5σ and 4.5σ. A threshold of 4.5σ (not plotted) did not identify any sources that were not already identified. The lower threshold of 3.5σ recovered two additional visual detections. This result is shown as blue squares in the right panel in Fig. 4.8. Similarly to the tests involving the maximum z-length setting, switching from 4.0σ to 3.5σ is not a perfect solution in this case because two other detections are lost. Again, an additional run is needed in order to maximise the amount of detections recovered: a threshold of 4.0σ, followed by 3.5σ.

In summary, the final source-finding process includes three consecutive SoFiA runs,

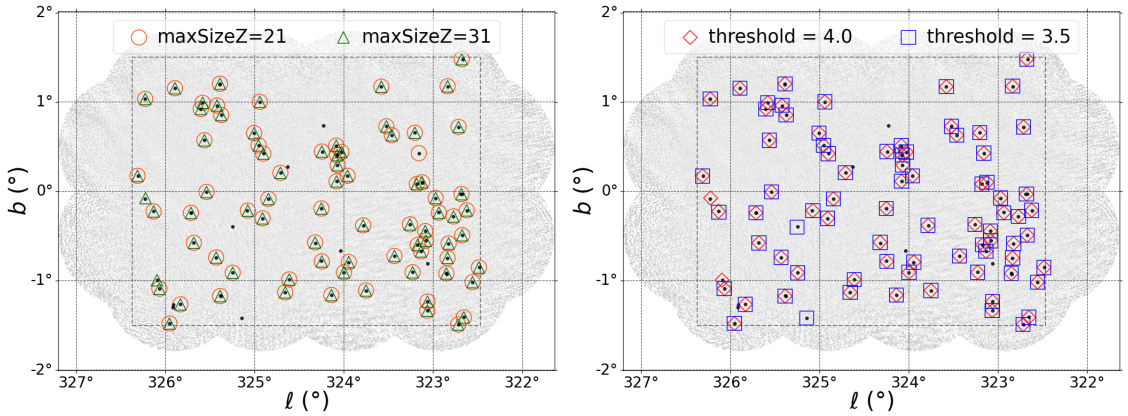

Figure 4.8: In both panels the black dots represent the visual detections found in mosaic T12. Left: Visual detections that were recovered with a flux threshold of 4.0σ and MAXSIZEZ = 21 (orange circles) versus MAXSIZEZ = 31 (green triangles). Right: the combined result from the left image (red diamonds) and the result after changing the flux threshold from 4.0σ to 3.5σ (blue squares).

changing the maximum z-length from 21 to 31 in the second run, then changing the flux threshold from 4.0σ to 3.5σ in the third run. The outputs are merged and duplicate entries are removed. The parameter settings can be found in Appendix B.

After the three runs on T12, 87 of the 93 visual detections within the search area of mosaic T12 were identified. The six visual sources that did not make the SoFiA catalog have an average local SNR $\sim 4.7\sigma$. After inspecting these sources to determine why they were not identified by SoFiA , it was found that they did not meet the linker criteria, namely: 1) spanning at least two z-channels and at least 8 pixels (24") spatially and 2) all the linked voxels having flux values higher than the user-given threshold. Even though the fluxes of the potential sources peaked at or above the flux threshold, failing these linker criteria implies they are smaller than the beamsize, rendering them unreliable.

Note, the outcome of the visual search was not taken as absolute truth. All SoFiA detections were inspected in CARTA and underwent the verification process described in Sect. 4.7.4.

The strategy of the three consecutive SoFiA runs described in this section was implemented on the other nine mosaics. This resulted in ten lengthy catalogs of detections. In a next step, each entry was adjudicated as described below.

4.7.4 Separating Real Detections and False Detections

A typical first verification process is searching for multi-wavelength counterparts; however, this is not a useful avenue for the GA-GPS survey, since none are known besides the HIZOA sources and two Spitzer Legacy program (GLIMPSE; Jarrett et al., 2007) sources (discussed further in Sect. 4.10).

For the adjudication process, moment-0 maps, moment-1 maps, and HI line profiles were created for each SoFiA source using Python's `SpectralCube` package[7]. Examples are shown in Fig. 4.9.

The moment-maps are in Galactic coordinates (degrees) and the beam size is indicated on the bottom left corners. The colour-bars on the top are in $\mathrm{Jy\,beam^{-1}\,km\,s^{-1}}$ and $\mathrm{km\,s^{-1}}$ for the moment-0 and moment-1 maps respectively.

Moment-0 maps have a 3σ-contour to represent 3 times the local rms, as measured in the corners of the moment-0 map. The white scale-bar measures 10 kpc in length — an indication if the size of the detection is reasonable for its redshift. The masked moment-1 maps are created by taking the pixels in the sub-cube which are greater than 3σ — where σ is the rms of the sub-cube — then collapsing the sub-cube into a moment-1 map. The final image is given iso-velocity contours separated by one spectral channel ($44.1\,\mathrm{km\,s^{-1}}$ at $z = 0$). Each point on the HI profile is the result of summing the flux contained in one channel of the sub-cube. The flux is corrected for the beam, giving it units of Jy.

The plots were visually assessed and the detections marked as a likely galaxy candidate or a false detection (reject). The top panel in Fig. 4.9 shows an example of what constitutes a solid detection. For a detection to be considered as likely real, the flux should be distinct from the background; about 5σ or more, and $\gtrsim 2$ beam sizes across. Perhaps the most compelling evidence of a real galaxy is a continuous velocity gradient in the moment-1 map — showing the gas approaching and receding. This feature translates to the double-horn profile seen in the right-side panel.

The bottom panel in Fig. 4.9 is a randomly selected example of a false SoFiA detection. Some signs of a false detection are a sinusoidal baseline (as in this HI profile). When there is a significant wobble in the baseline, SoFiA can mistakenly parametrise a crest as an HI source. Another sign of a false detection is a narrow line width at a high redshift, because we are not sensitive to dwarfs at high velocities. A specific phenomenon that gives rise to false detections is hydrogen recombination line emission — emitted by electrons when they drop to a lower energy level of the atom. These recombination lines are expected to originate from dense regions of the Galactic disk, and when their frequencies coincide

[7] https://spectral-cube.readthedocs.io/en/latest/

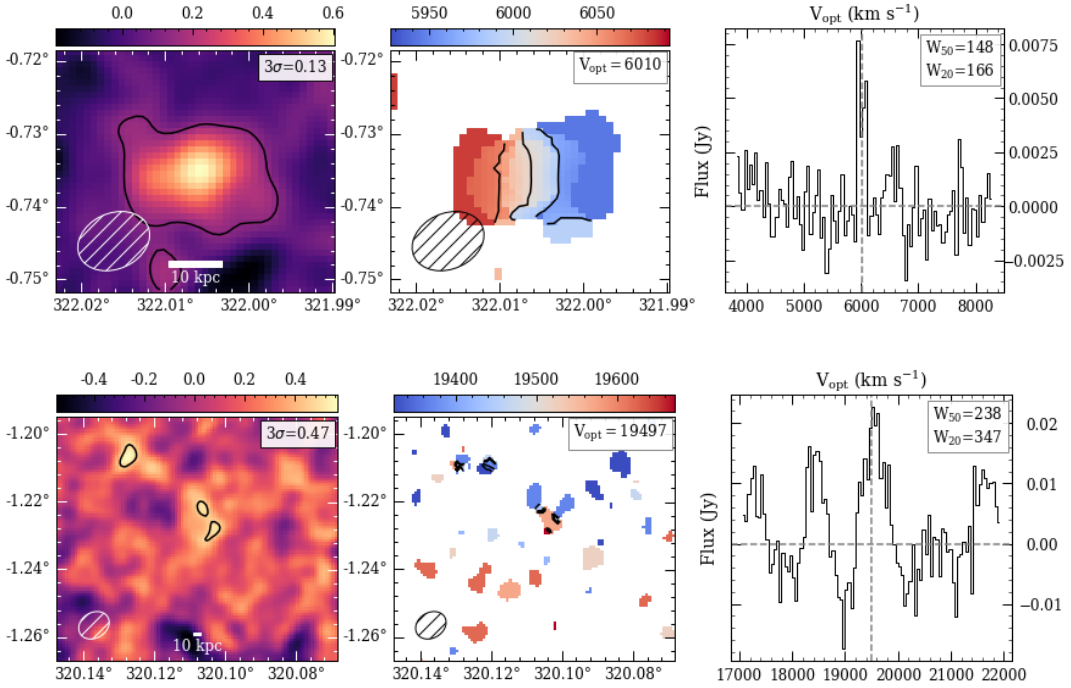

Figure 4.9: Top: A strong SoFiA detection with a moment-0 map (left panel) showing a distinct core, a moment-1 map (middle panel) showcasing clear rotation that span several channels and a global HI profile (right panel) with a pronounced double-horn. Bottom: An example of a SoFiA detection that is clearly false. The moment maps show no discernible object and the global HI profile reveals a baseline wobble that SoFiA most likely mistook for a peak.

with the frequency range of the survey, it is measured as a narrow peak which can be mistaken for an HI detection. All narrow detections ($\lesssim 40\,\mathrm{km\,s^{-1}}$) were cross-checked against the recombination wavelengths given in Lilley & Palmer (1968).

This source finding and source-verification process described above was implemented on the SoFiA catalogs from all ten mosaics. The moment-maps and HI profiles were later inspected a second time by an independent adjudicator and, after some final changes, the catalog was considered final.

After removing all duplicates from the intersections between mosaics, the final GA-GPS catalog has 477 galaxy detections: 406 solid detections (category 1) and 71 'strong possibles', which are reasonably strong detections, but flagged as category 2 to indicate slightly lower confidence (e.g., detections in high noise areas or with low SNR). An atlas of all GA-GPS detections (in the same format as Fig. 4.9) is available on Google Drive, and an extract is available in Appendix B.

4.8 GA-GPS Data Results

In this section, the final catalog of HI-detected galaxies is presented. This is followed by an assessment of the HI parameters through a detailed comparison with HIZOA galaxies in common (N=40) — including flux reproducibility and the HI mass ($M_{\rm HI}$) distribution. In Sect. 4.11, the GA-GPS detections are analysed in relation to large scale structure.

4.8.1 The GA-GPS Galaxy Catalog

Table 4.3 shows the first 50 entries of the final galaxy catalog of the GA-GPS survey. The full GA-GPS galaxy catalog is presented in Table B1, Appendix B. A brief description of the parameters follows. The output parameters produced by SoFiA are presented, unless otherwise stated.

– (1) GPS identifier, reflecting the equatorial coordinates [GPS-HI-Jhhmmss ± ddmmss].
– (2) Mosaic [T10 – T19].
– (3) Galactic longitude [deg].
– (4) Galactic latitude [deg].
– (5) Peak flux density – taken from the HI profile [Jy].
– (6) Integrated flux [Jy km s^{-1}].
– (7) Integrated flux uncertainty [Jy km s^{-1}].
– (8) Local rms – as measured in the corners of the sub-cube [Jy beam^{-1}].
– (9) Heliocentric velocity (optical convention) [km s^{-1}].
– (10) Line width at 20% of the peak flux density, measured in the observer's frame [km s^{-1}].
– (11) Line width at 50% of the peak flux density, measured in the observer's frame [km s^{-1}].
– (12) HI mass ($M_{\rm HI}$) – calculated with eq. 2.4 [$\log(M_{\rm HI}/M_\odot)$]. HI masses have not been corrected to the barycentre of the Local Group ($V_{\rm LG}$), nor corrected for the limited instrumental resolution.
– (13) Flag [category 1 (high confidence) or 2 (slightly lower confidence)].
– (14) Note [other name and/or comment].

Table 4.3: Extract of the GA-GPS galaxy catalog.

name	mosaic	ℓ	b	$S_{\rm peak}$	$S_{\rm int}$	$\mathrm{err}_{S_{\rm int}}$	rms	$V_{\rm hel}$	W_{20}	W_{50}	$M_{\rm HI}$	flag	note
J2000	TXX	deg	deg	Jy	Jy km/s	Jy km/s	Jy km/s	km/s	km/s	km/s	$\log(M_{\rm HI}/M_\odot)$	1/2	
(1)	(2)	(3)	(4)	(5)	(6)	(7)	(8)	(9)	(10)	(11)	(12)	(13)	(14)
J124141-620158	T19	301.788	0.817	0.008	1.25	0.79	0.33	12051	228	212	9.93	1	
J124160-615621	T19	301.821	0.912	0.008	0.46	0.35	0.33	5817	116	82	8.87	1	
J124342-620018	T19	302.024	0.853	0.005	0.42	0.37	0.29	12042	277	277	9.45	1	
J124404-624235	T19	302.088	0.150	0.006	0.94	0.46	0.26	10920	267	225	9.72	1	
J124431-622415	T19	302.130	0.457	0.010	0.78	0.48	0.29	11780	138	82	9.70	1	
J124532-624150	T19	302.255	0.167	0.010	0.84	0.39	0.26	11828	126	97	9.73	1	
J124624-630308	T19	302.362	-0.186	0.093	30.84	2.39	0.35	3912	489	455	10.35	1	J1246-63
J124734-630933	T19	302.494	-0.291	0.012	1.66	0.62	0.28	10105	266	241	9.90	1	
J124738-640005	T19	302.514	-1.133	0.007	0.68	0.46	0.34	10026	183	183	9.50	1	
J124844-621629	T19	302.618	0.595	0.012	1.95	1.27	0.33	11492	276	248	10.08	1	
J125027-620604	T19	302.816	0.770	0.007	0.92	0.90	0.30	15601	365	341	10.01	2	
J125060-614758	T19	302.880	1.072	0.018	1.12	0.72	0.36	15657	114	75	10.10	1	
J125146-622743	T19	302.970	0.410	0.004	0.51	0.40	0.30	11786	353	328	9.52	1	
J125214-632227	T19	303.021	-0.503	0.007	0.95	0.41	0.25	12876	225	210	9.86	1	
J125248-630837	T19	303.085	-0.272	0.006	0.63	0.32	0.24	12537	231	221	9.66	1	
J125255-631242	T19	303.099	-0.340	0.005	0.68	0.41	0.26	12587	323	292	9.70	1	
J125400-625346	T19	303.224	-0.026	0.002	0.11	0.14	0.23	12934	133	108	8.94	1	
J125446-640154	T19	303.296	-1.162	0.007	0.31	0.28	0.30	10116	92	76	9.17	1	
J125500-630545	T19	303.335	-0.227	0.009	0.97	0.45	0.27	10071	183	183	9.66	1	
J125625-631226	T19	303.493	-0.341	0.006	1.05	0.51	0.27	15920	326	302	10.09	1	
J125701-624842	T19	303.568	0.053	0.010	1.60	0.88	0.30	12929	259	225	10.09	1	
J125729-625317	T19	303.621	-0.025	0.004	0.27	0.27	0.27	15910	137	121	9.50	1	
J125841-620529	T19	303.780	0.768	0.011	0.81	0.52	0.32	9844	86	71	9.56	1	
J125907-641822	T19	303.765	-1.447	0.025	3.86	1.60	0.71	3756	215	200	9.41	1	J1259-64
J125932-635841	T19	303.819	-1.120	0.014	1.33	0.54	0.34	3912	135	117	8.99	1	
J125937-624059	T19	303.870	0.174	0.009	0.65	0.53	0.30	10535	128	109	9.52	1	
J130033-625813	T19	303.967	-0.117	0.007	0.47	0.31	0.27	10105	127	112	9.35	1	
J130211-640338	T19	304.107	-1.213	0.021	2.64	1.09	0.36	3917	253	223	9.28	1	J1302-64
J130219-621523	T19	304.197	0.589	0.009	1.19	0.78	0.36	13789	311	133	10.02	1	
J130235-640621	T19	304.148	-1.260	0.017	1.61	0.91	0.37	3923	157	101	9.07	1	J1302-64
J130247-614827	T19	304.272	1.035	0.007	0.95	0.96	0.35	13738	330	280	9.92	1	
J130804-625122	T18	304.827	-0.046	0.007	1.05	0.80	0.44	19820	414	329	10.27	2	
J130804-622610	T18	304.855	0.373	0.006	0.13	0.24	0.43	15894	83	53	9.18	2	
J130833-630248	T18	304.870	-0.239	0.007	1.01	0.71	0.48	12131	231	231	9.84	1	
J130932-640405	T18	304.908	-1.266	0.015	1.17	1.41	0.52	16626	421	161	10.17	2	
J131002-612302	T18	305.157	1.408	0.012	0.56	0.33	0.43	3904	45	45	8.61	1	
J131053-635201	T19	305.071	-1.076	0.005	0.23	0.41	0.37	12271	92	86	9.21	2	
J131127-634643	T18	305.141	-0.993	0.010	1.17	0.89	0.39	7822	270	254	9.53	1	
J131202-634757	T18	305.204	-1.018	0.024	3.41	1.69	0.41	7711	220	170	9.98	1	
J131319-631846	T18	305.386	-0.545	0.005	0.51	0.48	0.44	12136	171	138	9.54	1	
J131435-632335	T18	305.521	-0.638	0.008	1.12	0.90	0.43	12298	442	359	9.89	2	
J131744-633015	T18	305.861	-0.782	0.055	2.33	0.83	0.45	3750	72	45	9.19	1	J1318-63
J131924-635630	T18	305.997	-1.236	0.014	1.22	0.85	0.42	12729	225	188	9.96	1	
J132005-631728	T18	306.145	-0.598	0.006	0.43	0.44	0.32	24852	231	145	10.07	2	
J132011-631618	T18	306.157	-0.580	0.036	6.03	1.86	0.46	3743	236	151	9.60	1	J1320-63
J132158-621724	T18	306.473	0.372	0.010	0.34	0.30	0.34	9690	46	29	9.18	1	
J132322-620858	T18	306.651	0.491	0.006	0.17	0.22	0.32	2392	36	22	7.68	2	possible dwarf
J132407-623712	T18	306.679	0.014	0.010	3.05	1.75	0.38	6609	492	456	9.80	1	
J132532-621306	T18	306.894	0.391	0.008	1.16	0.79	0.35	6567	453	450	9.37	1	
J132642-613202	T18	307.121	1.051	0.029	7.29	1.57	0.35	6503	307	287	10.16	1	J1327-61

4.9 Comparison between HIZOA and GA-GPS Detections

Table 4.4 shows all the HIZOA galaxies that have a counterpart in GA-GPS, excluding the galaxies that were resolved into multiple sources. The detections listed here are used for the flux comparison in Fig. 4.15, Sect. 4.10. Columns 1 – 8 correspond to HIZOA and columns 9 – 16 correspond to GPS. A brief description of the parameters are as follows:
– (1) Unique identifier [J2000].
– (2) Galactic longitude [deg].
– (3) Galactic latitude [deg].
– (4) Integrated flux [$\mathrm{Jy\,km\,s^{-1}}$].
– (5) Integrated flux uncertainty [$\mathrm{Jy\,km\,s^{-1}}$].
– (6) Heliocentric velocity (optical convention) [$\mathrm{km\,s^{-1}}$].
– (7) Line width at 50% of the peak flux density, measured in the observer's frame [$\mathrm{km\,s^{-1}}$].
– (8) HI mass (M_{HI}) [$\log(M_{\mathrm{HI}}/M_{\odot})$]. HI masses have not been corrected to the barycentre of the Local Group (V_{LG}), nor corrected for the limited instrumental resolution.
This sequence is repeated for columns 9 – 16.

Table 4.4: Comparison of HIZOA and GA-GPS parameters, for all one-to-one counterparts.

HIZOA name (J2000)	ℓ deg	b deg	$S_{\rm int}$ Jy km/s	uncertainty Jy km/s	$V_{\rm hel}$ km/s	W_{50} km/s	$M_{\rm HI}$ $\log(M_{\rm HI}/M_\odot)$	GPS name (J2000)	ℓ deg	b deg	$S_{\rm int}$ Jy km/s	uncertainty Jy km/s	$V_{\rm hel}$ km/s	W_{50} km/s	$M_{\rm HI}$ $\log(M_{\rm HI}/M_\odot)$
J1246-63	302.36	-0.20	29.82	2.25	3916	459	10.2	J124624-630308	302.36	-0.19	30.84	2.39	3912	455	10.35
J1259-64	303.81	-1.45	3.94	0.87	3751	186	9.3	J125907-641822	303.77	-1.45	3.86	1.60	3756	200	9.41
J1318-63	306.01	-0.70	1.57	0.61	3747	25	8.9	J131744-633015	305.86	-0.78	2.33	0.83	3750	45	9.19
J1320-63	306.18	-0.61	7.20	1.20	3769	147	9.6	J132011-631618	306.16	-0.58	6.03	1.86	3743	151	9.60
J1327-61	307.19	0.98	8.70	1.70	6487	266	10.1	J132642-613202	307.12	1.05	7.29	1.57	6503	287	10.16
J1329-61	307.46	0.69	12.24	1.74	3699	203	9.8	J133002-615146	307.47	0.67	15.62	2.25	3696	222	10.01
J1331-62	307.63	0.45	2.18	0.95	7130	53	9.6	J133202-620407	307.67	0.43	1.57	0.62	7152	55	9.58
J1342-61	309.07	1.23	23.53	2.29	3946	326	10.1	J134227-610114	309.07	1.24	23.92	6.85	3964	326	10.25
J1348-61	309.61	0.23	2.23	0.79	4084	32	9.1	J134849-615619	309.63	0.19	3.61	1.55	4073	65	9.45
J1404-63	311.09	-1.50	7.87	1.12	7972	273	10.3	J140445-631057	311.09	-1.48	4.60	2.25	7951	273	10.13
J1414-62B*	312.47	-0.94	3.37	0.68	3288	190	9.1	J141521-621113	312.55	-0.89	4.33	1.12	3285	174	9.35
J1421-60	313.81	0.60	3.81	1.17	3883	246	9.3	J142120-602328	313.82	0.57	5.57	1.07	3891	269	9.60
J1423-59	314.22	0.97	10.32	1.79	5650	515	10.1	J142320-595138	314.24	0.98	11.99	1.78	5650	529	10.26
J1424-60	314.33	0.66	4.37	1.09	4124	187	9.4	J142510-600550	314.37	0.68	4.95	0.87	4142	198	9.61
J1425-59	314.51	1.05	4.79	0.86	8323	255	10.1	J142448-594049	314.47	1.08	3.06	0.85	8326	273	10.00
J1426-60	314.46	0.48	2.56	1.37	3692	231	9.1	J142621-601356	314.46	0.50	6.82	0.97	3711	213	9.65
J1435-61	315.09	-0.82	3.90	1.21	9836	174	10.2	J143505-611315	315.08	-0.82	4.68	0.91	9839	164	10.32
J1437-60	315.71	-0.25	13.98	1.57	4452	271	10.0	J143759-602534	315.72	-0.23	17.87	2.40	4471	305	10.23
J1504-57	320.19	1.07	4.04	0.96	3189	134	9.2	J150444-571309	320.24	1.11	4.48	0.96	3173	134	9.33
J1504-60	318.84	-1.40	6.02	1.46	4733	102	9.7	J150441-600535	318.83	-1.40	4.66	1.51	4719	85	9.69
J1513-56	321.49	0.81	7.51	0.96	4963	227	9.9	J151356-564906	321.52	0.82	6.01	1.22	4956	219	9.84
J1518-55	322.67	1.48	13.58	1.33	1484	234	9.0	J151830-553858	322.68	1.48	12.03	2.74	1510	237	9.12
J1530-55	324.08	0.49	16.58	1.83	5003	230	10.2	J153037-554053	324.09	0.51	14.65	2.20	5000	240	10.24
J1530-58	322.71	-1.52	4.92	1.13	5001	94	9.7	J153045-580625	322.72	-1.49	3.03	1.51	4983	90	9.55
J1531-55	324.22	0.43	7.61	1.39	1440	62	8.7	J153149-553838	324.25	0.45	4.08	0.91	1466	85	8.62
J1534-56B	324.25	-0.24	4.94	1.42	2904	115	9.2	J153429-560942	324.25	-0.19	4.45	0.88	2884	136	9.25
J1535-54	325.39	1.19	7.45	1.31	5700	245	10.0	J153516-542147	325.39	1.21	5.39	1.68	5696	240	9.92
J1536-56	324.32	-0.58	16.21	1.90	2723	165	9.6	J153630-562544	324.32	-0.57	18.00	2.03	2706	179	9.80
J1542-55	325.65	-0.24	8.86	1.76	5404	258	10.0	J154306-551947	325.72	-0.24	2.14	0.62	5411	77	9.47
J1545-56	325.38	-1.17	5.56	1.50	5499	158	9.8	J154515-561616	325.39	-1.17	2.90	1.50	5479	162	9.61
J1603-53	329.27	-0.56	6.68	1.15	5781	109	9.9	J160307-531754	329.27	-0.52	3.56	1.00	5790	103	9.75
J1605-51	330.93	0.77	10.63	2.85	5758	305	10.1	J160547-511331	330.95	0.76	4.48	2.18	5716	334	9.84
J1607-51	331.29	0.70	8.65	1.51	6041	178	10.1	J160748-510447	331.28	0.65	8.71	2.09	6036	181	10.17
J1607-53	329.43	-1.32	7.75	1.21	5515	320	10.0	J160732-534914	329.41	-1.35	6.95	3.43	5483	265	9.99
J1609-50	332.08	1.08	5.18	2.01	6202	123	9.9	J161008-501124	332.15	1.06	5.68	2.64	6245	184	10.02
J1612-52	330.72	-1.09	2.45	0.90	5671	88	9.5	J161246-524516	330.71	-1.10	2.80	1.26	5678	114	9.63

4.9.1 Special HIZOA Cases

Four HIZOA sources were found to be composed of multiple counterparts in the deep interferometric data. Three HIZOA sources are split into two sources and one HIZOA source is split into three sources. These special cases are shown in Figs. 4.10 – 4.13, where the yellow histogram is the HI profile from the published HIZOA data[8]. The GA-GPS counterparts are shown separately (left panels) and summed together (right panels). The bottom panels are moment-0 maps of the respective regions. It is not surprising that some sources were resolved into separate counterparts given both the higher spatial resolution (beamsize $\sim 31'' \times 26''$ vs 15') and the better rms sensitivity (average 0.47 mJy beam^{-1} vs 6 mJy beam^{-1}).

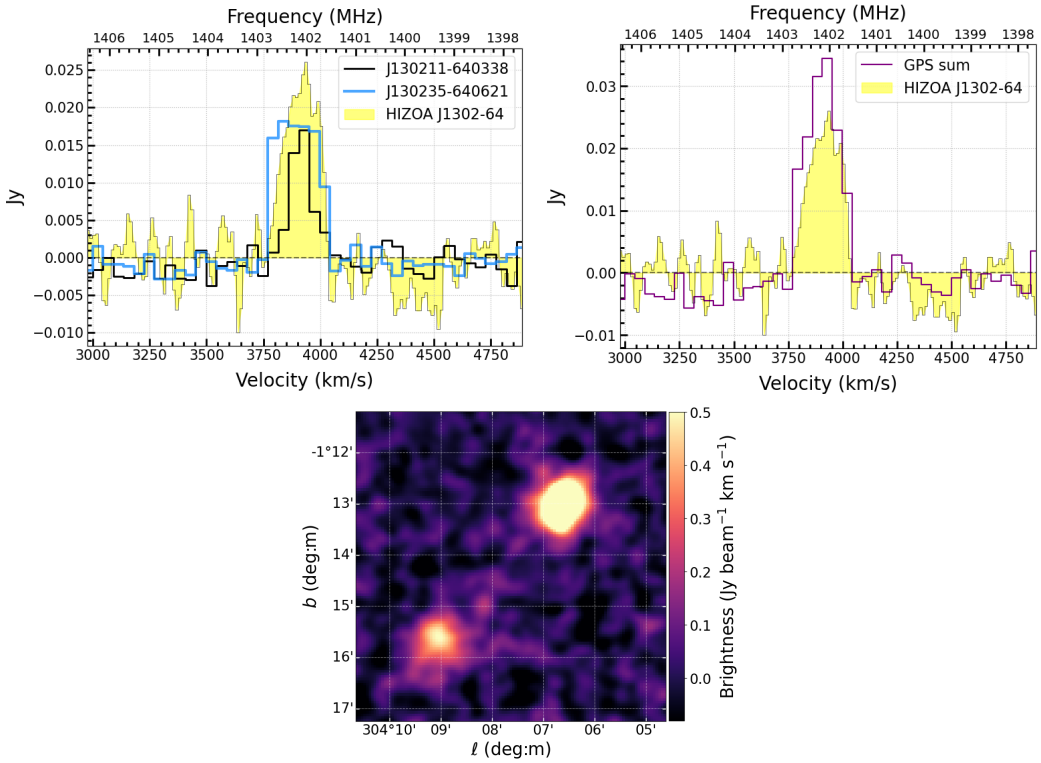

Figure 4.10: HIZOA J1302-64 is resolved into two counterparts in GPS.

[8]Data is publicly available at https://www.atnf.csiro.au/research/multibeam/release/

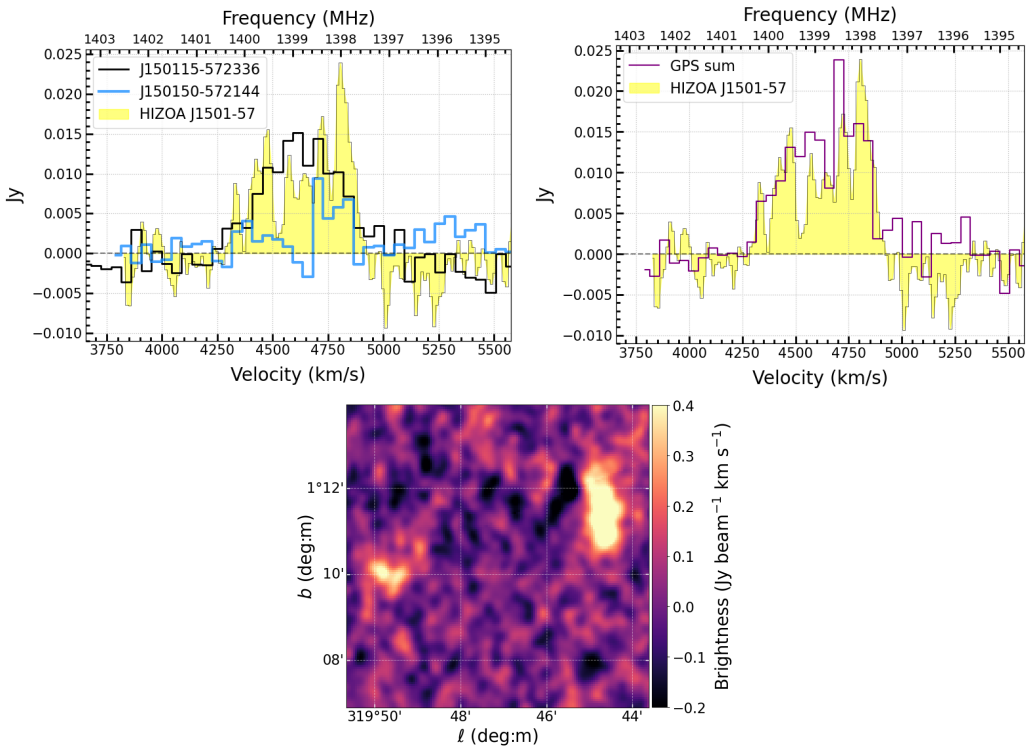

Figure 4.11: HIZOA J1501-57 is resolved into two counterparts in GPS.

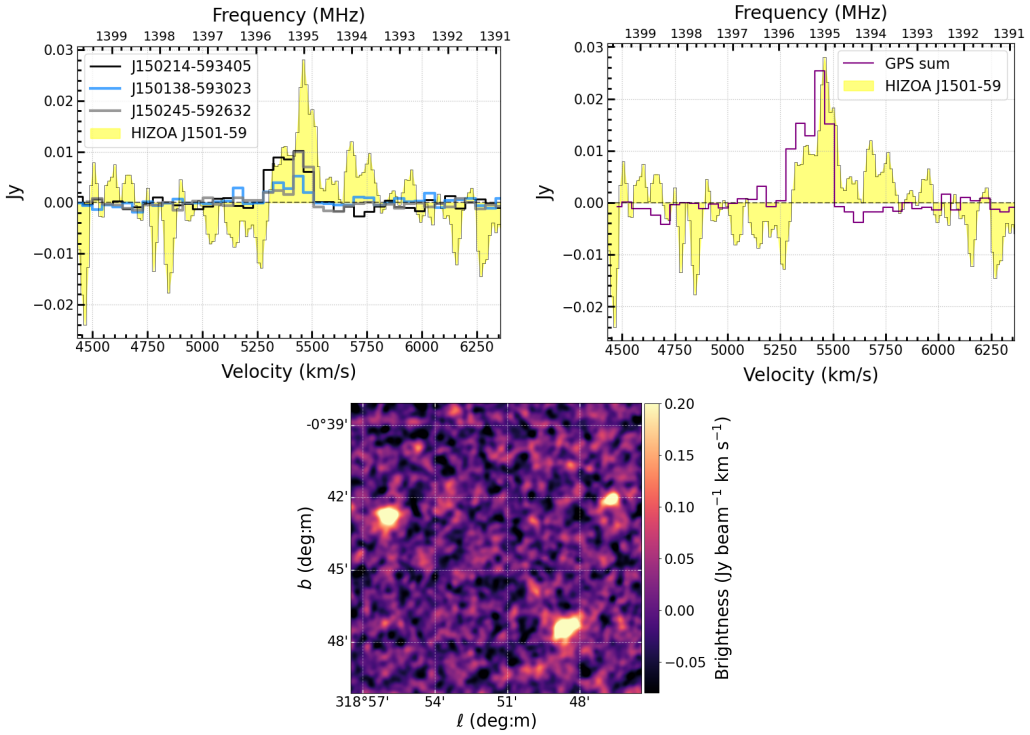

Figure 4.12: HIZOA J1501-59 is resolved into three counterparts in GPS.

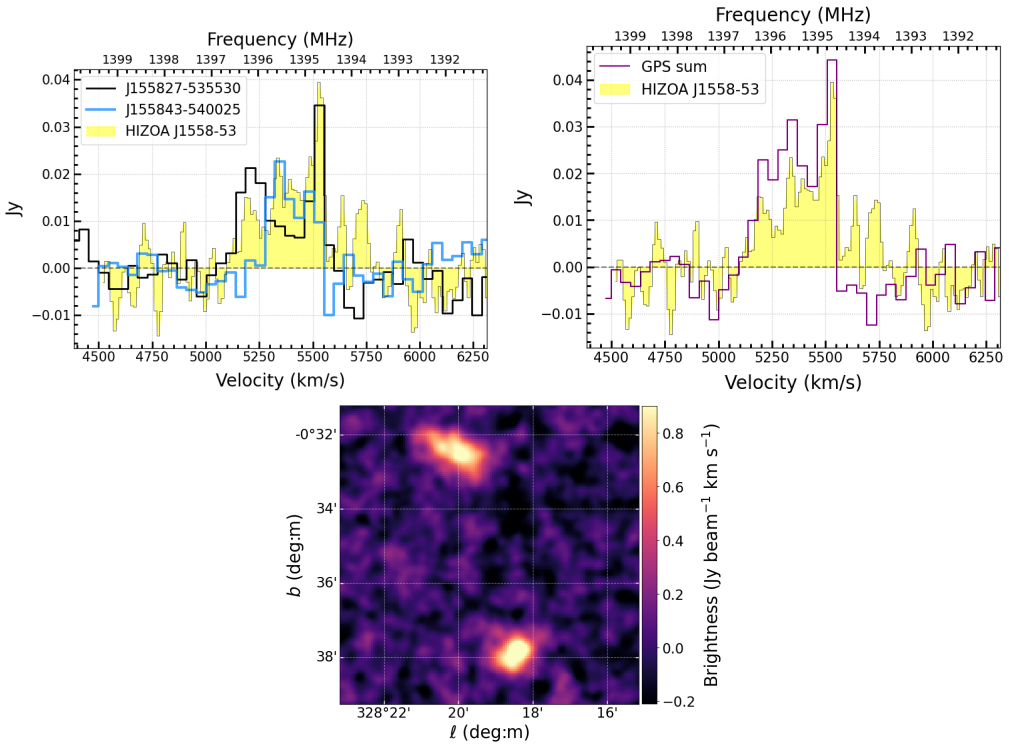

Figure 4.13: HIZOA J1558-53 is resolved into two counterparts in GPS.

The GPS HI profiles reproduce the HIZOA flux and profile shape better when the flux of the relevant GPS counterparts are summed together (right panels), compared to any of the separate individual profiles (left panels). This is a good indication that we have grouped these counterparts correctly. All HI profile plots comparing HIZOA and GA-GPS are shown in Fig. B1, Appendix B.

Forty-two (42) HIZOA galaxies (out of 883 total) fall within the GA-GPS data strip. Only two of these galaxies were not recovered by SoFiA in GPS data. One is a very special case due to its remarkable extent and very low column density (an average of $\mathbf{10}^{19}$ $N_{\rm HI}$, peaking at $\mathbf{10}^{20}$ $N_{\rm HI}$), therefore it is currently being investigated in more detail through deeper MeerKAT64 follow-up observations with the 32K correlator. A sneak-peak of this giant, almost face-on, open-armed spiral galaxy is shown in Fig. 4.14. The second missing source can not be identified by eye at the expected coordinates, leading to a hypothesis that it could form part of the very extended object.

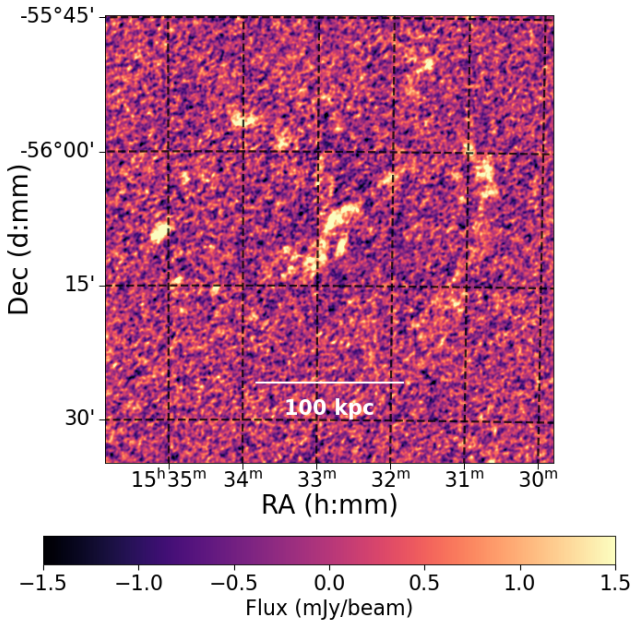

Figure 4.14: A channel map of a very special case: a HIZOA galaxy that has now been revealed to be much more extended than originally estimated.

4.10 Comparison of HI Parameters

4.10.1 Flux Determination

Flux verification is a fundamental step in assessing the data quality of HI images. At Galactic latitudes $b < \pm 2°$, the only sources available for flux verification are HIZOA galaxies (Staveley-Smith et al., 2016) and two galaxies previously discovered by GLIMPSE. If GPS independently reproduces integrated flux values consistent with HIZOA, it will be a strong indication that the flux in the data is captured accurately. Bear in mind, the reliability of the continuum flux was confirmed early on in the data reduction process by our collaborators.

Cases where HIZOA galaxies had more than one counterpart in GPS (as previously discussed and shown in Figs. 4.10 – 4.13) are excluded from the flux comparison sample. The remaining integrated HI flux values ($S_{\rm int}$) are plotted in Fig. 4.15 as a function of their flux values in HIZOA. The $S_{\rm int}$ values are taken directly from the SoFiA catalog, where they have already been corrected for the beam solid angle (by setting PARAMETER.PHYSICAL = True). The (statistical) uncertainty was calculated as $\mathrm{rms} \times 44.1\,\mathrm{km\,s^{-1}} \times \sqrt{\mathrm{N_{pix}}}$, where

rms is the local rms measured at the position of the source, 44.1 km s^{-1} is the channel width (at $z = 0$) and N_{pix} is the number of pixels that make up the source.

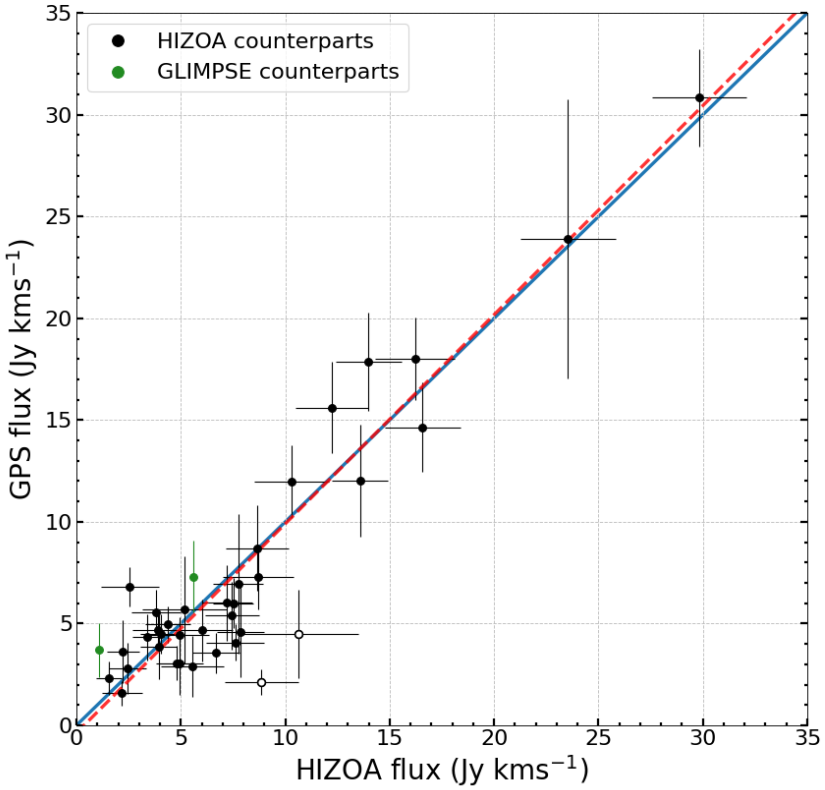

Figure 4.15: A comparison between the integrated fluxes (S_{int}) of HIZOA detections (x-coordinate) and the GPS counterparts (y-coordinate). The x (statistical) uncertainty is the published HIZOA uncertainty and the y (statistical) uncertainty is the GPS measurement uncertainty (explained in text). The two green markers represent GLIMPSE counterparts. The blue solid line represents a one-to-one relation and the red dashed line is a linear fit.

The points in green are not HIZOA galaxies, but represent counterparts based on ATCA observations of two GLIMPSE galaxies, discussed in detail in Jarrett et al. (2007).

In Fig. 4.15, the dispersion is greatest at the low-flux end; not surprising since smaller galaxies are more difficult to measure above the background noise, especially if the channels are broad — as is the case for GPS.

HIZOA J1542-55 and J1605-51, the two furthest outliers, are given an empty marker. Their HI profiles from the HIZOA survey are shown in Fig. 4.16 (also see HI profile comparison plots in Appendix B). When considering these plots, the baselines in the

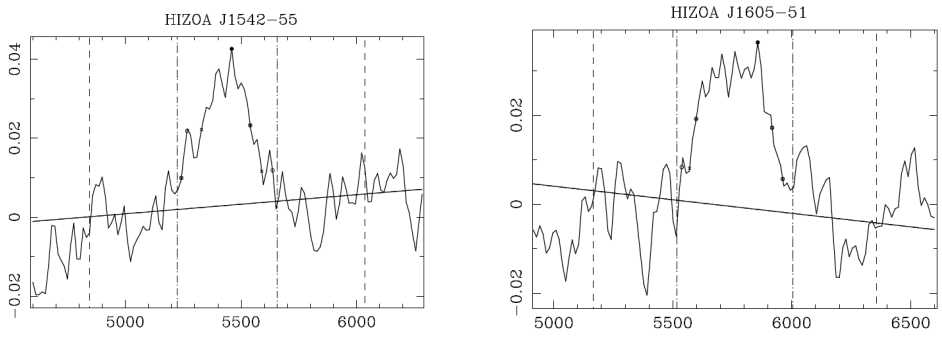

Figure 4.16: Published HI profiles of HIZOA galaxies J1542-55 and J1605-51; velocity on the x-axis and $S_{\rm int}$ (Jy) on the y-axis. These sources appear as outliers in Fig. 4.15, where they are marked with open circles.

HIZOA data are found to be irregular, making it difficult to define the profiles. In turn, there is uncertainty with regards to HIZOA's baseline subtraction (the linear baseline fits in Fig. 4.16) because it is not exactly clear where the baseline ends and where the signal begins. These two points were therefore excluded from the linear fit (red dashed line).

The red dashed line is the result of fitting the data points (excluding the two outliers) with a linear regression least-squares fit algorithm (using `scipy.optimize.curve_fit`). The high R^2 value of 0.92 indicates this model fits the data well. This routine returns a near-perfect slope of 1.03 ± 0.06, hence a near-perfect one-to-one relation over the flux range in common wit HIZOA.

There is also consistency with the independent ATCA data from the two GLIMPSE sources (green dots), including agreement in line width. G1 has a W_{50} of $365\,{\rm km\,s^{-1}}$ and $375.6\,{\rm km\,s^{-1}}$ in GLIMPSE and GPS, respectively, and G2 has a W_{50} of $397\,{\rm km\,s^{-1}}$ and $377.4\,{\rm km\,s^{-1}}$ in GLIMPSE and GPS, respectively.

This flux assessment demonstrates good agreement between GA-GPS and literature, providing evidence that our calibration is accurate.

A further quality check is to investigate the three-dimensional positional offsets between the GPS and HIZOA counterparts. Examining the magnitude and directions of the offsets have the potential to indicate biases in our data.

4.10.2 Offsets in Redshift Space and Line Width

Figures 4.17 show the positional offsets (left panel), $V_{\rm hel}$ (GPS) versus $\Delta V_{\rm hel}$ (right panel; where $\Delta V_{\rm hel} = V_{\rm HIZOA} - V_{\rm GPS}$) and the offsets in W_{50} (bottom panel). The positional offsets have a mean angular separation of 2.6 ±2.0' and most of the offsets fall within the pixel

scale of HIZOA (4'). There is one notable outlier (in the top right quadrant) which has been identified as the source J1318-63. Despite the on-sky offset for this source being larger than expected, we do believe this is the correct GPS counterpart (J131744-63301) because the velocities and line widths are a close match: $V_{\rm opt} = 3747\,{\rm km\,s^{-1}}$ versus $3750\,{\rm km\,s^{-1}}$ and $W_{50} = 25 \pm 15\,{\rm km\,s^{-1}}$ versus $44\,{\rm km\,s^{-1}}$ in HIZOA and GPS respectively. Another point to consider is J1318-63 is a very small galaxy with $S_{\rm int} = 1.57 \pm 0.61\,{\rm mJy}$, as measured in HIZOA. This is below HIZOA's completeness limit of 3.1 mJy (Staveley-Smith et al., 2016) and therefore the parameters are measured with lower confidence in that survey.

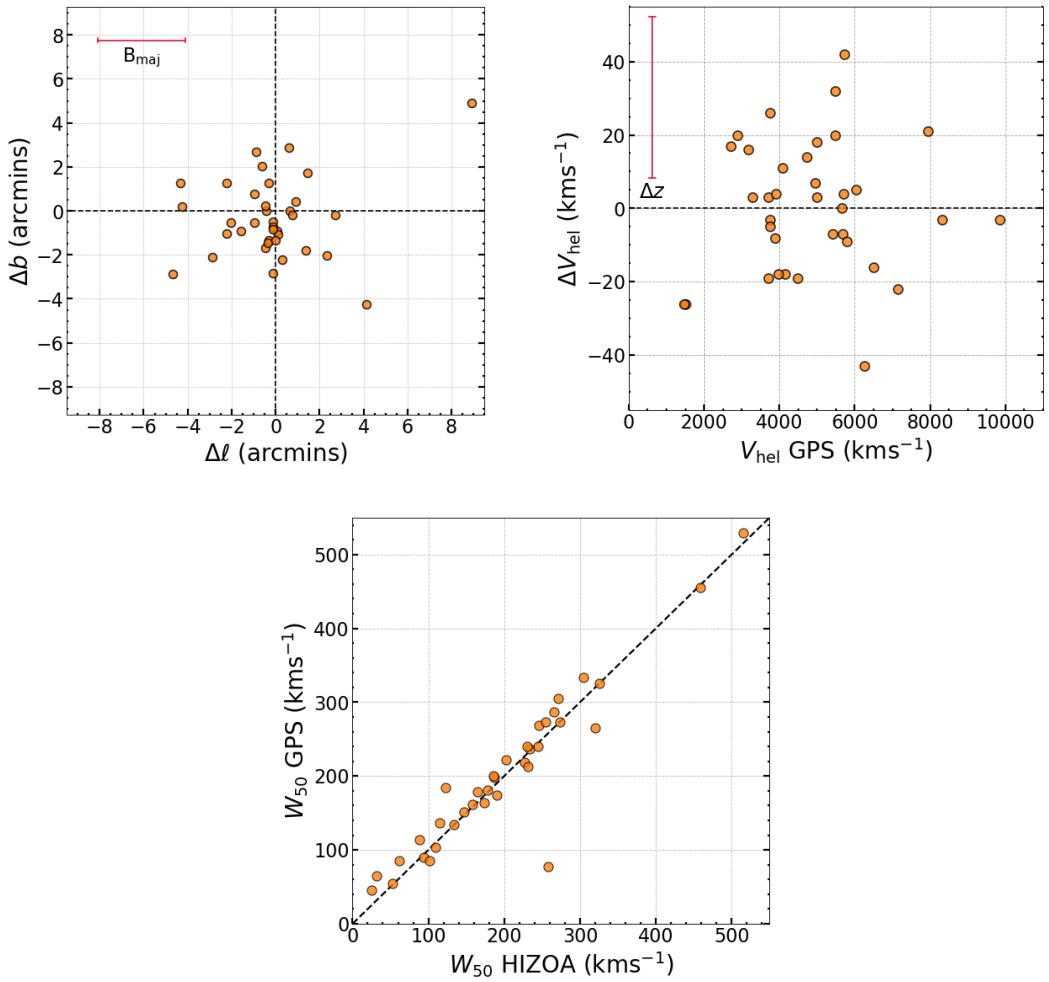

Figure 4.17: Offsets in parameters of the published HIZOA galaxies compared to the GA-GPS counterparts. Top left: on-sky offsets (with a scale-bar showing the HIZOA beam size); top right: $V_{\rm hel}$ (GPS) versus $\Delta V_{\rm hel}$, where $\Delta V_{\rm hel} = V_{\rm HIZOA} - V_{\rm GPS}$; and bottom; W_{50} offsets. Note that the GPS HI masses have not been corrected to the Local Group rest frame ($V_{\rm LG}$), whereas the HIZOA HI masses have.

The mean velocity offset is $14 \pm 11\,\mathrm{km\,s^{-1}}$. This is much less than one spectral channel in GPS ($\sim$44.1 $\mathrm{km\,s^{-1}}$). In addition, the points in the left and right panels seem to have a random distribution around 0. This implies that we do not observe any trends. The W_{50} comparisons (bottom panel) show good consistency, and the points are divided roughly evenly by the y=x line (black dashed line). The biggest outlier, appearing well below the y=x line is the previously mentioned HIZOA source J1542-55 (left panel in Fig. 4.16). As the HIZOA profile shows, the baseline was wavy, making it difficult to define the width of the signal. The GPS baseline was more stable in this case (see profile comparison in Fig. B1, Appendix B) therefore the (narrower) GPS W_{50} parameter is likely to be more accurate.

Figures 4.15 & 4.17 do not show any systematic biases in either flux, on-sky position, velocity or line width when compared to HIZOA results. The good agreement between HIZOA and GPS — where the latter were measured independently with a different instrument (single-dish versus interferometer) — is an indication that our HI images are of good quality. This result is also vindication of the HIZOA survey itself.

4.10.3 HI Masses

Figure 4.18 shows the M_{HI} of the full GA-GPS catalog as a function of redshift (indicated by the black dots). The theoretical sensitivity curves (produced with equation 2.7) represent detections of 5σ with line widths of $100\,\mathrm{km\,s^{-1}}$ (solid line) and $250\,\mathrm{km\,s^{-1}}$ (dashed line) at an rms of $0.45\,\mathrm{mJy\,beam^{-1}}$. The full catalog of simulated results (discussed in Sect. 4.1) is shown in orange in the background. This plot shows that the M_{HI} distribution of the actual GA-GPS detections substantiates the predictions.

Galaxies were detected within the range of $\log M_{\mathrm{HI}}/M_{\odot} = 7.5 - 10.6$ and the M_{HI} sensitivity curves show that GPS detected galaxies down to the theoretical M_{HI}-limit (M'_{HI}, cf. eq. 2.7) all the way to the far-redshift end of the survey. This confirms the potential of this work to map large scale structure in fine detail.

It is evident that several galaxies were detected below the $5\sigma/W_{100}$ limit. Nearly all of these sources were determined to have $W_{50} < 100\mathrm{km\,s^{-1}}$.

Looking at the histograms in Fig. 4.18, the M_{HI} distribution (right panel) is as expected; spread fairly symmetrically, with the larger galaxies appearing well above the sensitivity limit. However, looking at the velocity distribution, there is a conspicuous clumping in the region $4000 - 6000\,\mathrm{km\,s^{-1}}$. This dense region forms a striking peak in the velocity distribution (top panel), where other smaller peaks are also revealed. This uncovered galaxy distribution can be put into context with known large scale structures.

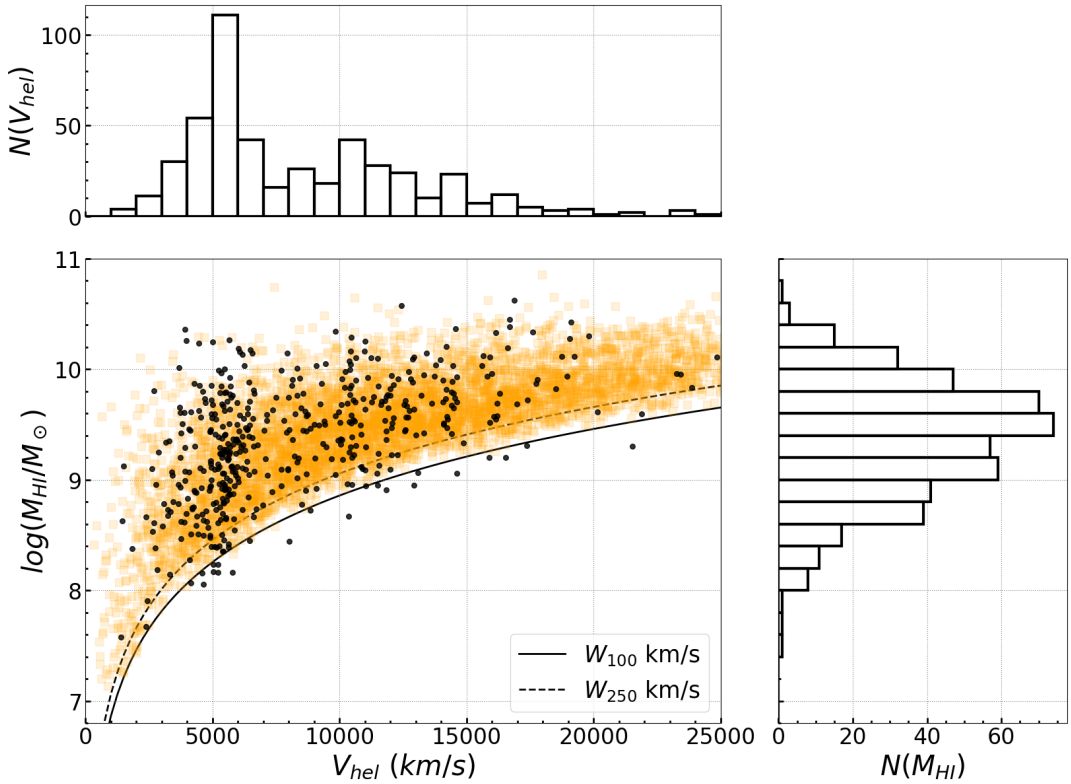

Figure 4.18: Bottom left: The black dots show the measured HI masses ($M_{\rm HI}$) of all GA-GPS detections as a function of recessional velocity ($V_{\rm hel}$). The theoretical sensitivity is plotted for line widths of 100 and 250 $\rm km\,s^{-1}$ at a 5σ threshold and a mean rms of 0.45 $\rm mJy\,beam^{-1}$ (cf. eq. 2.7). The simulation for the full survey (cf. Sect. 4.1) is shown in orange in the background. The top panel is the velocity distribution and the right panel is the $M_{\rm HI}$ distribution.

4.11 Large Scale Structure

Several superclusters above and below the Galactic plane have been mapped in the last few decades. East of the Galactic bulge, below the Galactic plane, lies the Pavo supercluster ($\ell \approx 332°, b \approx$ -24°, $cz \approx 4500\,\rm km\,s^{-1}$; Juraszek et al., 2000). Above the Galactic plane reside the Centaurus supercluster ($\ell \approx 302°, b \approx 22°, cz \approx 3418\rm km\,s^{-1}$; Juraszek et al., 2000) as well as the Ophiuchus cluster ($\ell \approx 0.5°, b \approx 9.5°, cz \approx 8500\,\rm km\,s^{-1}$; Wakamatsu et al., 2005). Crossing the Galactic plane at lower longitudes is the Puppis region ($\ell \approx 245°, |b| \lesssim 8°, cz \approx 1500\,\rm km\,s^{-1}$; Kraan-Korteweg & Huchtmeier, 1992) and the still relatively uncharted Vela supercluster ($\ell \approx 272.5° \pm 20°$, $cz \approx 18\,000\,\rm km\,s^{-1}$, Kraan-Korteweg et al., 2017).

Figure 4.19 shows the redshift distribution (top panel) of the GA-GPS galaxy candidates with a corresponding wedge diagram (bottom panel) that displays the on-sky distribution (in longitude) as a function of velocity ($V_{\rm hel}$). The HIZOA distribution is overlaid in black.

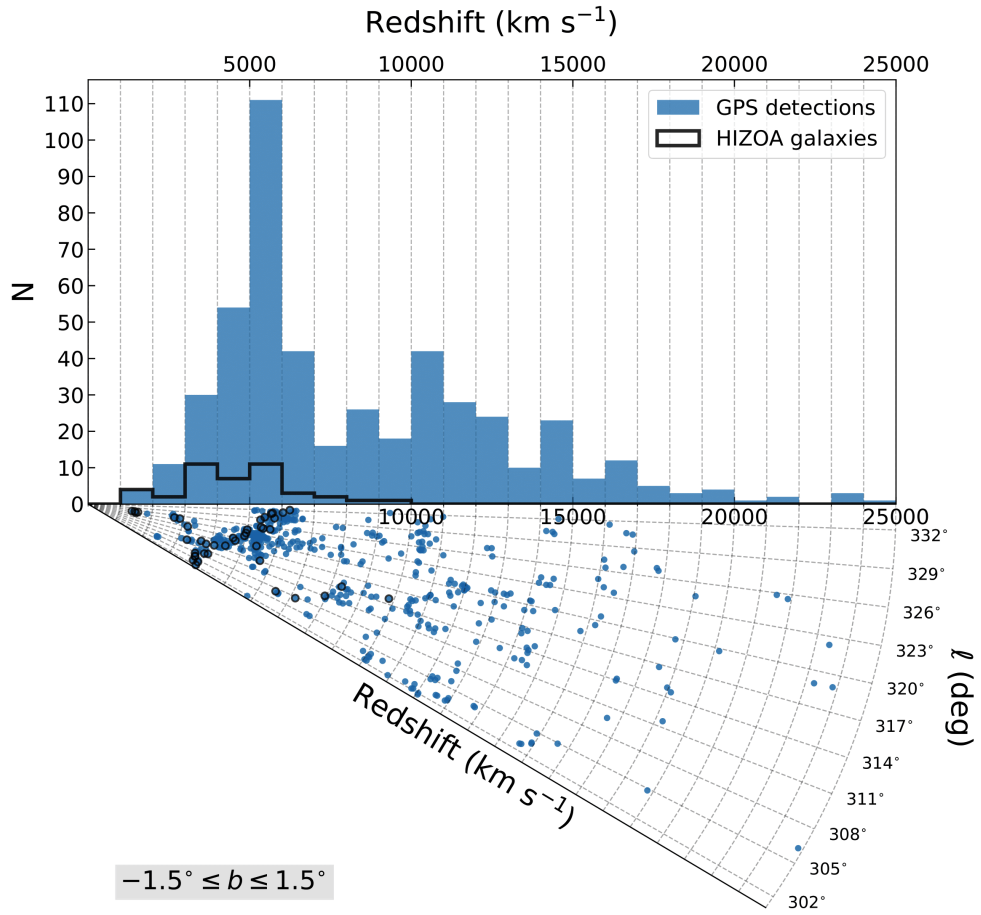

Figure 4.19: Top: the velocity (redshift) distribution of all GA-GPS galaxy detections. Bottom: corresponding wedge diagram showing the distribution of the velocities as a function of Galactic longitude. Blue dots are the GA-GPS galaxies and black circles are the previously known HIZOA galaxies. (Note, a 2°-padding was added to the top of the wedge for legibility.)

The overdensity at $4000-6000\,{\rm km\,s^{-1}}$, a segment of the GA Wall, dominates the velocity distribution with its broad shoulders — which is typical of superclusters (Kraan-Korteweg et al., 2016) — stretching from $\sim$3000 – 7000 km s^{-1}. In the wedge section below,

the HIZOA galaxies (black circles) are in excellent agreement with the densest regions of GA-GPS detections (blue dots).

Filamentary structures form a bump around ~10 000 – 13 000 km s^{-1} . Further out than this, there is rise in detections starting at 14 000 km s^{-1} , which may well be associated with the Ara cluster, located at (ℓ, b, V) = (324.5°, -11.6°, 15 060 km s^{-1}), and the Triangulum-Australis cluster at (ℓ, b, V) = (324°, -12°, 15 300 km s^{-1}) (Woudt et al., 1999); giving support to the hypothesis that these two clusters are associated with structures seen at the same redshift above the ZoA, linking further to the Shapley supercluster (private communication: R. Kraan-Korteweg).

At higher redshifts, the density of detections starts to taper off. GPS identified galaxy candidates out to 25 000 km s^{-1} (99 detections further out than the furthest detection in the full HIZOA survey — $V_{\rm hel}$ ≈12 000 km s^{-1}). Although, the sample is too sparse to identify new structures at the high-redshift end with confidence.

In order to focus on the GA area in more detail, Fig. 4.20 displays the galaxies with redshifts <10 000 km s^{-1} only. The black squares represent galaxies catalogued in the HIZOA survey. In the left panel, the wall-like structure that makes up the GA is traced clearly across the Galactic plane, starting from just under $V_{\rm hel}$ ≈ 4000 km s^{-1} at the lower longitude side, up to $V_{\rm hel}$ ≈ 6000 km s^{-1} at the higher longitude end of the survey. The void centred on (ℓ, b) ~ (316°, 7000 km s^{-1}) is the Circinus Void (Fairall, 1998). No HIZOA galaxies appear in the top left segment of the wedge ($\gtrsim$6500 km s^{-1} and >315°).

The right panel shows the latitude axis (the view if the left cone is turned onto its side), where the same sample appears as a strong but clumpy overdensity.

The HIZOA survey uncovered an overdensity of galaxies stretching between 2500 and 4000 km s^{-1} , suggestive of a continuous bridge of galaxies between the Centaurus and Pavo superclusters behind the Galactic plane (Juraszek et al., 2000). This is corroborated by the findings of the GA-GPS survey, with higher statistical significance. Furthermore, the results of this survey seem to suggest a trend towards the Ophiuchus cluster (Wakamatsu et al., 2005) behind the Galactic bulge, a hint of which is seen in the GPS survey of the Local Void region (Kurapati et al., in prep).

To assist in visualising the continuation of large scale structure, Fig. 4.21 shows wedge diagrams of galaxies below and above the Galactic plane (left and right figures respectively), using redshift data in literature (obtained from HyperLeda[9]). The GA-GPS detections are

[9]The HyperLeda database is available at: http://leda.univ-lyon1.fr/

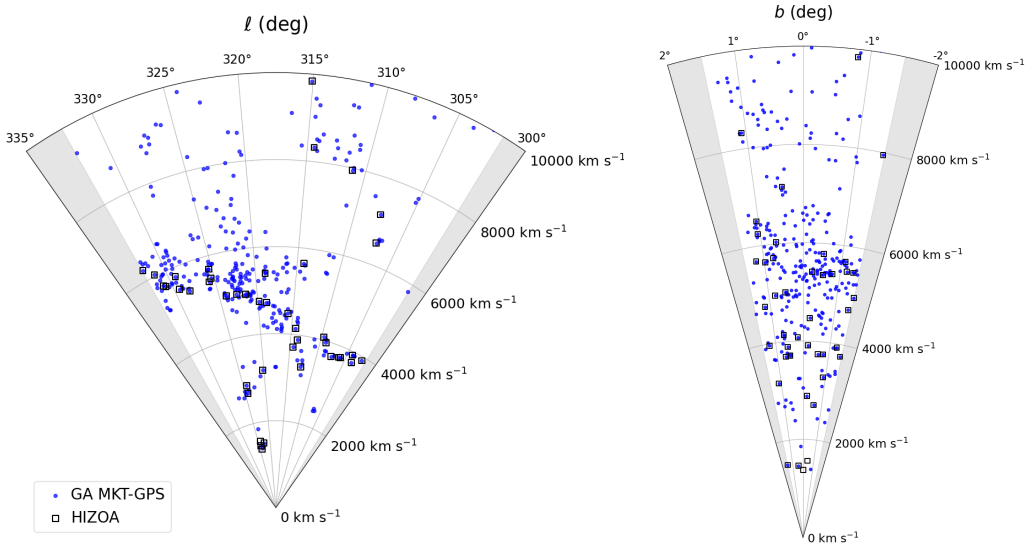

Figure 4.20: Wedge diagrams of GA-GPS galaxy detections (blue dots) and the HIZOA galaxies (black squares) for $V_{\rm hel} \leq 10\,000\,{\rm km\,s^{-1}}$. Left: redshift distribution as a function of longitude. Right: redshift distribution as a function of latitude.

shown as blue dots. The cone portrays a very different galaxy distribution when viewed from above the plane compared to below the plane.

The Norma cluster (ACO3627) at (ℓ, b, $V_{\rm hel}$) = (325.3°, -7.2°, $4871\,{\rm km\,s^{-1}}$), a rich cluster at the core of the GA (Kraan-Korteweg et al., 1996; Woudt et al., 2008), dominates the left wedge. The cluster shows characteristic lengthening along the velocity axis which is due to the combined motions of the galaxies within the potential well of the cluster. This is the well-known "finger of god" effect. The wide block of points between 4000 – $6000\,{\rm km\,s^{-1}}$ beginning at $\sim 315^\circ$ and moving over to the left of the wedge is the crossing of the GA wall. The thinner trail of dots running along $\sim$2600 $\,{\rm km\,s^{-1}}$ is the Centaurus Wall (Radburn-Smith et al., 2006).

The wedge on the right offers a view of the heavily obscured PKS1343-601 cluster at (ℓ, b, $V_{\rm hel}$) = (309.7°, 1.7°, $3872\,{\rm km\,s^{-1}}$; Kraan-Korteweg & Woudt, 1999; Kraan-Korteweg et al., 2003; Nagayama et al., 2004), where a dense group appears to take shape. Judging from this figure, as well as Fig. 4.20, the GA-GPS detections seem to provide a link to lower latitudes, which gives support for this suspected cluster.

The wedge plots (among others in this Chapter) show that, along with areas of overdensities, there are areas void of galaxies. The most significant void to the GPS survey, the Local Void, is a region to the left of the Galactic bulge that reaches as far as $\ell \sim 60^\circ$,

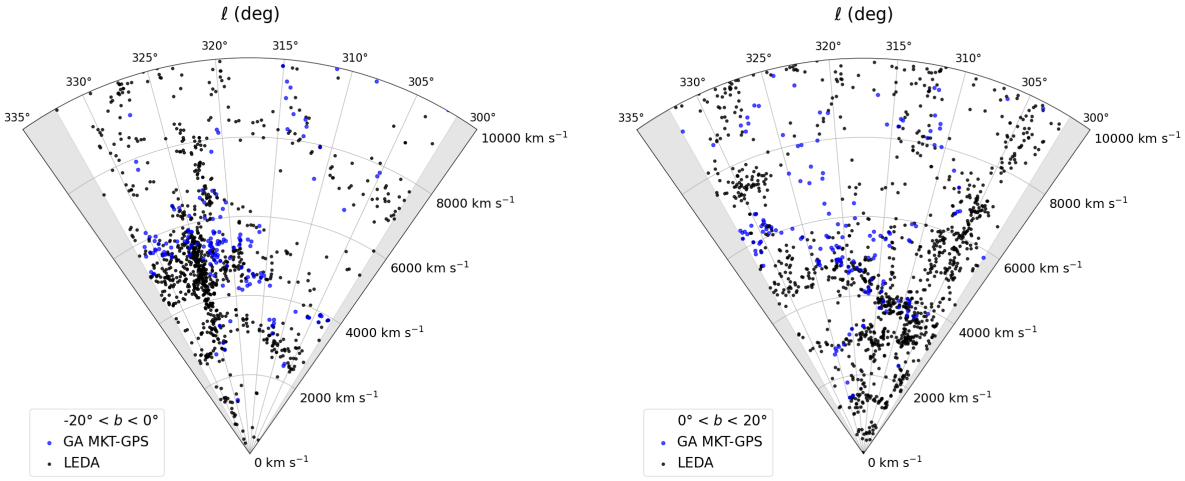

Figure 4.21: Wedge diagrams showing Galactic longitude as a function of redshift: $-20° < b < 0°$ (left) and $0° < b < 20°$ (right). Black markers represent galaxies from literature (LEDA). Blue markers show the GA-GPS galaxy detections. Regions outside of the boundary of GA-GPS are shaded in grey.

first identified by Tully & Fisher (1987). While the observed emptiness of this region is exacerbated by foreground extinction and stellar confusion, the low galaxy density is genuine and extends outside of the ZoA (Kraan-Korteweg et al., 2008a).

Mapping underdensities is equally as important as mapping overdensities when trying to understand large scale dynamics, and the Local Void's close proximity ($V_{\rm hel} \leq 6000\,{\rm km\,s^{-1}}$) makes it ideal to study in detail with GPS. The GA-GPS region encompasses only the very edge of void, the boundaries of which lie within $330° < \ell < 60°$ (Kraan-Korteweg et al., 2008a). However, the larger GPS-HI survey fully encompasses the Local Void, of which the ceiling and floor have been poorly documented in redshift surveys until now (Tully et al., 2019). Findings will be released in Kurapati et al., (in prep).

Figure 4.22, an overview plot, is an on-sky distribution populated with the GA-GPS detections (filled dots) and previously measured galaxies from literature (HIZOA & HyperLeda; open dots), subdivided into panels of $\Delta V = 4000\,{\rm km\,s^{-1}}$ of increasing velocity bins as indicated. This overview, spanning an on-sky area much larger than the GA-GPS footprint ($360° > \ell > 270°$; $-20° > b > 20°$), reveals wall-like structures and a multi-branching of filaments, with the ZoA appearing somewhat populated in the first panels; which is then followed by a decrease in galaxy numbers with increasing redshift bins. The last three panels have no points from literature along the plane ($|b| \lesssim 3°$). Figure. 4.23 looks

more closely at the two largest velocity peaks in GA-GPS, i.e., $3500 < V < 7500\,\mathrm{km\,s^{-1}}$ and $10\,500 < V < 15\,500\,\mathrm{km\,s^{-1}}$

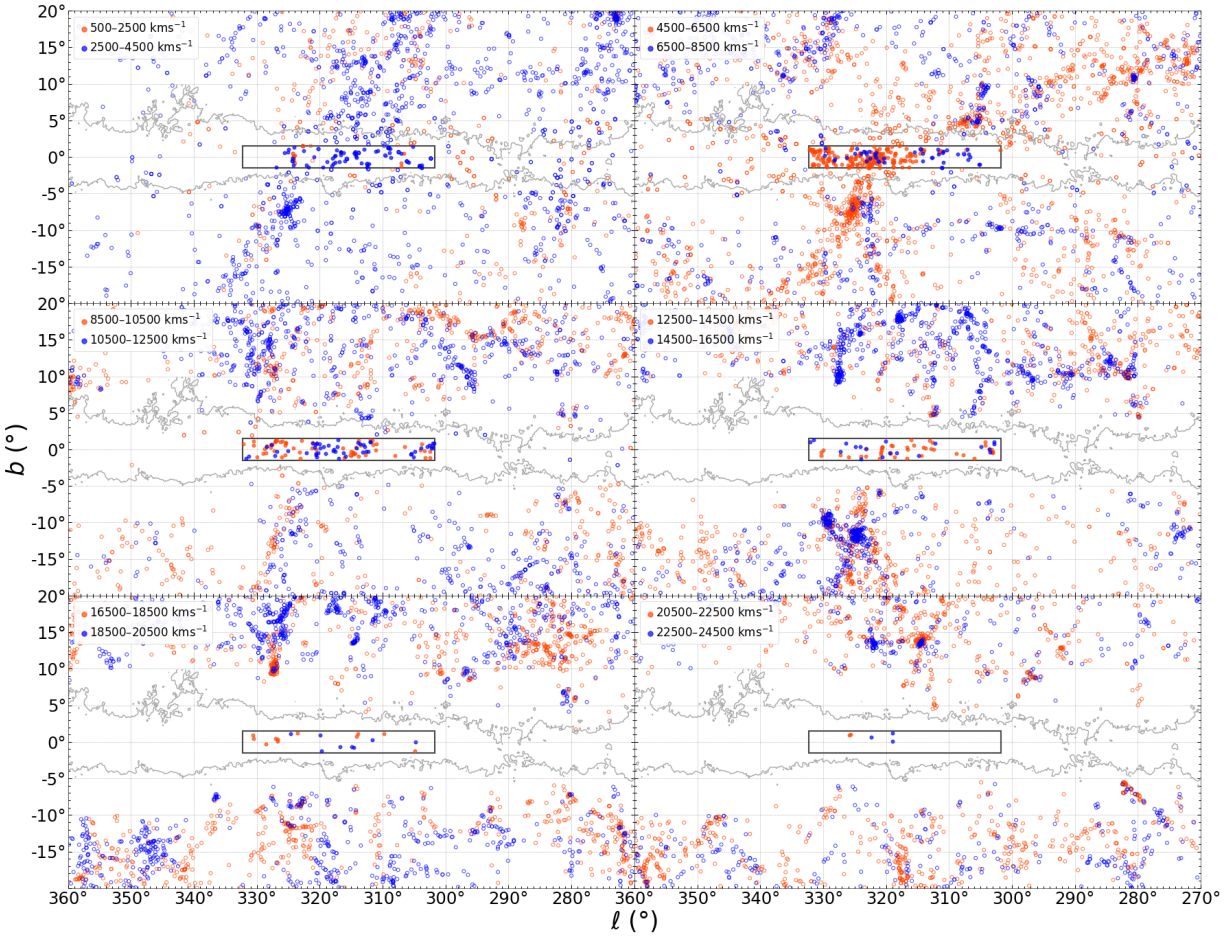

Figure 4.22: An overview of the GA-GPS detections (filled dots) combined with galaxies from literature (HIZOA & HyperLeda; open dots) between $360° > \ell > 270°$ and $-20° > b > 20°$. The sample is divided into velocity bins as indicated. The black box represents the GA-GPS search area. The grey contour marks a line of equal Galactic foreground extinction ($A_B = 3.0$m) as derived from the IRAS/DIRBE maps (Schlegel et al., 1998) and corrected with a factor 0.83 as derived by Schröder et al. (2021), where hardly any galaxies are known.

The top panel of Fig. 4.23 concentrates on the velocity range $3500 - 7500\,\mathrm{km\,s^{-1}}$, which encompasses the peak of the GA and the two shoulders. The Norma cluster is prominent at $(\ell,\ b,\ V_{\mathrm{hel}}) = (325.3°,\ -7.2°,\ 4871\,\mathrm{km\,s^{-1}})$; its $925\,\mathrm{km\,s^{-1}}$ velocity dispersion (Woudt et al., 2008) allowing it to infiltrate more than one velocity bin. The Norma cluster appears

to be the centre of a web, a bridge extending up and to the right, crossing the Galactic plane and connecting to the Centaurus-Crux cluster at (ℓ, b, V) $\approx$ (306°, 6°, 6200 km s^{-1}). Although just below the view of this plot, the GA wall is believed to connect all the way down to the Pavo II cluster (ℓ, b, $V_{\rm hel}$) = (332°, −24°, 4167 km s^{-1}) (Woudt et al., 2008). Towards the right of the black rectangle, the PKS1343 cluster appears in orange at (ℓ, b, $V_{\rm hel}$) = (309.7°, 1.7°, 3872 km s^{-1}), and seems to connect straight up to higher latitudes.

This plot can be compared to Fig. 1 in Woudt et al. (2008), which shows a similar longitude and velocity range, populated with optically detected galaxies from Woudt & Kraan-Korteweg (2001). It is evident from this figure that, despite the best optical efforts, much of the dust-obscuration around $b \simeq 0°$ could not be penetrated and the knowledge of the GA wall crossing was not well determined. The deep HI observations of GPS provides a clear view of the wall, which appears as a smooth overdensity, as well as inter-connecting filaments.

The bottom panel of Fig. 4.23 shows the velocity range 11 500 – 15 500 km s^{-1} in more detail. This plot is particularly interesting because these redshifts at the lowest latitudes are mostly unexplored. The GA-GPS footprint (black rectangle) provides a first peak at gas-rich galaxies in a region that has been practically unattainable until now.

What stands out immediately is the dark blue groups below the plane: the Ara cluster (ℓ, b, V) = (329°, -9°, 15 060 km s^{-1}) and the nearby Triangulum-Australis cluster (ℓ, b, $V_{\rm hel}$) = (324°, -12°, 15 300 km s^{-1}) (Radburn-Smith et al., 2006). The green and blue points in the GA-GPS region hint at a connection up to the Shapley Supercluster. However, the lack of points from literature around the GA-GPS rectangle makes it difficult to trace connections with high confidence.

On the right end of the rectangle there is a trail of detections in orange and cyan — possibly a glimpse of a filament. We would need to survey an extended latitude range and merge the GA-GPS segment with lower latitudes in order to investigate further.

As is evident from Fig. 4.22, the high-redshift panels are sparse in comparison, and there are not enough points in literature (from systematic spectroscopic surveys) to put the GA-GPS detections into context with regards to structure. However, these detections are a valuable starting point and can be incorporated into future large scale maps of the ZoA and related analysis. Figures showing redshifts up to 24 500 km s^{-1} in more detail are included in Appendix B (Fig. B2).

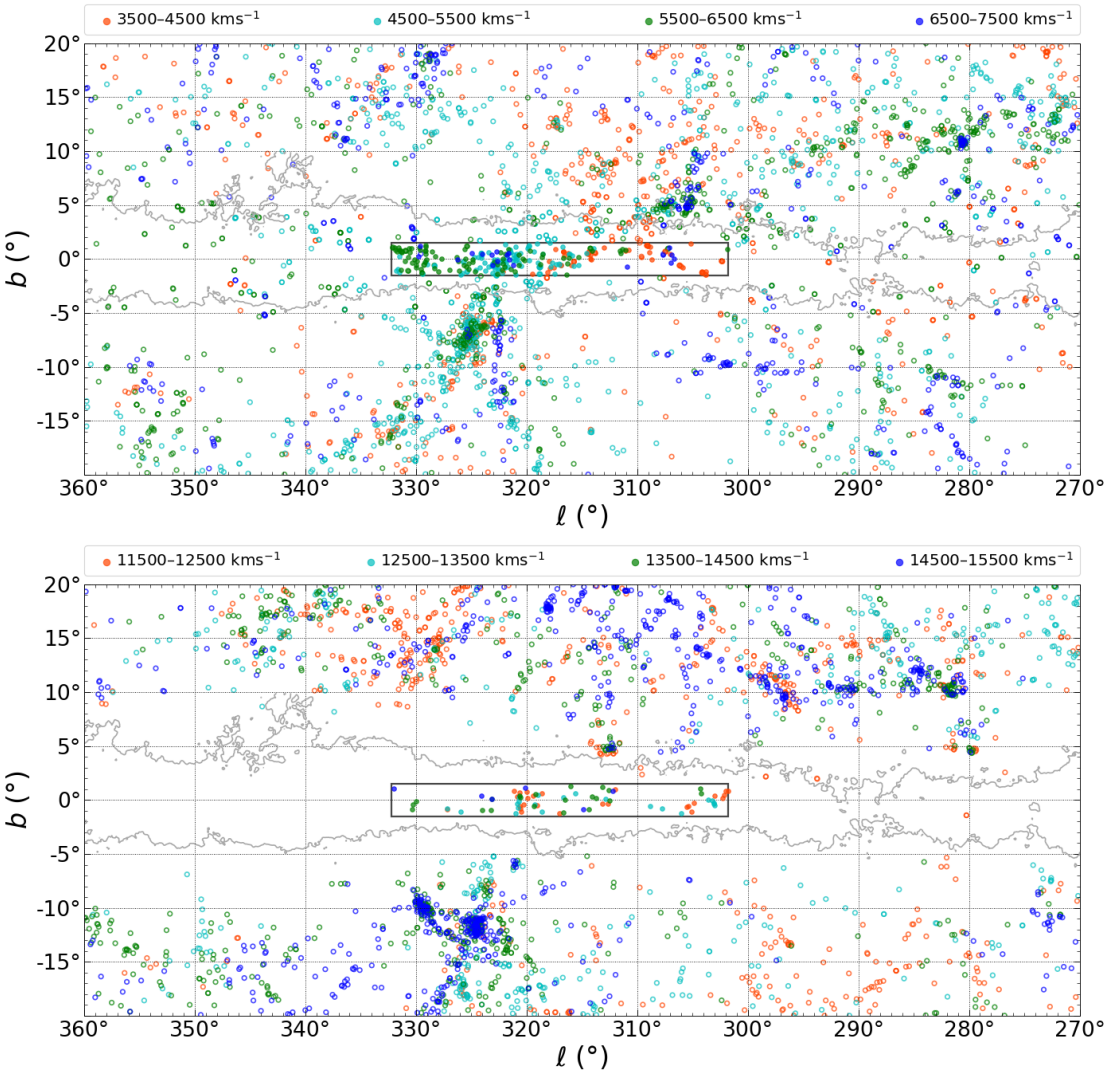

Figure 4.23: On-sky distribution of galaxies from GA-GPS (filled circles), and literature (HIZOA & HyperLeda – open circles). The top panel shows the redshift range $3500 < V_{\rm hel} < 7500\,{\rm km\,s^{-1}}$ and the bottom panel $11\,500 < V_{\rm hel} < 14\,500\,{\rm km\,s^{-1}}$. The black box represents the GA-GPS search area. The grey contour marks a line of equal Galactic foreground extinction ($A_B = 3.0$m).

4.12 GA-GPS Summary

This chapter presented the analysis and results of the HI line data of the MeerKAT GPS survey in the target area of $302° \leq \ell \leq 332°$; $-1.5° \leq b \leq 1.5°$. The rms values of the resultant HI mosaic cubes (reduced with robust=0 and taper=15") are mostly close to the mean of

0.47 mJy, with some local variations within the range 0.39 – 0.53 mJy. The origin of the periodic RFI in the frequency range 1376 – 1386 MHz (visible in Fig. 4.5) was identified as interference from Global Positioning Satellites. The continuum residuals in the data were mainly diffuse emission spread out over larger areas, resulting in regions of higher noise, whereas compact sources were eliminated more successfully.

In Sect. 4.10, the calibration of our derived fluxes was found to be of high standard, with our integrated fluxes following a near-linear trend as compared to HIZOA. The good agreement between the two surveys — in flux, profile shapes, line widths, and positions in redshift space — also bodes well for the HIZOA results (observations which have not been replicated until now). The flux assessment and rigorous data quality assurance demonstrate that our reduction process with CARACal lead to good quality (dirty) HI images, sufficient for detecting HI sources as well as accurately measuring the flux.

For the source-finding process, one mosaic cube (T12) was chosen as a representative case to undergo a full visual search for HI sources. SoFiA was implemented to search this same mosaic. The search parameters were fine-tuned through iteratively searching T12 until all visual detections were recovered, or as many as reasonably possible. This process resulted in a list of optimised parameter settings. Automated source finding was used from then on to identify galaxy candidates in the remainder of the GA-GPS mosaics.

When trying to extract sources with lower flux, any change in SoFiA 's source-finding parameters results in the removal or addition of detections near the detection threshold, largely as a result of stochastic fluctuations (Healy et al., 2021). Consequently, we were not able to maximise the number of visual detections recovered using a single set of SoFiA parameters — if we recovered an additional galaxy, another would fall away. Hence, the decision was made to implement three consecutive runs, and then merge the results. After the first run, the maximum z-length (LINKER.MAXSIZEZ) was increased from 21 to 31, then the flux threshold (SCFIND.THRESHOLD) was lowered from 4σ to 3.5σ. This method recovered 87 out of the 93 visual detections (the remaining six being of low flux density), giving a completeness of 93.5% for mosaic T12. Some additional detections that were missed in the visual search were also catalogued.

The GA-GPS catalog is a quantitative and qualitative advancement on the published HIZOA catalog. Compared to the HIZOA survey, the number of galaxies detected in the relevant ∼90 deg^2 on-sky region was increased by almost ten-fold (42 versus 382 for $V_{\mathrm{hel}} < 12\,000\,\mathrm{km\,s^{-1}}$). In terms of quality, the low spatial resolution of HIZOA did not permit a differentiation of neighbouring galaxies closer than ∼5' on-sky. Within the GA-GPS data, four HIZOA detections were discovered to be composed of more than one

source (cf. Sect. 4.9.1), owing to the improved resolving power of the MeerKAT interferometer over the Parkes dish. Even more interestingly, one of the HIZOA counterparts was revealed to be much more massive than originally documented. This strange source is so extended that it falls far from the established HI mass-diameter relation (Wang et al., 2016).

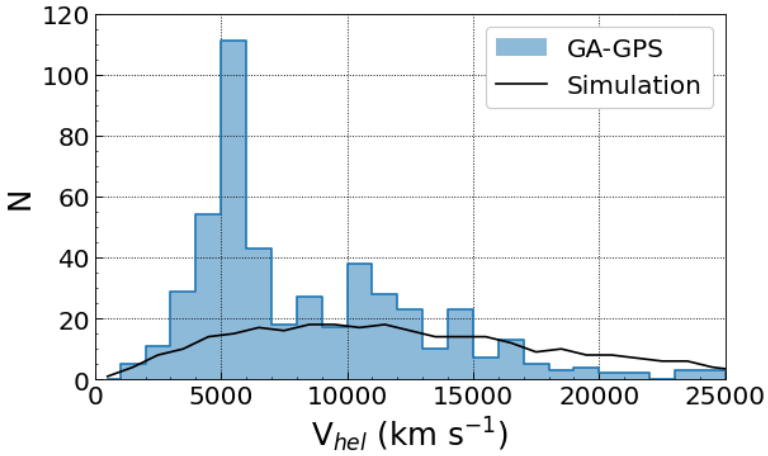

Figure 4.24: The velocity distribution of the GA-GPS galaxy candidates is shown in blue. The black line represents the scaled-down galaxy distribution predicted by the simulation.

The distribution of the GA-GPS catalog can be compared to the predicted detections from the simulations (courtesy of L. Staveley-Smith). Figure 4.24 displays the number of galaxy candidates from GA-GPS as a function of redshift (blue histogram), and the black line represents the distribution given by the simulation. Since the simulation results cover 528 deg^2, the number density in the plot has been scaled down to be representative of an average galaxy density (i.e., excluding the highest overdensity peaks) within a volume similar to that of GA-GPS. This comparison highlights the magnitude of the GA overdensity compared to an homogeneous universe. The number of galaxies in the bins between $3000-7000\,\mathrm{km\,s^{-1}}$, in this scaled comparison, is a factor $f\sim4$ times more than the simulated curve. This rough comparison insinuates that the segment of the GA wall that intersects the narrow GA-GPS strip has approximately four times the galaxy density compared to a typical segment of space of the same size which does not contain overdensities.

At further redshifts ($\gtrsim 15\,000\,\mathrm{km\,s^{-1}}$) the galaxy density of GA-GPS is less than predicted. This could be a combination of two factors: firstly, our rms noise was on average slightly higher than the 0.45 mJy used for the simulation ($\gtrsim 0.5$ mJy in some places),

which could lower our detection rate, particularly at higher redshifts; secondly, this patch of sky could genuinely be underdense. Based solely on these results, we cannot say for certain which of these is the dominating factor; although, preliminary analysis of the VSCL region of the GPS survey (Rajohnson et al., in prep.) does find overdensities at high redshifts (with a slightly lower rms). Furthermore, if we were incomplete, we would expect the high redshift detections to be higher $M_{\rm HI}$ galaxies. The fact that the high redshift detections lie close to the HI mass limit (cf. Fig. 4.18) could be an indication that we have a real underdensity. The results of the full GPS survey (spanning $248^\circ \leq \ell \leq 60^\circ$) will provide more clarity.

Chapter 5

Discussion and Outlook

This work analysed two extragalactic HI surveys conducted with MeerKAT — an SKA precursor array. In Chapter 3 I analysed a MeerKAT16 pilot survey which consisted of six individual pointings, aimed at the Vela Supercluster (VSCL). Chapter 4 presented a $\sim 3^\circ \times 30^\circ$ on-sky section of the Galactic Plane Legacy Survey (GPS), conducted with the completed MeerKAT array, lending a strong focus to the Great Attractor (GA) region.

In this final chapter, I summarise the science highlights and discuss the results and insights gained from the previous two chapters, then conclude with future prospects.

5.1 Discussion

Early Science projects such as MeerKAT16 were performed at intermediate stages during the installation of the full array to test and optimise the running of the telescope. Pilot projects also serve as a test-bed for technologies and software that will be crucial to future surveys — such as source-finding pipelines (in this case, SoFiA).

The 16-dish configurations already allowed for significant science results with the three hour on-source integration time, resulting in 119 solid galaxy candidates (and an additional 37 candidates with lower certainty), which allowed for detailed mapping of the region around the cluster VC04. The locations of these galaxy candidates are shown in red in Fig. 5.1. This on-sky distribution puts the MeerKAT16 results from Chapter 3 in context with the GA-GPS results from Chapter 4, shown in green.

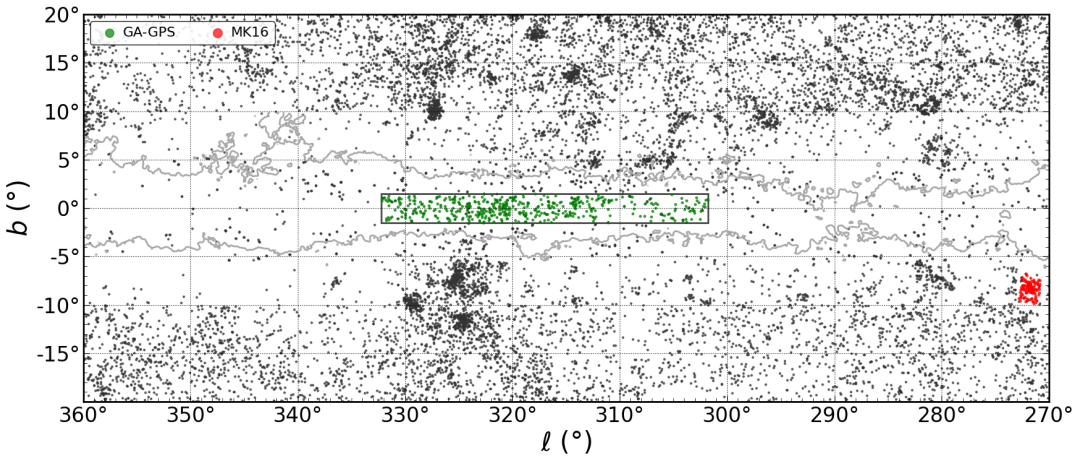

Figure 5.1: On-sky distribution showing the galaxy detections from MeerKAT16 (red dots) and GA-GPS (green dots). Black dots are galaxies from literature (HIZOA & HyperLeda). The black box represents the GA-GPS search area. The grey contour marks a line of equal Galactic foreground extinction (A_B = 3.0m).

The deep HI observations of GPS encompassed the inner-most Galactic plane, where past surveys mostly excluded some fraction of the ZoA due to the difficulties in penetrating the region (e.g., 2MRS; Huchra et al., 2012; Macri et al., 2019; Lambert et al., 2020). GA-GPS — although a narrow strip — has lifted the veil of the Milky Way considerably, probing a volume far beyond the deepest systematic HI survey in the southern ZoA to date (the HIZOA survey; Staveley-Smith et al., 2016). I catalogued 477 galaxy candidates: 406 strong detections (category 1) and 71 with slightly lower confidence (category 2).

The GA overdensity is densely populated, manifesting as a broad wall-like structure that extends above and below the Galactic plane. The new GPS data did not uncover any previously unknown galaxy clusters lurking at the GA distance (and no more are hypothesised). Nonetheless, this work (including MeerKAT16 and GA-GPS) assisted in populating regions obscured by the ZoA and improved current knowledge of over- and underdensities.

Enormous insight into large scale structure was garnered from the narrow 30° GA-GPS strip. Clusters, filaments and voids are recovered and striking new details of the GA wall are revealed. Individual HI galaxies around $b \simeq 0°$ are parametrised in the velocity range $12\,000 - 25\,000\,\mathrm{km\,s^{-1}}$ for the first time — where there are no counterparts in literature. The GA-GPS galaxy candidates, the majority of which are new discoveries, have unquestionably contributed towards narrowing the ZoA in redshift space and their

HI measurements can be used for future analysis, e.g., as supplementary data in reckoning the peculiar velocity field. This bodes well for the future, since it clearly demonstrates that deep interferometric HI surveys have the power to unveil the large scale structure of galaxies all the way across the ZoA, even at the lowest, most opaque latitudes which have so far remained impenetrable for extragalactic studies.

Large radio surveys are becoming progressively more reliant on automated source finding algorithms. Therefore testing source finders and quantifying their accuracy is vital (Hopkins et al., 2015). In this dissertation we explored the limitations of SoFiA in the case of real (non-uniform) data. We showed that the negative density method of extracting reliable sources (Serra et al., 2012) can achieve a high completeness, and give reliable parameters — even with the presence of RFI and continuum residuals. However, as the source-finding methodology of Chapters 3 and 4 showed, running source finders on real data does have limitations (Hopkins et al., 2015). Basic assumptions made by the SoFiA algorithms (e.g., that the noise is Gaussian) make it difficult to tune when cubes have a complicated noise structure. In addition, manual intervention is still crucial. Spurious detections need to be removed, and sometimes detections that were overlooked by the source finder need to be added. In particular, we found that SoFiA is not good at identifying extended structures — at least with respect to the parameter settings we tried. Moreover, it is very important to be aware of where the noisy regions are in the data and to be especially critical of sources extracted from these regions.

Recovering 93.5% of the visual detections in GPS mosaic T12 is a respectable result in terms of SoFiA 's completeness, but the trade-off is that false positives are accumulated with every run, all of which have to be removed via manual inspection. In Sect. 4.7.3 we showed that using multiple SoFiA runs with different parameter settings and combining the results did catch additional genuine detections that would otherwise have been lost. However, as a consequence we roughly tripled the false positives, lowering the reliability of our SoFiA output. That considered, the use of SoFiA was a major advantage and the HI analysis would not have been feasible without SoFiA 's efficient and rigorous parametrisation.

A trade-off between completeness and reliability is inherent in automated source identification (e.g., Hopkins et al., 2015; Healy et al., 2021). For the analysis of GPS, we opted for high completeness at the expense of reliability, which resulted in a laborious adjudication process, but culminated in a robust galaxy catalog. A source finder suitable for large spectral line surveys with high completeness and high reliability does not yet exist (Hopkins et al., 2015), and further refinements are necessary; fortunately, several

existing source finders are under continuous development (e.g., Popping et al. (2012) presents a comparison of HI source finders), and our findings served as useful feedback to the SoFiA working group.

5.2 Future Perspectives

The next logical step in the GPS project is to combine the results of the entire $248^\circ \leq \ell \leq 60^\circ$ strip, as different segments are being analysed by different members of the team. Following this, we can compute the HI mass function (HIMF), as was done for HIZOA (see Said et al., 2019). Since we are sensitive to low $M_{\rm HI}$ dwarfs, the GPS data will be particularly useful in determining the low $M_{\rm HI}$ end of the HIMF, which has historically been under-sampled (e.g., Kraan-Korteweg et al., 2008b; Maddox et al., 2021).

The GA-GPS sources were cross-matched with literature and counterparts were found: 40 in HIZOA and 2 in GLIMPSE (Jarrett et al., 2007). We can search for further counterparts in WISE and Spitzer (IR) data: this is applicable to the full GPS survey and the MeerKAT16 galaxy candidates.

Considering the success of GPS in uncovering large scale structure at the lowest latitudes, further observations extending to higher latitudes would allow us to trace the GA wall from beginning to end — similarly to what is currently being pursued with the MeerKAT64 VSCL survey; i.e., an extension of GPS to $b \pm 7^\circ$ (Rajohnson et al., in prep). Furthermore, additional data covering $b > \pm 1.5^\circ$ could provide further evidence for the suspected connection between Triangulum-Australis and Shapley.

The redshifts obtained from the MeerKAT16 Early Science data and the GPS HI observations can potentially be used to model the peculiar velocities: if a substantial sub-sample of IR counterparts could be obtained, a NIR-Tully-Fisher analysis could be performed, which will allow for an assessment of the shapes and content of the gravitational basins of the Vela and GA overdensities (Courtois et al., 2019, Courtois et al., submitted). In addition, deriving an actual mass estimate of the GA wall overdensity — as was done by Kraan-Korteweg et al. (2011) using NIR data — will help to compute to what degree the GA is gravitationally disruptive to the flow of galaxies in the local Universe. This result would be relevant in the controversy over the peculiar motion of our Local Group: whether the GA or Shapley exerts a stronger pull (cf. Sect. 1.3).

One instance of GPS-related future work is already underway. As mentioned in Chapter 4, Sect. 4.8.1, an exceptionally large spiral galaxy with low column density was uncovered in the GA-GPS data directly behind the Galactic plane — its extension on the sky measuring

roughly $40' \times 30'$ (corresponding to $\sim 225 \times 170$ kpc). Very large HI galaxies like this are extremely rare and little is known about their properties (Kraan-Korteweg et al., 2009). An extra 16 hours of MeerKAT commissioning time was awarded to do follow-up observations of this unusual object, using the 32K correlator. The improved velocity resolution ($44.1\,\mathrm{km\,s^{-1}}$ vs $\sim 10\,\mathrm{km\,s^{-1}}$) will allow much more detailed mapping of the structure and add immense value to our understanding of large galaxies. Results will be released in a future paper.

The highly encouraging results of the MeerKAT16 pilot survey (Chapter 3) and the MeerKAT-GPS Legacy survey (Chapter 4) demonstrate the HI exploration power of the MeerKAT array as well as the potential of the long-anticipated full SKA array, expected to be fully operational by the late 2020s.

Acknowledgements

The MeerKAT telescope is operated by the South African Radio Astronomy Observatory, which is a facility of the National Research Foundation, an agency of the Department of Science and Innovation.

This research was supported by the South African Research Chairs Initiative (SARChI) of the Department of Science and Technology and National Research Foundation.

This research has made use of the SoFiA software, which has been made freely available to the entire community under an open-source licence. The source code of SoFiA 1 is available from GitHub at https://github.com/SoFiA-Admin/SoFiA/. The source code of SoFiA 2 is available from GitHub at https://github.com/SoFiA-Admin/SoFiA-2/.

We acknowledge the use of the Ilifu cloud computing facility,[1] a partnership between the University of Cape Town, the University of the Western Cape, the University of Stellenbosch, Sol Plaatje University, the Cape Peninsula University of Technology and the South African Radio Astronomy Observatory. The Ilifu facility is supported by contributions from the Inter-University Institute for Data Intensive Astronomy (IDIA – a partnership between the University of Cape Town, the University of Pretoria, the University of the Western Cape and the South African Radio astronomy Observatory), the Computational Biology division at UCT and the Data Intensive Research Initiative of South Africa (DIRISA).

We acknowledge the usage of the HyperLeda database[2].

We acknowledge the use of the SAO/NASA Astrophysics Data System[3].

[1] www.ilifu.ac.za
[2] http://leda.univ-lyon1.fr
[3] http://ui.adsabs.harvard.edu/

Bibliography

Aaronson, M., Huchra, J., Mould, J., Schechter, P. L., & Tully, R. B. 1982, ApJ, 258, 64

Abell, G. O., Corwin, Harold G., J., & Olowin, R. P. 1989, ApJS, 70, 1

Barnes, D. G., Staveley-Smith, L., de Blok, W. J. G., et al. 2001, MNRAS, 322, 486

Blyth, S., Baker, A. J., Holwerda, B., et al. 2016, in MeerKAT Science: On the Pathway to the SKA, 4

Boehringer, H., Neumann, D. M., Schindler, S., & Kraan-Korteweg, R. C. 1996, ApJ, 467, 168

Bolejko, K., & Hellaby, C. 2008, General Relativity and Gravitation, 40, 1771

Booth, R. S., & Jonas, J. L. 2012, African Skies, 16, 101

Boruah, S. S., Hudson, M. J., & Lavaux, G. 2020, MNRAS, 498, 2703

Brandt, W. N., & Hasinger, G. 2005, ARAA, 43, 827

Brandt, W. N., & Yang, G. 2021, arXiv e-prints, arXiv:2111.01156

Calabretta, M. R., Staveley-Smith, L., & Barnes, D. G. 2014, PASA, 31, e007

Comrie, A., Wang, K.-S., Hsu, S.-C., et al. 2021, CARTA: The Cube Analysis and Rendering Tool for Astronomy, Zenodo, doi:10.5281/zenodo.3377984

Cornwell, T. J. 1988, A&A, 202, 316

Courtois, H. M., Kraan-Korteweg, R. C., Dupuy, A., Graziani, R., & Libeskind, N. I. 2019, MNRAS, 490, L57

de Vaucouleurs, G. 1958, Nature, 182, 1478

Dekel, A. 1994, ARAA, 32, 371

Donley, J. L., Staveley-Smith, L., Kraan-Korteweg, R. C., et al. 2005, AJ, 129, 220

Dressler, A., Faber, S. M., Burstein, D., et al. 1987, ApJL, 313, L37

Driessen, L. 2020, Astronomy and Geophysics, 61, 5.12

Ebeling, H., Edge, A. C., Allen, S. W., et al. 2000, MNRAS, 318, 333

Ebeling, H., Mullis, C. R., & Tully, R. B. 2002, ApJ, 580, 774

Epchtein, N., de Batz, B., Capoani, L., et al. 1997, The Messenger, 87, 27

Ewen, H. I., & Purcell, E. M. 1951, Nature, 168, 356

Fairall, A. P. 1998, Large-Scale Structures in the Universe, Wiley-Praxis Series in Astronomy and Astrophysics (New York : Wiley)

Field, G. B. 1958, Proceedings of the IRE, 46, 240

Giovanelli, R., & Haynes, M. P. 2015, AAPR, 24, 1

Gooch, R. 1996, in Astronomical Society of the Pacific Conference Series, Vol. 101, Astronomical Data Analysis Software and Systems V, ed. G. H. Jacoby & J. Barnes, 80

Gould, A. 1993, ApJL, 412, L55

Hatamkhami, N. 2022, PhD thesis, University of Cape Town, unveiling of the newly discovered Vela Supercluster.

Healy, J., Deb, T., Verheijen, M. A. W., et al. 2021, A&A, 654, A173

Henning, P. A., Staveley-Smith, L., Ekers, R. D., et al. 2000, AJ, 119, 2686

Herschel, J. F. W. 1864, Philosophical Transactions of the Royal Society of London Series I, 154, 1

Hoffman, Y., Courtois, H. M., & Tully, R. B. 2015, MNRAS, 449, 4494

Hoffman, Y., Pomarède, D., Tully, R. B., & Courtois, H. M. 2017, Nature Astronomy, 1, 0036

Högbom, J. A. 1974, AAPS, 15, 417

Hopkins, A., Whiting, M., Seymour, N., et al. 2015, Publications of the Astronomical Society of Australia, 32, doi:10.1017/pasa.2015.37

Hubble, E. 1929, Proceedings of the National Academy of Science, 15, 168

Huchra, J. P., Macri, L. M., Masters, K. L., et al. 2012, ApJS, 199, 26

Hudson, M. J., Smith, R. J., Lucey, J. R., & Branchini, E. 2004, MNRAS, 352, 61

Jakiel, R. 2000, Sky & Telescope, retrieved from The Free Library: https://www.thefreelibrary.com/Behind+the+Veil%3a+Exploring+the+IC+342+Galaxy+Group.-a061372201

Jarrett, T. H., Chester, T., Cutri, R., et al. 2000, AJ, 120, 298

Jarrett, T. H., Koribalski, B. S., Kraan-Korteweg, R. C., et al. 2007, AJ, 133, 979

Jarvis, M., Taylor, R., Agudo, I., et al. 2016, in MeerKAT Science: On the Pathway to the SKA, 6

Johnston, S., Taylor, R., Bailes, M., et al. 2008, Experimental Astronomy, 22, 151

Józsa, G. I. G., White, S. V., Thorat, K., et al. 2020, arXiv e-prints, arXiv:2006.02955

Juraszek, S. J., Staveley-Smith, L., Kraan-Korteweg, R. C., et al. 2000, AJ, 119, 1627

Kerr, F. J., & Henning, P. A. 1987, ApJL, 320, L99

Kerr, F. J., & Hindman, J. V. 1953, AJ, 58, 218

Kocevski, D. D., & Ebeling, H. 2006, ApJ, 645, 1043

Kocevski, D. D., Ebeling, H., & Mullis, C. R. 2004a, in Clusters of Galaxies: Probes of Cosmological Structure and Galaxy Evolution, ed. J. S. Mulchaey, A. Dressler, & A. Oemler, 26

Kocevski, D. D., Ebeling, H., Mullis, C. R., & Tully, R. B. 2007, The Astrophysical Journal, 662, 224

Kocevski, D. D., Ebeling, H., Tully, R. B., & Mullis, C. R. 2005, in American Astronomical Society Meeting Abstracts, Vol. 207, American Astronomical Society Meeting Abstracts, 162.03

Kocevski, D. D., Mullis, C. R., & Ebeling, H. 2004b, ApJ, 608, 721

Kogut, A., Lineweaver, C., Smoot, G. F., et al. 1993, ApJ, 419, 1

Kolatt, T., Dekel, A., & Lahav, O. 1995, MNRAS, 275, 797

Koribalski, B. S. 2012, PASA, 29, 359

Koribalski, B. S., Staveley-Smith, L., Kilborn, V. A., et al. 2004, AJ, 128, 16

Koribalski, B. S., Staveley-Smith, L., Westmeier, T., et al. 2020, , 365, 118

Kovač, K., Oosterloo, T. A., & Van Der Hulst, J. M. 2009, Monthly Notices of the Royal Astronomical Society, 400, 743

Kraan-Korteweg, R. C. 2005, Reviews in Modern Astronomy, 18, 48

Kraan-Korteweg, R. C., Cluver, M. E., Bilicki, M., et al. 2017, MNRAS, 466, L29

Kraan-Korteweg, R. C., Cluver, M. E., Jarrett, T. H., & Woudt, P. A. 2009, in Panoramic Radio Astronomy: Wide-field 1-2 GHz Research on Galaxy Evolution, 27

Kraan-Korteweg, R. C., Fairall, A. P., & Balkowski, C. 1995, A&A, 297, 617

Kraan-Korteweg, R. C., Henning, P. A., & Schröder, A. C. 2002, A&A, 391, 887

Kraan-Korteweg, R. C., & Huchtmeier, W. K. 1992, A&A, 266, 150

Kraan-Korteweg, R. C., Jarrett, T. H., Elagali, A., et al. 2015, in SALT Science Conference 2015 (SSC2015), 40

Kraan-Korteweg, R. C., & Lahav, O. 2000, AAPR, 10, 211

Kraan-Korteweg, R. C., Riad, I. F., Woudt, P. A., Nagayama, T., & Wakamatsu, K. 2011, arXiv e-prints, arXiv:1107.1069

Kraan-Korteweg, R. C., Shafi, N., Koribalski, B. S., et al. 2008a, in Astrophysics and Space Science Proceedings, Vol. 5, Galaxies in the Local Volume, 13

Kraan-Korteweg, R. C., Staveley-Smith, L., Donley, J., & Henning, P. A. 2003, arXiv e-prints, astro

Kraan-Korteweg, R. C., van Derheyden, K. J., Cluverand, M. E., & Woudt, P. A. 2008b, in First Middle East-Africa Regional IAU Meeting, 8

Kraan-Korteweg, R. C., & Woudt, P. A. 1999, PASA, 16, 53

Kraan-Korteweg, R. C., Woudt, P. A., Cayatte, V., et al. 1996, The Messenger, 84, 17

Kraan-Korteweg, R. C., Elson, E., Blyth, S., et al. 2016, in MeerKAT Science: On the Pathway to the SKA, 21

Lah, P., Pracy, M. B., Chengalur, J. N., et al. 2009, MNRAS, 399, 1447

Lambert, T. S., Kraan-Korteweg, R. C., Jarrett, T. H., & Macri, L. M. 2020, MNRAS, 497, 2954

Lavaux, G., & Hudson, M. J. 2011, MNRAS, 416, 2840

Lavaux, G., Tully, R. B., Mohayaee, R., & Colombi, S. 2010, ApJ, 709, 483

Lilley, A. E., & Palmer, P. 1968, ApJS, 16, 143

Lucey, J., Radburn-Smith, D., & Hudson, M. 2005, in Astronomical Society of the Pacific Conference Series, Vol. 329, Nearby Large-Scale Structures and the Zone of Avoidance, ed. A. P. Fairall & P. A. Woudt, 21

Lynden-Bell, D., Faber, S. M., Burstein, D., et al. 1988, ApJ, 326, 19

Macri, L. M., Kraan-Korteweg, R. C., Lambert, T., et al. 2019, ApJS, 245, 6

Maddox, N., Frank, B. S., Ponomareva, A. A., et al. 2021, A&A, 646, A35

Mauch, T., Cotton, W. D., Condon, J. J., et al. 2020, ApJ, 888, 61

Meyer, M. J., Zwaan, M. A., Webster, R. L., et al. 2004, MNRAS, 350, 1195

Nagayama, T., Woudt, P. A., Nagashima, C., et al. 2004, MNRAS, 354, 980

Pence, W. D., Chiappetti, L., Page, C. G., Shaw, R. A., & Stobie, E. 2010, A&A, 524, A42

Penzias, A. A., & Wilson, R. W. 1965, ApJ, 142, 1149

Pillay, V. 2020, Optimisation of Source Finding Algorithms in Early MeerKAT HI Surveys, undergraduate Honours Thesis. University of Cape Town.

Popping, A., Jurek, R., Westmeier, T., et al. 2012, PASA, 29, 318

Proctor, R. 1878, The Universe of Stars: Presenting Researches Into and New Views Respecting the Constitution of the Heavens (Longmans, Green, and Company)

Radburn-Smith, D. J., Lucey, J. R., Woudt, P. A., Kraan-Korteweg, R. C., & Watson, F. G. 2006, Monthly Notices of the Royal Astronomical Society, 369, 1131

Ramatsoku, M., Verheijen, M. A. W., Kraan-Korteweg, R. C., et al. 2016, MNRAS, 460, 923

Said, K., Kraan-Korteweg, R. C., & Staveley-Smith, L. 2019, MNRAS, 486, 1796

Saunders, W., Sutherland, W. J., Maddox, S. J., et al. 2000, MNRAS, 317, 55

Schlegel, D. J., Finkbeiner, D. P., & Davis, M. 1998, ApJ, 500, 525

Schmidt, M. 1959, ApJ, 129, 243

Schröder, A. C., van Driel, W., & Kraan-Korteweg, R. C. 2021, MNRAS, 503, 5351

Scrimgeour, M. I., Davis, T. M., Blake, C., et al. 2016, MNRAS, 455, 386

Serra, P., Jurek, R., & Flöer, L. 2012, PASA, 29, 296

Serra, P., Westmeier, T., Giese, N., et al. 2015, MNRAS, 448, 1922

Smith, R. J., Hudson, M. J., Lucey, J. R., Schlegel, D. J., & Davies, R. L. 2000, in Astronomical Society of the Pacific Conference Series, Vol. 201, Cosmic Flows Workshop, ed. S. Courteau & J. Willick, 39

Springob, C. M., Hong, T., Staveley-Smith, L., et al. 2016, MNRAS, 456, 1886

Staveley-Smith, L., Kraan-Korteweg, R. C., Schröder, A. C., et al. 2016, AJ, 151, 52

Staveley-Smith, L., & Oosterloo, T. 2015, in Advancing Astrophysics with the Square Kilometre Array (AASKA14), 167

Takata, T., Yamada, T., & Saito, M. 1996, ApJ, 457, 693

Trumpler, R. J. 1930, PASP, 42, 214

Tully, R. B., & Fisher, J. R. 1987, Nearby galaxies Atlas

Tully, R. B., Pomarède, D., Graziani, R., et al. 2019, ApJ, 880, 24

Voges, W., Aschenbach, B., Boller, T., et al. 1999, A&A, 349, 389

Wakamatsu, K., Malkan, M. A., Nishida, M. T., et al. 2005, in Astronomical Society of the Pacific Conference Series, Vol. 329, Nearby Large-Scale Structures and the Zone of Avoidance, ed. A. P. Fairall & P. A. Woudt, 189

Wang, J., Koribalski, B. S., Serra, P., et al. 2016, MNRAS, 460, 2143

Weltman, A., Bull, P., Camera, S., et al. 2020, PASA, 37, e002

Westmeier, T. 2021, SoFiA 2 User Manual, version 2.3.1, available at https://github.com/SoFiA-Admin/SoFiA-2/wiki

Westmeier, T., Kitaeff, S., Pallot, D., et al. 2021, SoFiA 2: An automated, parallel HI source finding pipeline, ascl:2109.005

Wong, O. I., Ryan-Weber, E. V., Garcia-Appadoo, D. A., et al. 2006, MNRAS, 371, 1855

Wood, K. S., Meekins, J. F., Yentis, D. J., et al. 1984, ApJS, 56, 507

Woudt, P. A., & Kraan-Korteweg, R. C. 2001, A&A, 380, 441

Woudt, P. A., Kraan-Korteweg, R. C., & Fairall, A. P. 1999, A&A, 352, 39

Woudt, P. A., Kraan-Korteweg, R. C., Lucey, J., Fairall, A. P., & Moore, S. A. W. 2008, MNRAS, 383, 445

Yamauchi, S., Bamba, A., Kaneda, H., et al. 2002, in 8th Asian-Pacific Regional Meeting, Volume II, ed. S. Ikeuchi, J. Hearnshaw, & T. Hanawa, 81–82

Zwaan, M. A., Meyer, M. J., Staveley-Smith, L., & Webster, R. L. 2005, MNRAS, 359, L30

Appendix A

SoFiA Parameters

SoFiA version 1.3.2 parameters used for the MeerKAT16 source finding:

```
steps.doFilterArtefacts = true
steps.doScaleNoise = true
steps.doSCfind = true
steps.doMerge = true
steps.doReliability = true
steps.doParameterise = true
steps.doMom0 = true
steps.doMom1 = true
steps.doWriteMask = true
steps.doWriteCat = true
steps.doDebug = true
import.inFile = mosaic1.fits #mosaic2.fits
import.maskFile =
import.sources =
import.weightsFile = mosaic1_weights.fits #mosaic2_weights.fits
filterArtefacts.threshold = 4
filterArtefacts.dilation = 5
scaleNoise.method = local
scaleNoise.windowSpatial = 51
scaleNoise.windowSpectral = 31
scaleNoise.interpolation = linear
scaleNoise.statistic = mad
scaleNoise.fluxRange = all
scaleNoise.perSCkernel = true
```

```
SCfind.threshold = 3.5 #4.0
SCfind.kernels = [[0, 0, 0, 'b'], [0, 0, 3, 'b'], [0, 0, 7, 'b'], [0, 0, 15, 'b'],
[3, 3, 0, 'b'], [3, 3, 3, 'b'], [3, 3, 7, 'b'], [3, 3, 15, 'b'], [6, 6, 0, 'b'],
[6, 6, 3, 'b'], [6, 6, 7, 'b'], [6, 6, 15, 'b']]
SCfind.rmsMode = mad
SCfind.fluxRange = all
merge.radiusX = 3
merge.radiusY = 3
merge.radiusZ = 5
merge.minSizeX = 3
merge.minSizeY = 3
merge.minSizeZ = 3
reliability.threshold = 0.70
reliability.fMin = 15
reliability.scaleKernel = 0.2
reliability.makePlot = true
reliability.parSpace = ['snr_mean', 'snr_sum', 'snr_max']
writeCat.writeASCII = true
writeCat.writeXML = true
```

Table A1: The MeerKAT16 Early Science Project: Full Catalog

A brief description of the parameters follows. Parameters are given by SoFiA unless otherwise stated.

– (1) MeerKAT16 identifier, reflecting the equatorial coordinates [MK16-Jhhmmss ± ddmmss].
– (2) Mosaic (1 or 2).
– (3) Galactic longitude [deg].
– (4) Galactic latitude [deg].
– (5) Integrated flux [Jy km s^{-1}].
– (6) Local rms [Jy beam^{-1}].
– (7) Heliocentric velocity [km s^{-1}].
– (8) Line width at 20% of the peak flux density [km s^{-1}].
– (9) Line width at 50% of the peak flux density [km s^{-1}].
– (10) Reliability R (between 0 and 1) [unitless].
– (11) Mean flux density, divided by the global rms noise level and then logarithmised s_{mean} [unitless].
– (12) Summed flux density, divided by the global rms noise level and then logarithmised, s_{sum} [unitless].
– (13) Peak flux density, divided by the global rms noise level and then logarithmised, s_{max} [unitless].
– (14) SNR, as calculated with the local rms [unitless].
– (15) SNR, as calculated with the mosaic rms (1.2 mJy beam^{-1}) [unitless].
– (16) HI mass – calculated with eq. 2.4 [$\log(M_{\mathrm{HI}}/M_{\odot})$]. HI masses have not been corrected to the barycentre of the Local Group (V_{LG}).
– (17) Flag [category 1, 2 or 3, from highest confidence to lowest confidence respectively].

name J2000 (1)	Mosaic 1/2 (2)	ℓ deg (3)	b deg (4)	$S_{\rm int}$ Jy*km/s (5)	Local rms mJy/beam (6)	$V_{\rm hel}$ km/s (7)	W_{20} km/s (8)	W_{50} km/s (9)	R (10)	$s_{\rm mean}$ (11)	$s_{\rm sum}$ (12)	$s_{\rm max}$ (13)	$SNR_{\rm indiv}$ (14)	$SNR_{\rm mean}$ (15)	$M_{\rm HI}$ $\log(M_{\rm HI}/M_\odot)$ (16)	flag 1/2/3 (17)
J082742-552757	1	271.25	-9.78	0.25	3.4	12909	53	30	0.04	0.01	2.21	0.48	3.0	8.5	9.3	2
J082805-554052	1	271.46	-9.86	2.62	3.8	13651	373	323	1.00	0.13	3.18	0.66	10.7	34.1	10.4	1
J082827-551605	1	271.14	-9.58	0.16	2.2	16338	84	49	0.15	0.09	2.24	0.58	2.5	4.5	9.3	1
J082922-551707	1	271.23	-9.48	0.17	1.7	16639	123	100	0.27	0.14	2.41	0.61	2.8	3.9	9.4	2
J082940-553558	1	271.52	-9.63	5.52	2.1	4134	185	152	1.00	0.43	3.81	1.26	57.5	101.8	9.7	1
J083027-551702	1	271.32	-9.36	0.03	1.3	11960	78	32	0.03	0.28	1.79	0.50	0.7	0.8	8.3	2
J083050-545830	1	271.10	-9.13	0.11	1.6	13189	120	12	0.05	0.26	2.22	0.53	1.9	2.6	9.0	3
J083052-551059	1	271.27	-9.25	0.03	1.4	4343	28	14	0.04	0.39	1.80	0.50	1.3	1.5	7.5	3
J083101-551056	1	271.28	-9.23	0.28	1.2	9632	175	96	0.83	0.04	2.75	0.71	5.4	5.4	9.1	1
J083117-551150	1	271.32	-9.21	0.02	1.4	2545	39	26	0.09	0.30	1.70	0.52	0.9	1.0	6.9	3
J083137-544434	1	270.97	-8.91	0.23	2.7	21762	171	13	0.28	0.22	2.30	0.61	1.9	4.4	9.7	2
J083143-554337	1	271.79	-9.47	0.14	1.8	17511	118	102	0.20	0.17	2.30	0.58	2.1	3.1	9.3	1
J083144-552903	1	271.59	-9.32	0.36	1.2	13245	120	56	0.82	0.03	2.86	0.58	8.0	8.3	9.5	1
J083146-553331	1	271.66	-9.36	1.51	1.4	4145	146	131	1.00	0.49	3.43	1.03	26.3	31.4	9.1	1
J083148-544906	2	271.05	-8.93	0.08	2.5	13928	78	59	0.18	0.01	1.70	0.56	1.1	2.2	8.9	3
J083203-550416	1	271.28	-9.05	0.10	1.3	14113	69	23	0.42	0.22	2.26	0.55	2.7	3.0	9.0	2
J083215-555856	1	272.05	-9.55	0.08	2.2	16345	62	55	0.00	0.36	1.98	0.65	1.4	2.6	9.0	1
J083217-543458	2	270.89	-8.74	0.10	2.4	22359	96	81	0.17	0.16	1.87	0.54	1.3	2.7	9.4	1
J083217-555643	1	272.02	-9.53	0.23	2.0	17409	87	26	0.02	0.12	2.47	0.58	3.8	6.3	9.5	2
J083221-560623	1	272.16	-9.61	1.35	2.3	20625	165	135	0.97	-0.01	3.15	0.62	13.6	26.5	10.4	1
J083254-550228	1	271.32	-8.93	0.06	1.4	9305	69	16	0.17	0.05	1.97	0.55	1.4	1.7	8.4	3
J083258-545313	1	271.20	-8.83	0.03	2.5	12520	21	13	0.00	0.32	1.56	0.57	0.8	1.6	8.4	3
J083311-554946	1	272.00	-9.36	1.20	1.4	16933	253	204	1.00	0.10	3.32	0.72	16.4	19.0	10.2	1
J083326-545809	1	271.31	-8.83	0.11	1.8	17132	82	53	0.16	0.19	2.16	0.48	2.1	3.1	9.2	2
J083347-551116	2	271.52	-8.91	0.03	2.3	2547	22	22	0.38	0.01	1.48	0.53	1.0	1.8	7.0	3
J083350-542139	2	270.84	-8.42	0.02	2.2	13485	22	18	0.20	0.39	1.35	0.50	0.7	1.3	8.3	3
J083430-542309	2	270.92	-8.36	0.07	2.0	22077	66	17	0.34	0.16	1.76	0.59	1.3	2.1	9.2	2
J083431-545944	1	271.42	-8.72	0.60	2.4	7375	193	88	0.64	-0.01	2.79	0.58	5.5	10.9	9.2	2
J083435-543811	2	271.13	-8.50	0.07	1.3	17826	50	35	0.07	0.19	1.93	0.60	2.2	2.5	9.0	2
J083435-550905	1	271.56	-8.80	0.03	1.8	22768	37	24	0.00	0.27	1.64	0.48	0.9	1.4	8.9	3
J083437-563033	1	272.68	-9.59	0.59	4.3	4129	89	61	0.99	0.31	2.55	0.73	4.4	15.7	8.7	1
J083446-542418	2	270.96	-8.34	0.04	1.6	18137	21	9	0.37	0.24	1.66	0.57	1.5	2.0	8.8	3
J083447-550331	1	271.50	-8.72	12.87	2.3	4036	286	237	1.00	0.48	4.11	1.40	101.1	191.3	10.0	1
J083455-545851	1	271.45	-8.66	0.05	2.8	6652	42	24	0.04	0.29	1.61	0.45	0.8	1.9	8.0	2
J083456-560327	1	272.33	-9.29	0.83	1.3	8717	243	157	1.00	0.01	3.21	0.64	12.7	13.4	9.5	1
J083504-551055	1	271.62	-8.76	2.37	2.0	4280	246	217	1.00	0.19	3.41	0.83	22.8	38.0	9.3	1
J083507-555614	1	272.25	-9.20	0.33	1.1	4625	154	109	0.85	0.05	2.86	0.65	7.4	6.6	8.5	1
J083524-560214	1	272.35	-9.22	0.08	1.3	2810	80	36	0.39	0.23	2.24	0.57	2.1	2.3	7.5	2
J083526-541935	2	270.95	-8.22	0.06	1.8	17025	107	102	0.00	0.14	1.72	0.49	1.0	1.5	8.9	3

name J2000 (1)	Mosaic 1/2 (2)	ℓ deg (3)	b deg (4)	$S_{\rm int}$ Jy*km/s (5)	Local rms mJy/beam (6)	$V_{\rm hel}$ km/s (7)	W_{20} km/s (8)	W_{50} km/s (9)	R (10)	$s_{\rm mean}$ (11)	$s_{\rm sum}$ (12)	$s_{\rm max}$ (13)	$SNR_{\rm indiv}$ (14)	$SNR_{\rm mean}$ (15)	$M_{\rm HI}$ $\log(M_{\rm HI}/M_\odot)$ (16)	flag 1/2/3 (17)
J083530-542230	2	271.00	-8.24	0.07	1.7	19988	17	10	0.36	0.27	1.89	0.56	3.1	4.4	9.1	2
J083534-554842	1	272.18	-9.07	0.04	1.1	7867	35	24	0.20	0.14	1.98	0.55	1.9	1.8	8.1	3
J083535-550840	1	271.64	-8.68	0.86	2.3	4129	113	91	1.00	0.30	2.94	0.68	10.6	20.3	8.8	1
J083536-550527	1	271.59	-8.65	0.18	2.4	13431	29	17	0.36	0.34	2.27	0.59	4.1	8.2	9.2	2
J083538-543713	2	271.21	-8.37	0.26	1.2	8750	121	48	0.93	0.14	2.51	0.56	5.9	5.9	9.0	1
J083540-544304	2	271.29	-8.42	2.51	1.2	8642	365	330	1.00	0.33	3.51	0.94	33.7	33.0	10.0	1
J083547-543932	2	271.26	-8.37	0.01	1.1	7309	22	9	0.17	0.34	1.29	0.64	0.5	0.5	7.3	3
J083550-553547	1	272.03	-8.92	0.01	1.1	15833	55	33	0.32	-0.12	1.43	0.52	0.5	0.4	8.2	3
J083553-554500	1	272.16	-9.00	0.04	1.1	22881	118	113	0.11	0.40	1.94	0.60	1.0	0.9	9.0	3
J083556-550001	1	271.55	-8.56	0.06	2.8	11729	56	17	0.20	0.19	1.73	0.40	0.9	2.0	8.6	2
J083558-551222	2	271.72	-8.67	0.06	1.8	21165	58	21	0.00	0.18	1.63	0.45	1.3	1.8	9.1	3
J083559-551202	1	271.72	-8.67	0.02	2.1	12045	168	16	0.13	-0.17	1.38	0.41	0.2	0.4	8.2	3
J083602-541217	2	270.91	-8.07	11.01	2.3	1254	111	94	1.00	0.56	3.87	1.43	139.2	262.2	8.9	1
J083604-551560	1	271.78	-8.70	0.07	1.9	6436	75	72	0.14	0.18	1.98	0.52	1.3	2.1	8.2	2
J083609-544940	2	271.43	-8.43	0.17	1.2	8948	111	71	0.99	0.27	2.34	0.70	4.0	4.1	8.8	1
J083623-560951	1	272.54	-9.19	0.02	1.4	4377	79	21	0.00	0.31	1.57	0.55	0.5	0.5	7.2	3
J083626-561849	1	272.66	-9.27	0.90	2.1	8088	128	111	1.00	0.18	3.04	0.76	11.5	19.9	9.5	1
J083633-562727	1	272.79	-9.34	0.11	3.2	5467	49	22	0.18	0.42	1.89	0.57	1.4	3.8	8.2	2
J083634-545341	2	271.52	-8.42	0.10	1.2	12208	86	51	0.26	0.22	2.05	0.54	2.6	2.6	8.8	2
J083641-542537	2	271.14	-8.13	0.04	1.3	12968	44	35	0.00	0.25	1.66	0.62	1.5	1.6	8.5	3
J083643-550749	1	271.72	-8.54	0.43	2.2	10328	106	60	0.54	0.05	2.69	0.55	5.8	10.4	9.3	2
J083649-545153	2	271.51	-8.37	0.24	1.4	10247	122	82	0.74	0.21	2.43	0.64	4.7	5.5	9.1	1
J083652-541221	2	270.98	-7.98	0.11	1.7	17781	54	29	0.74	0.31	2.02	0.54	2.7	3.9	9.2	1
J083657-545411	1	271.56	-8.38	0.07	2.9	1488	80	14	0.03	0.13	1.73	0.48	0.8	1.9	6.9	2
J083707-561348	1	272.65	-9.15	0.18	1.8	20455	167	87	0.41	0.19	2.42	0.63	2.4	3.6	9.6	1
J083709-553510	1	272.13	-8.76	0.45	1.4	7946	86	72	1.00	0.45	2.92	0.83	10.4	12.3	9.1	1
J083711-540247	2	270.88	-7.84	0.10	2.2	8619	44	16	0.43	0.46	1.83	0.64	2.1	3.8	8.5	2
J083715-541631	2	271.07	-7.97	0.07	1.7	19726	42	12	0.28	0.33	1.87	0.61	2.0	2.7	9.1	3
J083721-552515	1	272.01	-8.64	0.09	1.3	847	98	58	0.29	0.19	2.20	0.56	2.2	2.4	6.5	2
J083721-551410	1	271.86	-8.53	0.09	1.7	12120	44	25	0.22	0.20	2.14	0.62	2.5	3.4	8.8	1
J083722-555727	1	272.45	-8.96	1.19	1.4	7982	290	276	1.00	0.25	3.34	0.79	15.6	17.6	9.6	1
J083734-541810	2	271.12	-7.95	0.04	1.4	15961	51	31	0.02	0.14	1.65	0.54	1.1	1.3	8.7	3
J083738-544004	2	271.42	-8.16	0.04	1.3	17013	22	16	0.10	0.43	1.71	0.61	1.8	1.9	8.7	2
J083741-550847	1	271.82	-8.44	0.17	1.5	20178	67	24	0.33	0.19	2.42	0.62	4.0	5.1	9.5	1
J083750-545044	2	271.59	-8.24	0.14	1.6	10198	156	139	0.56	0.10	2.14	0.53	2.2	2.9	8.9	2
J083751-552260	1	272.02	-8.56	2.63	1.3	9661	516	454	1.00	0.20	3.69	0.83	26.8	29.0	10.1	1
J083752-544812	1	271.55	-8.21	0.16	3.0	8629	123	108	0.11	0.16	2.10	0.48	1.4	3.6	8.8	2
J083755-560910	1	272.66	-9.01	1.01	1.8	10280	243	195	1.00	0.00	3.14	0.66	11.1	16.3	9.7	1
J083757-550009	1	271.72	-8.32	0.10	1.9	11654	90	54	0.28	0.15	2.13	0.62	1.6	2.5	8.8	1

name J2000 (1)	Mosaic 1/2 (2)	ℓ deg (3)	b deg (4)	$S_{\rm int}$ Jy*km/s (5)	Local rms mJy/beam (6)	$V_{\rm hel}$ km/s (7)	W_{20} km/s (8)	W_{50} km/s (9)	R (10)	$s_{\rm mean}$ (11)	$s_{\rm sum}$ (12)	$s_{\rm max}$ (13)	$SNR_{\rm indiv}$ (14)	$SNR_{\rm mean}$ (15)	$M_{\rm HI}$ $\log(M_{\rm HI}/M_\odot)$ (16)	flag 1/2/3 (17)
J083805-541031	2	271.06	-7.82	0.14	1.4	10355	54	21	0.91	0.27	2.18	0.71	4.1	4.8	8.9	1
J083807-541407	2	271.11	-7.85	0.02	1.2	23066	68	44	0.79	0.18	1.65	0.72	0.7	0.7	8.8	2
J083817-545324	2	271.66	-8.22	0.28	1.8	12606	131	60	0.49	0.11	2.37	0.63	4.2	6.2	9.3	1
J083821-545001	2	271.62	-8.18	0.03	1.6	4054	17	8	0.00	0.34	1.57	0.62	1.5	2.1	7.4	2
J083828-542949	2	271.36	-7.96	0.10	1.0	7987	77	53	0.02	0.28	2.06	0.58	3.4	2.9	8.5	2
J083837-555827	1	272.57	-8.83	0.11	2.0	11838	66	50	0.24	0.16	2.13	0.45	1.9	3.3	8.9	2
J083839-552814	1	272.16	-8.52	0.16	1.1	20846	267	22	0.10	0.08	2.50	0.62	2.5	2.4	9.5	3
J083846-553014	1	272.20	-8.53	0.12	1.3	6460	115	57	0.33	0.19	2.38	0.49	2.6	2.9	8.4	2
J083853-545850	1	271.79	-8.20	0.26	1.6	10270	242	212	0.27	0.13	2.62	0.62	3.3	4.2	9.1	1
J083909-544712	2	271.65	-8.06	0.04	1.4	4444	22	22	0.04	0.38	1.50	0.48	1.9	2.1	7.6	2
J083915-561211	1	272.81	-8.89	0.06	3.3	21858	22	16	0.15	0.40	1.71	0.58	1.2	3.3	9.1	3
J083915-550209	1	271.86	-8.19	0.13	1.6	1236	40	26	0.66	0.38	2.33	0.68	3.8	5.0	7.0	2
J083918-534839	2	270.88	-7.45	0.15	2.4	18911	101	85	0.25	0.13	2.00	0.54	1.9	3.8	9.4	2
J083923-540503	2	271.10	-7.61	0.09	1.3	17415	113	93	0.33	0.10	2.04	0.49	2.0	2.2	9.1	2
J083923-541915	2	271.30	-7.75	0.07	1.2	17167	85	73	0.42	0.16	1.97	0.49	2.0	2.0	9.0	2
J083936-551134	1	272.02	-8.25	0.52	1.2	19912	360	304	1.00	0.16	3.02	0.64	6.9	6.9	10.0	1
J083940-554752	1	272.51	-8.60	0.02	1.6	20849	19	15	0.27	0.13	1.53	0.34	0.8	1.0	8.6	3
J083941-550501	1	271.94	-8.17	0.03	1.3	22098	39	30	0.00	0.16	1.67	0.42	1.0	1.0	8.8	3
J083942-553347	1	272.33	-8.46	0.04	1.3	9574	45	11	0.16	0.17	1.83	0.50	1.3	1.4	8.2	2
J083945-552415	1	272.20	-8.36	0.21	1.1	7815	98	67	0.23	0.19	2.63	0.61	5.7	5.4	8.8	1
J083950-545858	1	271.87	-8.09	0.05	1.6	11645	53	37	0.22	0.28	1.87	0.51	1.1	1.6	8.5	2
J083954-544841	1	271.74	-7.98	0.33	2.5	7628	174	41	0.10	0.11	2.53	0.58	3.1	6.4	9.0	2
J083956-535251	2	270.99	-7.42	0.26	2.2	7974	97	61	0.51	0.27	2.27	0.62	3.6	6.6	8.9	2
J083956-560140	1	272.72	-8.71	0.47	3.2	18561	141	58	0.26	0.12	2.54	0.62	3.7	9.9	9.9	1
J083956-551157	1	272.05	-8.21	0.30	1.2	7796	129	96	1.00	0.29	2.79	0.70	6.8	6.7	8.9	1
J083959-553934	1	272.43	-8.48	0.05	1.7	20141	77	56	0.22	0.14	1.93	0.56	1.1	1.5	9.0	3
J084006-545548	1	271.85	-8.03	0.04	1.8	4590	67	21	0.19	0.34	1.74	0.53	0.8	1.2	7.6	3
J084006-542119	2	271.39	-7.69	0.04	1.3	15727	76	62	0.25	0.23	1.77	0.51	1.2	1.2	8.7	2
J084015-544614	2	271.73	-7.92	0.02	2.0	18481	20	14	0.32	0.40	1.35	0.63	0.8	1.4	8.6	2
J084018-544918	2	271.78	-7.94	0.38	2.1	7979	76	39	0.59	0.19	2.43	0.61	6.3	11.1	9.1	1
J084037-550310	1	271.99	-8.05	0.61	1.5	10227	119	103	1.00	0.26	3.01	0.76	11.2	14.1	9.5	1
J084038-552123	1	272.24	-8.23	0.07	1.2	19153	82	55	0.06	-0.01	2.15	0.42	1.9	2.0	9.1	3
J084051-553244	1	272.41	-8.32	0.08	1.6	18812	45	35	0.20	0.19	2.10	0.56	2.2	3.0	9.1	2
J084055-541716	2	271.40	-7.55	0.17	1.3	5242	118	39	0.89	0.12	2.32	0.56	3.6	3.9	8.3	2
J084057-553107	1	272.40	-8.29	0.45	1.6	17637	219	196	0.66	0.00	2.86	0.64	5.8	7.6	9.8	1
J084103-554116	1	272.54	-8.38	1.26	2.0	18677	316	299	0.98	0.01	3.17	0.63	10.6	17.8	10.3	1
J084104-550323	1	272.04	-8.00	1.04	1.5	12006	229	90	1.00	0.14	3.22	0.79	13.4	17.2	9.9	1
J084104-553432	1	272.46	-8.31	0.41	1.8	12078	137	62	0.86	0.13	2.78	0.63	5.9	8.8	9.5	1
J084106-545156	2	271.89	-7.88	1.20	1.9	7660	345	306	1.00	0.23	2.99	0.78	10.3	16.2	9.5	1

name J2000 (1)	Mosaic 1/2 (2)	ℓ deg (3)	b deg (4)	$S_{\rm int}$ Jy*km/s (5)	Local rms mJy/beam (6)	$V_{\rm hel}$ km/s (7)	W_{20} km/s (8)	W_{50} km/s (9)	R (10)	$s_{\rm mean}$ (11)	$s_{\rm sum}$ (12)	$s_{\rm max}$ (13)	$SNR_{\rm indiv}$ (14)	$SNR_{\rm mean}$ (15)	$M_{\rm HI}$ $\log(M_{\rm HI}/M_\odot)$ (16)	flag 1/2/3 (17)
J084106-544041	2	271.73	-7.77	0.92	1.5	11785	103	82	1.00	0.50	2.99	1.02	18.2	22.7	9.8	1
J084107-545153	1	271.89	-7.88	1.86	2.4	7653	355	329	1.00	0.11	3.28	0.77	12.4	24.8	9.7	1
J084111-545615	1	271.95	-7.91	0.72	2.2	8198	130	100	0.98	0.13	2.92	0.67	8.8	15.8	9.4	1
J084117-554646	1	272.64	-8.41	1.00	2.9	15342	165	116	0.84	0.03	2.95	0.58	8.3	19.6	10.1	1
J084124-545436	2	271.95	-7.87	0.21	2.1	9251	121	21	0.62	0.15	2.23	0.54	2.8	4.9	8.9	1
J084129-544522	2	271.83	-7.77	0.76	1.4	20896	187	101	0.99	-0.03	2.90	0.55	11.8	13.9	10.2	1
J084131-552748	1	272.40	-8.19	0.06	1.4	12227	126	20	0.17	0.07	1.99	0.55	1.2	1.4	8.6	3
J084132-534745	2	271.06	-7.18	0.04	2.5	17795	20	16	0.04	0.18	1.29	0.51	1.0	2.1	8.8	3
J084132-545503	1	271.97	-7.86	0.04	2.2	18259	39	30	0.58	0.24	1.64	0.34	0.8	1.5	8.8	3
J084132-542750	2	271.60	-7.59	0.07	1.3	22718	86	71	0.19	0.12	1.91	0.48	1.7	1.9	9.2	3
J084136-553221	1	272.47	-8.23	0.04	1.8	12052	57	45	0.36	0.12	1.72	0.39	0.8	1.2	8.4	3
J084139-541314	2	271.42	-7.43	0.50	1.4	12161	151	70	0.58	0.14	2.74	0.61	9.1	10.3	9.6	1
J084141-551641	1	272.27	-8.06	0.39	1.6	17595	298	202	0.94	0.13	2.79	0.64	4.3	5.6	9.8	1
J084147-545148	2	271.94	-7.80	1.08	1.6	10395	176	112	1.00	0.08	3.02	0.59	15.6	20.6	9.8	1
J084155-542957	2	271.66	-7.56	0.12	1.3	21073	215	90	0.47	0.10	2.15	0.52	1.8	2.0	9.4	2
J084157-542721	2	271.63	-7.53	0.03	1.1	18685	9	6	0.00	0.12	1.52	0.49	2.6	2.4	8.7	3
J084210-551052	1	272.23	-7.95	0.37	1.8	12026	110	96	0.65	0.02	2.70	0.61	5.8	8.7	9.4	1
J084220-544652	1	271.93	-7.69	0.06	3.9	20979	36	15	0.14	0.28	1.56	0.50	0.7	2.4	9.1	3
J084224-545211	2	272.00	-7.73	0.11	1.8	8190	20	17	1.00	0.60	2.11	0.78	4.2	6.3	8.6	1
J084227-553534	1	272.59	-8.17	0.38	2.5	18021	187	116	0.41	0.05	2.57	0.56	3.4	7.0	9.8	1
J084230-551955	1	272.38	-8.00	0.13	2.1	17480	44	20	0.20	0.34	2.22	0.59	2.9	5.1	9.3	1
J084233-544505	2	271.92	-7.64	0.32	1.3	20703	330	312	0.89	0.14	2.60	0.59	4.2	4.4	9.8	1
J084236-552339	1	272.44	-8.03	1.61	2.0	9729	319	286	1.00	0.11	3.28	0.80	13.7	22.7	9.9	1
J084237-552521	1	272.47	-8.04	0.43	2.2	12545	167	119	0.63	0.12	2.70	0.67	4.6	8.4	9.5	1
J084250-544629	2	271.97	-7.62	0.42	1.2	8209	116	85	1.00	0.30	2.70	0.69	9.5	9.8	9.1	1
J084302-552453	1	272.50	-7.99	1.08	2.5	2760	111	96	1.00	0.42	3.01	0.87	12.3	25.8	8.6	1
J084330-545223	2	272.10	-7.61	0.47	1.2	9323	146	93	1.00	0.29	2.77	0.79	9.6	9.8	9.3	1
J084351-545148	2	272.13	-7.56	0.15	1.2	10545	79	19	0.73	0.13	2.28	0.52	4.2	4.2	8.9	2
J084353-542017	2	271.71	-7.24	0.06	1.8	3061	65	21	0.04	0.26	1.71	0.52	1.1	1.8	7.4	2
J084428-543414	2	271.95	-7.31	0.02	1.0	18755	21	15	0.01	0.38	1.46	0.55	1.5	1.3	8.6	3
J084443-545623	2	272.26	-7.51	0.19	1.2	4467	116	71	0.80	0.07	2.34	0.52	4.3	4.4	8.3	2
J084507-545309	2	272.26	-7.43	0.05	1.2	19673	22	20	0.19	0.47	1.80	0.59	2.7	2.8	9.0	2
J084539-550055	2	272.41	-7.45	0.07	1.6	17178	80	62	0.41	0.18	1.82	0.44	1.5	2.0	9.0	1
J084603-544010	2	272.17	-7.19	0.04	1.6	21550	66	38	0.00	0.29	1.67	0.63	1.0	1.4	9.0	3
J084642-542724	2	272.06	-6.99	0.07	2.0	6877	33	23	0.17	0.43	1.71	0.58	1.9	3.1	8.2	2
J084644-545537	2	272.43	-7.27	0.35	1.9	2730	171	136	0.73	0.07	2.45	0.59	4.2	6.8	8.1	2
J084743-545557	2	272.53	-7.17	0.33	3.0	18818	96	82	0.77	0.08	2.27	0.55	3.4	8.4	9.7	1
J084802-542417	2	272.14	-6.80	0.22	4.4	8422	66	48	0.00	0.19	1.87	0.64	1.8	6.7	8.9	1
J084818-542611	2	272.19	-6.79	0.58	4.5	22162	56	29	0.72	0.28	2.33	0.64	5.2	19.6	10.1	2

Atlas of moment-0 maps

Page 1 of the moment-0 maps of the MeerKAT16 galaxy detections. The full atlas is available on Google Drive: https://drive.google.com/drive/folders/16g0frJHkbDKLOB1_2lMqhn5qwqbOxM4X?usp=sharing .

The unique name is in the top-left, the $V_{\rm hel}$ is in the top-right, the beam size is on the bottom-left, and the contour represents 3σ (as measured in the corners of the moment-0 map). The images are in order of RA, going down the left column and then down the right column.

Figure A1: MeerKAT16 Atlas Extract

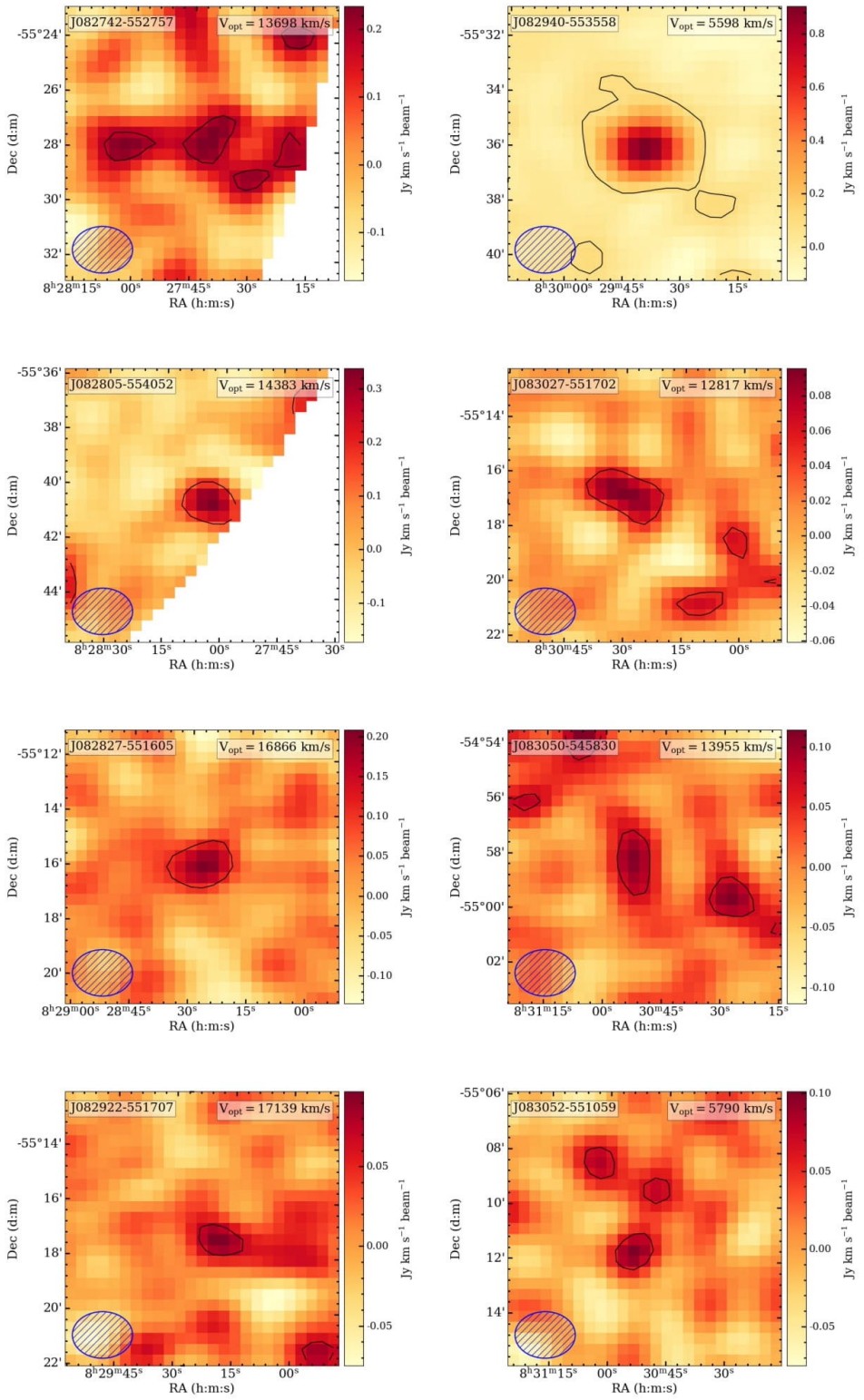

Appendix B

SoFiA Parameters

SoFiA version 2.3.1 parameters used for the GPS source finding:

```
# Global settings
pipeline.verbose = false
pipeline.pedantic = false

# Input
input.data =
/idia/projects/vela/V1_GA_CARACal/output_T19/mosaics/T19_gal.fits
input.region = 1457,5659,355,3959,9,570 #square region of 3x3 deg (slightly different for
different mosaics)
input.gain =
input.noise =
/idia/projects/vela/V1_GA_CARACal/output_T19/mosaics/T19_gal_noise.fits
input.weights =
input.mask =
input.invert = false

# Flagging
flag.region =
flag.auto = false
flag.threshold = 5.0
flag.log = true # Log file listing the spectral channels and spatial pixels flagged by the
auto-flagger

# Noise scaling
scaleNoise.enable = true
scaleNoise.mode = spectral
scaleNoise.gridXY = 0
scaleNoise.gridZ = 0
scaleNoise.interpolate = false
scaleNoise.scfind = true # normalises the noise after each S+C smoothing step
```

```
# S+C finder (smooth & clip)
scfind.enable = true
scfind.kernelsXY = 0, 10, 20, 30
scfind.kernelsZ = 0, 3, 7 #up to x*44.1 500 km/s ; must be odd numbers
scfind.threshold = 3.5 #4.0 # x*sigma sources and above
scfind.replacement = 1.5 # affects how snuggly the mask will fit at the end
scfind.statistic = mad
scfind.fluxRange = negative # this parameter is related to the reliability.

# Linker
linker.radiusXY = 5 # "a bit less than the size of the beam"
linker.radiusZ = 1 # affects when a double horn galaxy starts being defined as two galaxies
linker.minSizeXY = 8 # Paolo: "about the size of the beam" e.g. for 3" pix size & 24" beam
size, beam size = 8 pix
linker.minSizeZ = 2
linker.maxSizeXY = 0
linker.maxSizeZ = 21 #31

# Reliability
reliability.enable = true
reliability.threshold = 0.70
reliability.scaleKernel = 0.25 # Sofia 2.4.0 will use the auto-kernel feature if set to 0
reliability.minSNR = 3 # Replaced reliability.fmin in latest Sofia2 update
reliability.plot = true
reliability.debug = true

# Parameterisation
parameter.enable = true
parameter.wcs = true
parameter.physical = true
parameter.prefix = SoFiA
parameter.offset = true # The position parameters will be relative to the full cube (when
specifying input.region)

# Output
output.directory = /users/nadia/Sofia2/T19 # CHANGE
output.filename = T19 #z_31 #scfind_3.5 # CHANGE
output.writeCatASCII = true
output.writeCatXML = false
output.writeCatSQL = false
output.writeNoise = false
output.writeFiltered = false
output.writeMask = false
```

```
output.writeMask2d = false
output.writeMoments = false # make moment maps
output.writeCubelets = false # small fits cube for each file
output.marginCubelets = 0
output.overwrite = true
```

Figure B1: Global HI profiles of the HIZOA galaxies in the GA-GPS region (blue) versus their GPS counterparts (black). Galaxies are sorted by right ascension and cases with multiples GPS counterparts are marked with '*'.

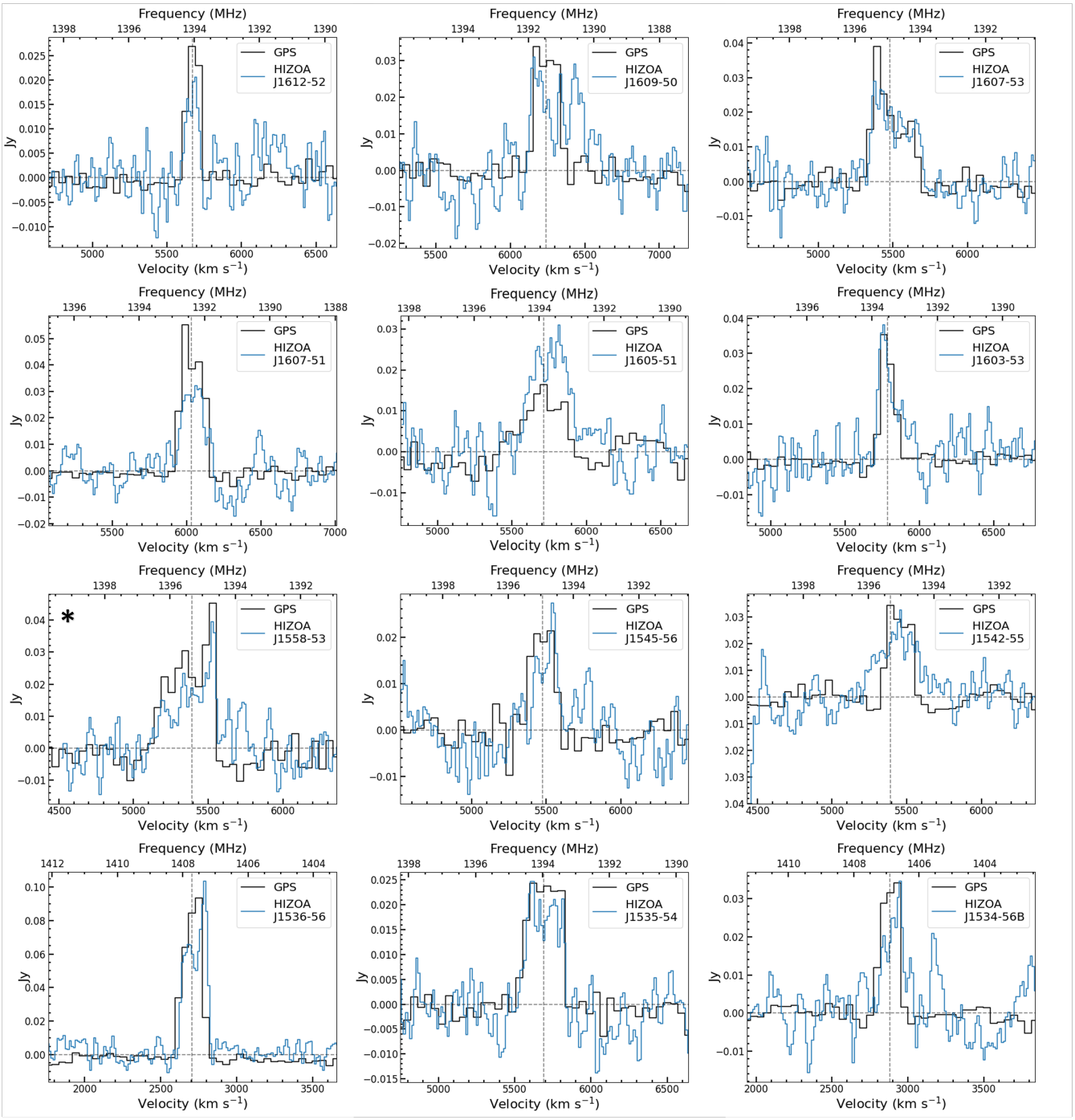

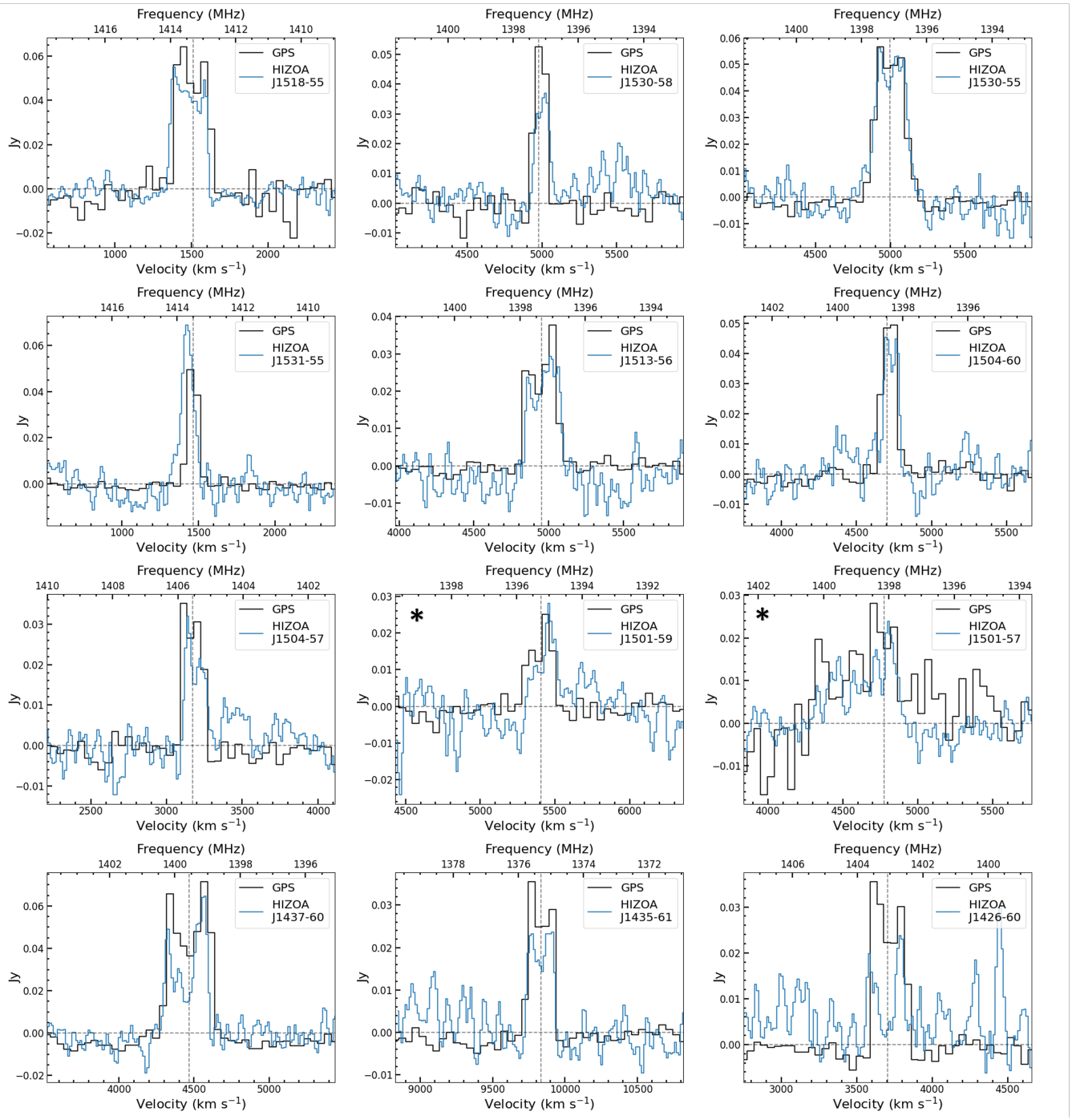
Frequency (MHz)
Velocity (km s^{-1})
Jy
GPS
HIZOA J1518-55
HIZOA J1530-58
HIZOA J1530-55
HIZOA J1531-55
HIZOA J1513-56
HIZOA J1504-60
HIZOA J1504-57
HIZOA J1501-59
HIZOA J1501-57
HIZOA J1437-60
HIZOA J1435-61
HIZOA J1426-60
*


Frequency (MHz)
Jy
Velocity (km s^{-1})
GPS
HIZOA J1425-59
HIZOA J1424-60
HIZOA J1423-59
HIZOA J1421-60
HIZOA J1414-62B*
HIZOA J1404-63
HIZOA J1348-61
HIZOA J1342-61
HIZOA J1331-62
HIZOA J1329-61
HIZOA J1327-61
HIZOA J1320-63

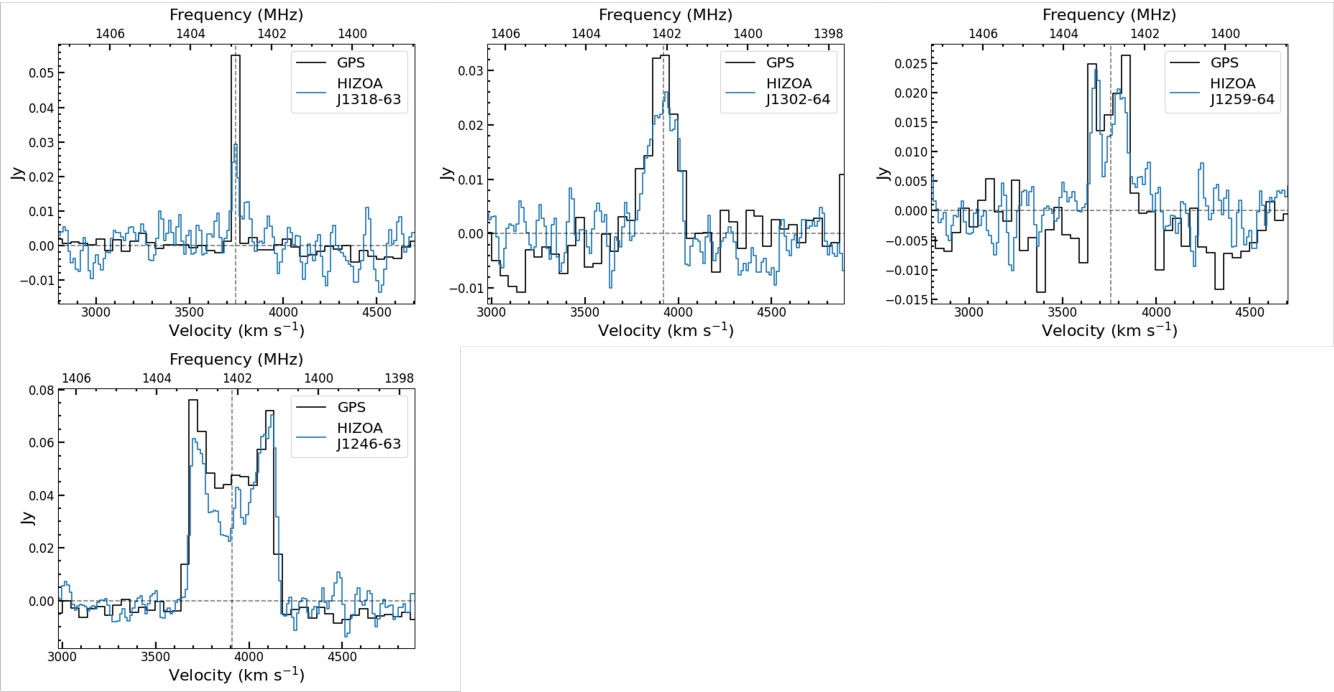
Frequency (MHz)
GPS
HIZOA
J1318-63
Jy
Velocity (km s^{-1})
Frequency (MHz)
GPS
HIZOA
J1302-64
Jy
Velocity (km s^{-1})
Frequency (MHz)
GPS
HIZOA
J1259-64
Jy
Velocity (km s^{-1})
Frequency (MHz)
GPS
HIZOA
J1246-63
Jy
Velocity (km s^{-1})

Figure B2: On-sky distribution of galaxies from GA-GPS (filled circles), and literature (HIZOA & HyperLeda – open circles). The top panel shows the redshift range $14\,500 < V_{\rm hel} < 19\,500\,{\rm km\,s^{-1}}$ and the bottom panel $19\,500 < V_{\rm hel} < 24\,500\,{\rm km\,s^{-1}}$. The black box represents the GA-GPS search area. The grey contour marks a line of equal Galactic foreground extinction ($A_B = 3.0$m).

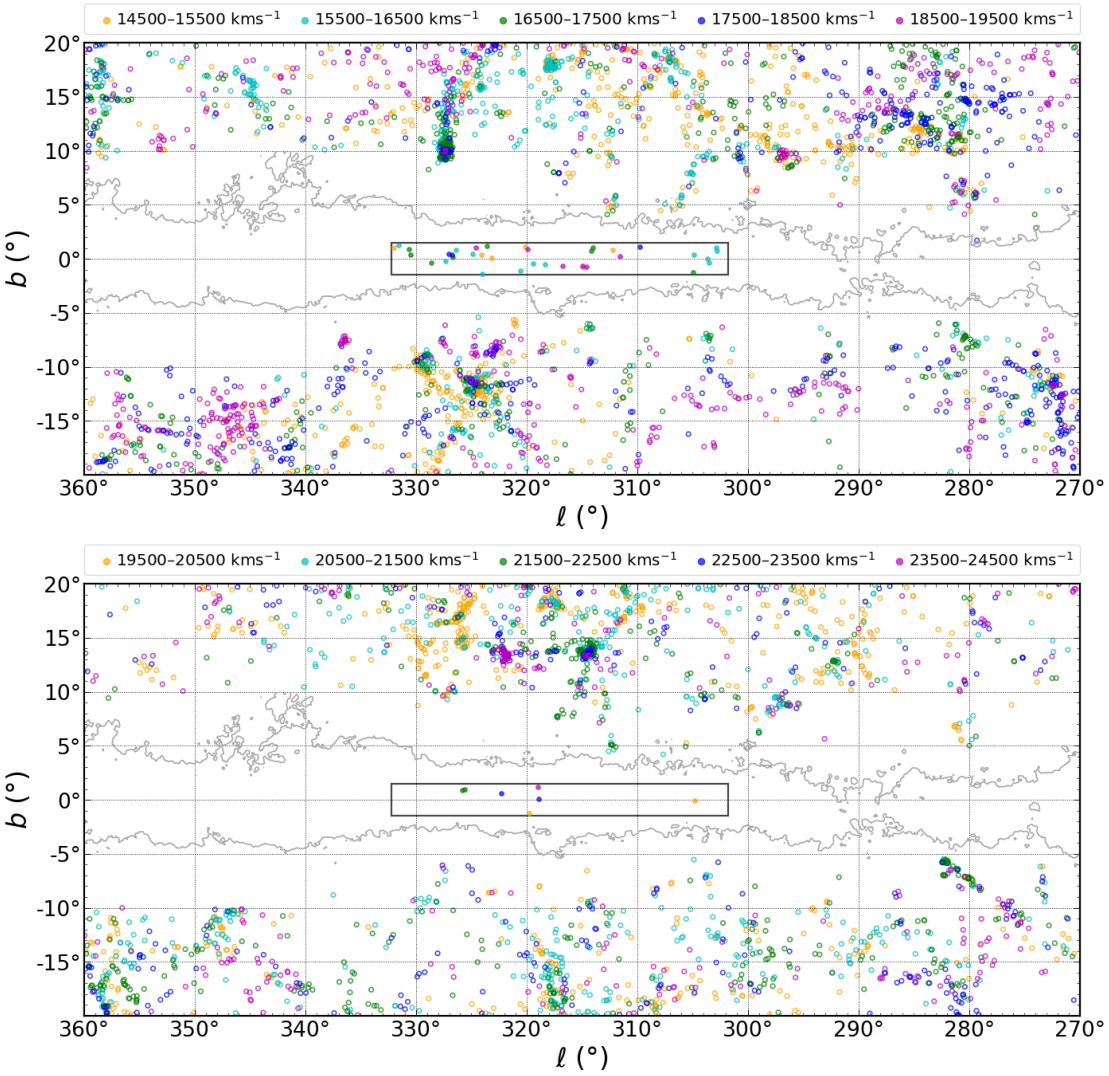

Table B1: The MeerKAT Galactic Plane Legacy Survey: Full Catalog

A brief description of the parameters follows. Parameters are given by SoFiA unless otherwise stated.

– (1) GPS identifier, reflecting the equatorial coordinates [GPS-HI-Jhhmmss ± ddmmss].
– (2) Mosaic [T10 – T19].
– (3) Galactic longitude [deg].
– (4) Galactic latitude [deg].
– (5) Peak flux density – taken from the HI profile [Jy].
– (6) Integrated flux [$\mathrm{Jy\,km\,s^{-1}}$].
– (7) Integrated flux statistical uncertainty [$\mathrm{Jy\,km\,s^{-1}}$].
– (8) Local rms – as measured in the corners of the sub-cube [$\mathrm{Jy\,beam^{-1}}$].
– (9) Heliocentric velocity (optical convention) [$\mathrm{km\,s^{-1}}$].
– (10) Line width at 20% of the peak flux density, measured in the observer's frame [$\mathrm{km\,s^{-1}}$].
– (11) Line width at 50% of the peak flux density, measured in the observer's frame [$\mathrm{km\,s^{-1}}$].
– (12) HI mass – calculated with eq. 2.4 [$\log(M_{\mathrm{HI}}/M_{\odot})$]. HI masses have not been corrected to the barycentre of the Local Group (V_{LG}), nor corrected for the limited instrumental resolution.
– (13) Flag [category 1 (high confidence) or 2 (slightly lower confidence)].
– (14) Note [other name and/or comment].

Footnotes are found at the end of the table.

Table B1: The GA-GPS galaxy catalog.

name J2000 (1)	mosaic TXX (2)	ℓ deg (3)	b deg (4)	$S_{\rm peak}$ Jy (5)	$S_{\rm int}$ Jy km/s (6)	$\mathrm{err}_{S_{\rm int}}$ Jy km/s (7)	rms Jy km/s (8)	$V_{\rm hel}$ km/s (9)	W_{20} km/s (10)	W_{50} km/s (11)	$M_{\rm HI}$ $\log(M_{\rm HI}/M_\odot)$ (12)	flag 1/2 (13)	note
J124141-620158	T19	301.788	0.817	0.008	1.25	0.79	0.33	12051	228	212	9.93	1	
J124160-615621	T19	301.821	0.912	0.008	0.46	0.35	0.33	5817	116	82	8.87	1	
J124342-620018	T19	302.024	0.853	0.005	0.42	0.37	0.29	12042	277	277	9.45	1	
J124404-624235	T19	302.088	0.150	0.006	0.94	0.46	0.26	10920	267	225	9.72	1	
J124431-622415	T19	302.130	0.457	0.010	0.78	0.48	0.29	11780	138	82	9.70	1	
J124532-624150	T19	302.255	0.167	0.010	0.84	0.39	0.26	11828	126	97	9.73	1	
J124624-630308	T19	302.362	-0.186	0.093	30.84	2.39	0.35	3912	489	455	10.35	1	J1246-63
J124734-630933	T19	302.494	-0.291	0.012	1.66	0.62	0.28	10105	266	241	9.90	1	
J124738-640005	T19	302.514	-1.133	0.007	0.68	0.46	0.34	10026	183	183	9.50	1	
J124844-621629	T19	302.618	0.595	0.012	1.95	1.27	0.33	11492	276	248	10.08	1	
J125027-620604	T19	302.816	0.770	0.007	0.92	0.90	0.30	15601	365	341	10.01	2	
J125060-614758	T19	302.880	1.072	0.018	1.12	0.72	0.36	15657	114	75	10.10	1	
J125146-622743	T19	302.970	0.410	0.004	0.51	0.40	0.30	11786	353	328	9.52	1	
J125214-632227	T19	303.021	-0.503	0.007	0.95	0.41	0.25	12876	225	210	9.86	1	
J125248-630837	T19	303.085	-0.272	0.006	0.63	0.32	0.24	12537	231	221	9.66	1	
J125255-631242	T19	303.099	-0.340	0.005	0.68	0.41	0.26	12587	323	292	9.70	1	
J125400-625346	T19	303.224	-0.026	0.002	0.11	0.14	0.23	12934	133	108	8.94	1	
J125446-640154	T19	303.296	-1.162	0.007	0.31	0.28	0.30	10116	92	76	9.17	1	
J125500-630545	T19	303.335	-0.227	0.009	0.97	0.45	0.27	10071	183	183	9.66	1	
J125625-631226	T19	303.493	-0.341	0.006	1.05	0.51	0.27	15920	326	302	10.09	1	
J125701-624842	T19	303.568	0.053	0.010	1.60	0.88	0.30	12929	259	225	10.09	1	
J125729-625317	T19	303.621	-0.025	0.004	0.27	0.27	0.27	15910	137	121	9.50	1	
J125841-620529	T19	303.780	0.768	0.011	0.81	0.52	0.32	9844	86	71	9.56	1	
J125907-641822	T19	303.765	-1.447	0.025	3.86	1.60	0.71	3756	215	200	9.41	1	J1259-64
J125932-635841	T19	303.819	-1.120	0.014	1.33	0.54	0.34	3912	135	117	8.99	1	
J125937-624059	T19	303.870	0.174	0.009	0.65	0.53	0.30	10535	128	109	9.52	1	
J130033-625813	T19	303.967	-0.117	0.007	0.47	0.31	0.27	10105	127	112	9.35	1	
J130211-640338	T19	304.107	-1.213	0.021	2.64	1.09	0.36	3917	253	223	9.28	1	J1302-64
J130219-621523	T19	304.197	0.589	0.009	1.19	0.78	0.36	13789	311	133	10.02	1	
J130235-640621	T19	304.148	-1.260	0.017	1.61	0.91	0.37	3923	157	101	9.07	1	J1302-64
J130247-614827	T19	304.272	1.035	0.007	0.95	0.96	0.35	13738	330	280	9.92	1	
J130804-625122	T18	304.827	-0.046	0.007	1.05	0.80	0.44	19820	414	329	10.27	2	
J130804-622610	T18	304.855	0.373	0.006	0.13	0.24	0.43	15894	83	53	9.18	2	
J130833-630248	T18	304.870	-0.239	0.007	1.01	0.71	0.48	12131	231	231	9.84	1	
J130932-640405	T18	304.908	-1.266	0.015	1.17	1.41	0.52	16626	421	161	10.17	2	group[1]
J131002-612302	T18	305.157	1.408	0.012	0.56	0.33	0.43	3904	45	45	8.61	1	
J131053-635201	T19	305.071	-1.076	0.005	0.23	0.41	0.37	12271	92	86	9.21	2	
J131127-634643	T18	305.141	-0.993	0.010	1.17	0.89	0.39	7822	270	254	9.53	1	
J131202-634757	T18	305.204	-1.018	0.024	3.41	1.69	0.41	7711	220	170	9.98	1	
J131319-631846	T18	305.386	-0.545	0.005	0.51	0.48	0.44	12136	171	138	9.54	1	
J131435-632335	T18	305.521	-0.638	0.008	1.12	0.90	0.43	12298	442	359	9.89	2	
J131744-633015	T18	305.861	-0.782	0.055	2.33	0.83	0.45	3750	72	45	9.19	1	J1318-63
J131924-635630	T18	305.997	-1.236	0.014	1.22	0.85	0.42	12729	225	188	9.96	1	
J132005-631728	T18	306.145	-0.598	0.006	0.43	0.44	0.32	24852	231	145	10.07	2	
J132011-631618	T18	306.157	-0.580	0.036	6.03	1.86	0.46	3743	236	151	9.60	1	J1320-63
J132158-621724	T18	306.473	0.372	0.010	0.34	0.30	0.34	9690	46	29	9.18	1	
J132322-620858	T18	306.651	0.491	0.006	0.17	0.22	0.32	2392	36	22	7.68	2	possible dwarf
J132407-623712	T18	306.679	0.014	0.010	3.05	1.75	0.38	6609	492	456	9.80	1	
J132532-621306	T18	306.894	0.391	0.008	1.16	0.79	0.35	6567	453	450	9.37	1	
J132642-613202	T18	307.121	1.051	0.029	7.29	1.57	0.35	6503	307	287	10.16	1	J1327-61

GA-GPS galaxy catalog continued

name J2000 (1)	mosaic TXX (2)	ℓ deg (3)	b deg (4)	$S_{\rm peak}$ Jy (5)	$S_{\rm int}$ Jy km/s (6)	$\mathrm{err}_{S_{\rm int}}$ Jy km/s (7)	rms Jy km/s (8)	$V_{\rm hel}$ km/s (9)	W_{20} km/s (10)	W_{50} km/s (11)	$M_{\rm HI}$ $\log(M_{\rm HI}/M_\odot)$ (12)	flag 1/2 (13)	note
J132652-620544	T18	307.065	0.491	0.020	1.28	0.51	0.35	3733	45	45	8.93	1	
J132659-625456	T18	306.965	-0.322	0.014	0.96	0.72	0.34	6609	121	84	9.30	1	
J132836-632540	T18	307.074	-0.855	0.009	0.28	0.29	0.31	2437	36	22	7.90	2	
J132934-635331	T18	307.112	-1.330	0.033	1.69	0.68	0.46	2383	81	54	8.66	1	
J133002-615146	T18	307.465	0.669	0.087	15.62	2.25	0.39	3696	253	222	10.01	1	J1329-61
J133202-620407	T18	307.667	0.429	0.028	1.57	0.62	0.36	7152	88	55	9.58	1	J1331-62
J133415-631618	T18	307.724	-0.799	0.005	0.47	0.29	0.28	12709	185	167	9.54	1	
J133736-631519	T18	308.098	-0.847	0.007	0.48	0.28	0.25	9932	92	80	9.35	1	
J134019-615716	T17	308.643	0.374	0.023	2.03	1.34	0.53	7516	91	88	9.73	1	
J134043-610942	T17	308.841	1.143	0.012	1.39	1.08	0.55	3672	193	130	8.95	1	
J134129-622316	T17	308.694	-0.077	0.010	0.43	0.39	0.42	3767	45	45	8.46	1	
J134158-613945	T17	308.890	0.623	0.010	0.61	0.51	0.44	3772	129	81	8.62	1	
J134227-610114	T17	309.072	1.242	0.076	23.92	7.17	0.68	3964	391	326	10.25	1	J1342-61[2]
J134309-605759	T17	309.167	1.278	0.021	0.87	0.80	0.60	4030	73	46	8.83	1	
J134319-625119	T17	308.810	-0.577	0.008	0.60	0.33	0.28	12642	92	92	9.64	1	
J134831-605751	T17	309.804	1.144	0.012	1.45	1.35	0.64	17605	250	104	10.31	2	
J134849-615619	T17	309.625	0.185	0.054	3.61	1.55	0.54	4073	108	65	9.45	1	J1348-61
J135335-610333	T17	310.380	0.911	0.017	1.80	1.59	0.55	8005	168	130	9.73	2	
J135639-610312	T17	310.741	0.826	0.025	4.55	1.67	0.47	3811	223	181	9.50	1	
J135753-610405	T16	310.883	0.774	0.015	2.42	1.70	0.45	8449	390	343	9.91	2	
J135831-610248	T16	310.962	0.775	0.010	1.70	1.13	0.38	8565	274	239	9.77	1	
J135911-605931	T16	311.054	0.807	0.014	1.02	0.53	0.35	5915	90	73	9.23	1	
J135922-611215	T16	311.020	0.596	0.010	0.91	0.55	0.41	8014	176	158	9.44	1	
J135930-610330	T16	311.074	0.733	0.010	0.65	0.55	0.40	3971	90	81	8.68	1	
J140130-604917	T16	311.371	0.897	0.008	0.59	0.36	0.37	5501	90	78	8.93	1	
J140144-623126	T16	310.940	-0.750	0.012	1.39	0.75	0.44	7137	136	136	9.52	1	
J140147-615220	T16	311.121	-0.124	0.008	0.86	0.96	0.53	9968	280	216	9.60	2	
J140259-602854	T16	311.637	1.175	0.008	0.80	0.68	0.55	9394	320	320	9.52	1	
J140316-605941	T16	311.530	0.672	0.007	1.06	0.51	0.39	8741	228	202	9.58	1	
J140320-610558	T16	311.509	0.569	0.008	0.56	0.46	0.40	5529	135	74	8.91	1	
J140325-605235	T16	311.581	0.781	0.009	0.65	0.58	0.40	5933	136	112	9.03	1	
J140413-603211	T16	311.769	1.081	0.010	0.72	0.51	0.43	8145	182	182	9.35	1	
J140445-631057	T16	311.090	-1.478	0.021	4.60	2.25	0.96	7951	273	273	10.13	1	J1404-63
J140449-612305	T16	311.601	0.246	0.006	0.73	0.60	0.46	19228	215	178	10.08	1	
J140454-611442	T16	311.649	0.377	0.017	1.73	0.95	0.48	8339	171	148	9.75	1	
J140537-601402	T16	312.019	1.322	0.009	0.74	0.48	0.46	9427	183	164	9.49	1	
J140614-603014	T16	312.016	1.042	0.009	0.74	0.45	0.34	11022	223	196	9.62	1	
J140620-603229	T16	312.016	1.003	0.005	0.27	0.22	0.30	11538	92	74	9.22	1	
J140807-603938	T16	312.192	0.825	0.005	0.49	0.41	0.35	14623	232	214	9.68	1	
J141057-602613	T16	312.591	0.935	0.011	0.62	0.40	0.36	14418	85	70	9.77	1	
J141151-613818	T16	312.328	-0.242	0.007	0.91	0.73	0.46	11349	300	227	9.74	1	
J141224-612258	T16	312.470	-0.019	0.006	0.56	0.59	0.47	14177	232	232	9.71	1	
J141249-621625	T16	312.242	-0.882	0.013	1.30	0.93	0.46	3102	169	147	8.78	1	
J141330-612227	T16	312.597	-0.052	0.010	0.46	0.42	0.44	8386	46	46	9.18	1	
J141333-600959	T16	312.980	1.094	0.011	0.94	0.50	0.33	3657	90	90	8.77	1	
J141425-605213	T16	312.861	0.392	0.010	0.82	0.62	0.43	11279	184	160	9.68	1	
J141426-600124	T16	313.129	1.195	0.012	0.55	0.40	0.36	13632	46	46	9.67	1	
J141427-622556	T16	312.372	-1.092	0.019	0.95	0.65	0.51	3352	84	68	8.71	1	
J141435-612420	T16	312.712	-0.123	0.016	2.23	1.51	0.50	8134	291	195	9.84	2	
J141444-613640	T16	312.663	-0.323	0.010	1.10	0.99	0.48	11531	248	168	9.83	2	

GA-GPS galaxy catalog continued

name J2000 (1)	mosaic TXX (2)	ℓ deg (3)	b deg (4)	$S_{\rm peak}$ Jy (5)	$S_{\rm int}$ Jy km/s (6)	$\mathrm{err}_{S_{\rm int}}$ Jy km/s (7)	rms Jy km/s (8)	$V_{\rm hel}$ km/s (9)	W_{20} km/s (10)	W_{50} km/s (11)	$M_{\rm HI}$ $\log(M_{\rm HI}/M_\odot)$ (12)	flag 1/2 (13)	note
J141503-610757	T16	312.850	0.119	0.013	1.55	1.07	0.43	12876	247	150	10.07	1	
J141503-603143	T16	313.043	0.691	0.016	3.04	1.20	0.37	11017	554	417	10.23	1	
J141521-621113	T16	312.548	-0.892	0.027	4.33	1.12	0.50	3285	204	174	9.35	1	J1414-62B*
J141557-623832	T16	312.469	-1.346	0.026	1.10	0.95	0.80	3445	45	39	8.79	1	
J141652-615941	T16	312.779	-0.767	0.009	0.79	0.49	0.41	8562	159	120	9.43	1	
J141835-612830	T16	313.141	-0.343	0.006	0.12	0.30	0.37	11832	289	210	8.90	2	
J141846-603302	T16	313.467	0.523	0.007	0.48	0.32	0.30	10056	183	155	9.36	1	
J141931-601920	T16	313.630	0.707	0.017	1.45	0.51	0.33	10636	92	92	9.88	1	
J142001-594727	T15	313.867	1.187	0.007	0.46	0.35	0.36	10489	92	92	9.37	1	
J142103-595703	T15	313.936	0.993	0.013	1.45	0.54	0.31	5302	180	155	9.29	1	
J142109-595153	T15	313.977	1.069	0.007	0.14	0.16	0.27	17381	84	52	9.28	1	
J142111-600236	T15	313.920	0.900	0.005	0.23	0.19	0.27	10859	92	92	9.10	1	
J142120-602328	T15	313.820	0.566	0.028	5.57	1.07	0.36	3891	269	269	9.60	1	J1421-60
J142139-604552	T16	313.729	0.202	0.006	0.44	0.32	0.30	14493	186	186	9.63	1	
J142209-614849	T16	313.425	-0.804	0.027	1.94	0.80	0.40	3423	90	76	9.03	1	
J142239-600634	T15	314.070	0.775	0.016	0.99	0.44	0.32	5604	45	45	9.17	1	
J142320-595138	T15	314.236	0.979	0.040	11.99	1.78	0.36	5650	565	529	10.26	1	J1423-59
J142345-600755	T15	314.190	0.706	0.004	0.36	0.31	0.27	17388	375	359	9.69	2	
J142357-602412	T15	314.118	0.444	0.019	1.28	0.74	0.40	8487	121	88	9.63	1	
J142415-603102	T15	314.113	0.324	0.006	0.60	0.39	0.30	14488	269	224	9.76	1	
J142446-603711	T15	314.137	0.205	0.010	0.63	0.42	0.34	10589	127	111	9.52	1	
J142448-594049	T15	314.471	1.084	0.018	3.06	0.85	0.40	8326	273	273	10.00	1	J1425-59
J142504-602434	T15	314.246	0.389	0.013	0.50	0.29	0.33	4390	37	23	8.66	2	
J142510-600550	T15	314.367	0.677	0.032	4.95	0.87	0.33	4142	222	198	9.61	1	J1424-60
J142547-605013	T15	314.176	-0.042	0.011	0.90	0.43	0.34	4286	90	84	8.90	1	
J142551-604323	T15	314.223	0.062	0.029	2.24	0.76	0.38	4314	127	89	9.30	1	
J142554-602916	T15	314.313	0.280	0.007	0.17	0.19	0.32	8525	46	46	8.77	1	
J142600-614812	T15	313.855	-0.954	0.008	1.15	0.56	0.36	8659	274	259	9.60	1	
J142621-601356	T15	314.458	0.498	0.037	6.82	0.97	0.34	3711	224	213	9.65	1	J1426-60
J142720-600942	T15	314.597	0.520	0.008	0.80	0.37	0.28	5457	135	121	9.05	1	
J142739-612022	T15	314.206	-0.592	0.010	1.20	0.47	0.31	8252	228	195	9.58	1	
J142845-611259	T15	314.373	-0.525	0.017	1.78	0.76	0.34	9304	183	183	9.86	1	
J142934-613043	T15	314.356	-0.836	0.004	0.26	0.27	0.28	14411	325	325	9.39	1	
J143036-610716	T15	314.616	-0.519	0.007	0.40	0.40	0.32	9037	109	69	9.19	2	
J143042-605733	T15	314.688	-0.373	0.011	1.34	0.74	0.34	10464	265	249	9.83	1	
J143107-611941	T15	314.596	-0.735	0.011	1.51	0.64	0.31	19118	283	268	10.40	1	
J143131-611207	T15	314.689	-0.636	0.014	2.59	0.68	0.31	9448	274	274	10.03	1	
J143313-604541	T15	315.047	-0.306	0.010	0.30	0.23	0.30	10485	83	52	9.19	1	
J143327-594404	T15	315.466	0.631	0.007	0.43	0.31	0.30	8346	137	137	9.15	1	
J143329-611930	T15	314.859	-0.839	0.004	0.11	0.13	0.26	14630	93	76	9.04	1	
J143332-610746	T15	314.941	-0.661	0.010	0.50	0.34	0.29	18958	47	47	9.91	1	
J143347-601128	T15	315.329	0.194	0.005	0.30	0.30	0.32	5534	181	181	8.64	1	
J143427-594240	T15	315.592	0.604	0.007	0.54	0.30	0.28	12743	92	92	9.61	1	
J143505-611315	T15	315.077	-0.817	0.033	4.68	0.91	0.34	9839	179	164	10.32	1	J1435-61
J143520-585617	T15	315.995	1.273	0.006	0.34	0.27	0.34	14096	128	112	9.49	1	
J143551-605214	T15	315.299	-0.531	0.015	1.29	0.55	0.32	4525	155	107	9.10	1	
J143724-595045	T15	315.881	0.335	0.004	0.12	0.16	0.29	5035	82	52	8.15	2	
J143759-602534	T15	315.716	-0.226	0.078	17.87	2.40	0.42	4471	341	305	10.23	1	J1437-60
J143826-593730	T15	316.087	0.486	0.006	0.21	0.28	0.33	4954	90	66	8.40	1	
J143911-592916	T15	316.230	0.573	0.009	0.34	0.35	0.35	4434	110	60	8.51	1	

GA-GPS galaxy catalog continued

name J2000 (1)	mosaic TXX (2)	ℓ deg (3)	b deg (4)	$S_{\rm peak}$ Jy (5)	$S_{\rm int}$ Jy km/s (6)	$\mathrm{err}_{S_{\rm int}}$ Jy km/s (7)	rms Jy km/s (8)	$V_{\rm hel}$ km/s (9)	W_{20} km/s (10)	W_{50} km/s (11)	$M_{\rm HI}$ $\log(M_{\rm HI}/M_\odot)$ (12)	flag 1/2 (13)	note
J143913-593419	T15	316.200	0.494	0.005	0.16	0.18	0.30	5418	123	83	8.35	1	
J143940-604606	T15	315.766	-0.622	0.018	0.84	0.43	0.34	4582	82	59	8.92	1	
J144023-595745	T15	316.175	0.078	0.007	0.16	0.22	0.35	5632	75	47	8.38	2	
J144108-584315	T14	316.770	1.172	0.012	3.31	1.16	0.50	4963	525	497	9.59	1	
J144110-603922	T15	315.980	-0.595	0.010	0.42	0.30	0.32	4362	45	45	8.58	1	
J144119-594648	T15	316.357	0.197	0.016	2.71	1.04	0.44	9088	294	244	10.02	1	
J144151-591330	T15	316.646	0.675	0.015	1.47	0.98	0.40	4066	176	132	9.06	1	
J144153-591231	T15	316.657	0.688	0.022	3.40	2.16	0.43	4116	334	245	9.44	2	two sources?
J144155-591056	T15	316.672	0.710	0.012	0.63	0.69	0.38	4218	124	87	8.73	1	
J144210-605933	T15	315.953	-0.952	0.007	0.98	0.66	0.35	10553	448	428	9.71	1	
J144228-602503	T15	316.224	-0.443	0.015	2.32	0.85	0.40	10643	267	253	10.09	1	
J144236-582527	T14	317.067	1.363	0.010	0.22	0.28	0.46	10908	46	29	9.08	2	
J144249-602252	T15	316.279	-0.428	0.010	1.39	0.92	0.40	5610	216	176	9.31	1	
J144254-593444	T15	316.622	0.297	0.005	0.39	0.38	0.38	4155	160	124	8.50	2	
J144308-595142	T15	316.531	0.028	0.005	0.36	0.49	0.39	14256	223	185	9.52	2	
J144321-593460	T15	316.672	0.270	0.003	0.14	0.20	0.34	13078	93	93	9.05	2	
J144348-594514	T15	316.653	0.090	0.006	0.31	0.34	0.41	5523	90	84	8.66	1	
J144423-610551	T15	316.154	-1.159	0.011	0.61	0.41	0.36	10476	92	77	9.49	1	
J144608-584238	T14	317.364	0.910	0.008	0.23	0.23	0.35	4112	38	24	8.27	2	
J144643-602239	T15	316.718	-0.629	0.004	0.40	0.40	0.36	18503	217	185	9.79	2	
J144656-591332	T14	317.237	0.400	0.014	2.08	1.10	0.46	11231	304	148	10.08	1	two sources?
J144659-611545	T15	316.367	-1.442	0.015	0.83	0.73	0.74	5766	176	142	9.11	1	
J144745-601709	T14	316.872	-0.601	0.024	7.31	1.63	0.43	4484	397	383	9.84	1	GLIMPSEG2
J144758-575741	T14	317.903	1.483	0.011	0.30	0.33	0.60	4647	45	45	8.49	1	
J144835-605320	T15	316.703	-1.189	0.009	0.83	0.66	0.42	14071	325	288	9.88	1	
J144837-600719	T14	317.040	-0.500	0.017	3.69	1.13	0.40	4542	427	381	9.56	1	GLIMPSEG1
J145003-591445	T14	317.587	0.208	0.018	0.93	0.75	0.43	3244	110	62	8.67	2	
J145028-600005	T14	317.301	-0.493	0.020	5.05	1.15	0.39	5361	442	423	9.84	1	
J145043-591550	T14	317.656	0.154	0.014	1.06	0.53	0.39	3240	90	85	8.72	1	
J145116-604726	T14	317.040	-1.244	0.008	0.34	0.30	0.34	11828	122	92	9.34	1	
J145135-594435	T14	317.540	-0.323	0.003	0.21	0.23	0.33	11001	225	201	9.07	1	
J145227-592145	T14	317.808	-0.032	0.004	0.15	0.21	0.35	11031	46	46	8.92	2	
J145255-600846	T14	317.510	-0.759	0.038	8.31	1.08	0.39	4288	261	239	9.86	1	
J145258-594260	T14	317.708	-0.378	0.004	0.11	0.15	0.32	4636	45	45	8.05	1	
J145326-592834	T14	317.869	-0.190	0.007	0.34	0.36	0.38	11026	184	173	9.29	1	
J145407-592406	T14	317.980	-0.162	0.009	0.65	0.49	0.38	4255	134	104	8.75	1	
J145445-595906	T14	317.787	-0.719	0.005	0.44	0.38	0.32	5420	354	339	8.79	1	
J145451-604438	T14	317.452	-1.400	0.021	1.84	1.42	0.76	5249	180	180	9.38	1	
J145532-583339	T14	318.527	0.502	0.036	5.03	1.39	0.35	4706	298	101	9.72	1	
J145540-582735	T14	318.589	0.584	0.008	0.73	0.54	0.33	11627	220	188	9.66	1	
J145551-573053	T14	319.045	1.412	0.010	0.70	0.54	0.54	4880	169	77	8.90	1	
J145552-583350	T14	318.565	0.479	0.011	0.76	0.38	0.34	5970	45	45	9.10	1	
J145558-600531	T14	317.873	-0.883	0.054	4.41	0.76	0.35	4468	122	86	9.62	1	
J145617-574540	T14	318.983	1.166	0.008	0.25	0.26	0.33	23852	86	69	9.79	1	
J145725-584745	T14	318.635	0.181	0.014	1.46	0.58	0.34	6351	136	119	9.44	1	
J145731-593252	T14	318.297	-0.491	0.007	0.71	0.57	0.31	15824	233	210	9.91	1	
J145846-601546	T14	318.102	-1.196	0.009	0.84	0.47	0.39	4366	135	135	8.88	1	
J145853-582347	T14	318.991	0.444	0.007	0.31	0.30	0.32	13320	231	84	9.41	1	
J145945-584317	T14	318.937	0.105	0.011	0.35	0.32	0.33	23263	48	35	9.93	2	
J145949-581438	T14	319.171	0.521	0.023	1.29	0.54	0.36	13962	86	71	10.06	1	

GA-GPS galaxy catalog continued

name J2000 (1)	mosaic TXX (2)	ℓ deg (3)	b deg (4)	$S_{\rm peak}$ Jy (5)	$S_{\rm int}$ Jy km/s (6)	$\mathrm{err}_{S_{\rm int}}$ Jy km/s (7)	rms Jy km/s (8)	$V_{\rm hel}$ km/s (9)	W_{20} km/s (10)	W_{50} km/s (11)	$M_{\rm HI}$ $\log(M_{\rm HI}/M_\odot)$ (12)	flag 1/2 (13)	note
J150020-580251	T14	319.324	0.662	0.012	1.16	0.60	0.35	4649	168	93	9.08	1	
J150048-592024	T14	318.763	-0.504	0.008	0.70	0.37	0.33	5545	111	81	9.01	1	
J150115-572336	T13	319.744	1.179	0.020	6.10	2.65	0.50	4629	474	425	9.79	1	J1501-57 A
J150138-593023	T14	318.777	-0.701	0.005	0.16	0.19	0.28	5411	134	118	8.36	1	J1501-59 B
J150145-590347	T14	319.002	-0.319	0.009	0.68	0.40	0.32	5273	169	142	8.95	1	
J150150-572144	T13	319.828	1.168	0.009	0.48	0.46	0.41	4756	135	102	8.71	1	J1501-57 B
J150160-581343	T14	319.430	0.398	0.006	0.41	0.35	0.32	11828	138	113	9.42	1	
J150206-595406	T14	318.640	-1.076	0.004	0.37	0.33	0.34	12598	323	317	9.43	1	
J150209-592728	T14	318.858	-0.690	0.005	0.14	0.14	0.27	4162	37	23	8.06	2	
J150214-593405	T14	318.813	-0.791	0.011	1.21	0.60	0.33	5396	180	156	9.22	1	J1501-59 A
J150234-574631	T13	319.715	0.759	0.008	0.74	0.73	0.37	5790	181	146	9.07	1	
J150245-592632	T14	318.933	-0.713	0.009	0.43	0.28	0.31	5459	45	45	8.79	1	J1501-59 C
J150248-591258	T14	319.047	-0.518	0.006	0.21	0.24	0.30	11565	127	78	9.12	1	
J150304-572718	T14	319.928	1.007	0.004	0.14	0.18	0.31	4599	45	45	8.14	2	
J150320-573416	T13	319.904	0.888	0.006	0.77	0.49	0.34	18736	377	377	10.09	1	
J150345-571615	T14	320.098	1.124	0.005	0.20	0.25	0.36	14885	93	75	9.31	1	
J150406-590147	T14	319.282	-0.435	0.006	0.31	0.26	0.32	13005	89	62	9.39	1	
J150423-573757	T13	319.996	0.767	0.006	0.18	0.22	0.33	11992	46	46	9.07	1	
J150441-600535	T14	318.829	-1.400	0.054	4.66	1.51	0.60	4719	90	85	9.69	1	J1504-60
J150444-571309	T13	320.238	1.105	0.034	4.48	0.96	0.47	3173	134	134	9.33	1	J1504-57
J150451-590810	T14	319.314	-0.575	0.004	0.38	0.36	0.32	14237	279	246	9.54	1	
J150503-585842	T14	319.416	-0.451	0.005	0.30	0.24	0.29	16213	93	78	9.56	1	
J150554-583101	T13	319.738	-0.103	0.004	0.13	0.19	0.32	5229	81	68	8.21	1	
J150609-581012	T13	319.937	0.183	0.008	0.96	0.66	0.39	11997	225	187	9.81	1	
J150716-571931	T13	320.486	0.843	0.007	0.22	0.27	0.36	8672	125	82	8.89	1	
J150721-571817	T13	320.506	0.855	0.004	0.18	0.23	0.33	11486	92	84	9.05	1	
J150856-594552	T14	319.454	-1.379	0.015	0.66	0.71	0.72	4205	90	90	8.74	1	
J150857-573460	T13	320.553	0.506	0.027	3.95	1.28	0.43	5004	171	156	9.67	1	
J150901-572231	T13	320.665	0.681	0.012	0.78	0.47	0.39	11659	46	46	9.69	1	
J150913-580509	T13	320.330	0.054	0.017	1.77	0.99	0.47	5503	181	181	9.40	1	
J150919-564815	T13	320.986	1.155	0.019	0.75	0.45	0.40	4943	44	28	8.94	1	
J150921-581826	T13	320.235	-0.147	0.012	1.45	0.85	0.44	6390	192	134	9.45	1	
J150944-573852	T13	320.611	0.397	0.012	0.53	0.45	0.37	14061	46	46	9.68	2	
J151000-574844	T13	320.558	0.238	0.005	0.33	0.40	0.39	14108	158	80	9.48	2	
J151005-573635	T13	320.670	0.407	0.008	0.27	0.28	0.34	5849	82	51	8.63	1	
J151032-593156	T13	319.746	-1.280	0.007	0.21	0.36	0.52	20149	176	26	9.58	2	
J151035-581232	T13	320.424	-0.144	0.006	0.50	0.65	0.42	8234	216	179	9.20	2	
J151056-583150	T13	320.300	-0.444	0.003	0.24	0.32	0.37	12051	231	106	9.21	2	
J151058-574513	T13	320.699	0.222	0.011	1.03	1.01	0.47	13320	231	231	9.93	2	
J151112-565432	T13	321.156	0.934	0.007	0.31	0.28	0.33	8708	86	71	9.04	1	
J151120-572808	T13	320.886	0.443	0.008	0.33	0.34	0.37	4823	81	64	8.56	1	
J151122-575916	T13	320.625	-0.006	0.013	1.89	1.06	0.42	10415	319	228	9.98	1	
J151129-573716	T13	320.825	0.302	0.006	0.65	0.75	0.38	11921	323	323	9.63	1	
J151137-565952	T13	321.160	0.828	0.005	0.14	0.19	0.34	11506	184	166	8.94	1	
J151203-580238	T13	320.674	-0.100	0.005	0.54	0.59	0.39	12943	296	192	9.62	1	
J151212-584501	T13	320.328	-0.717	0.018	2.52	0.96	0.46	8150	137	137	9.89	1	
J151213-573919	T13	320.892	0.222	0.012	1.26	0.60	0.37	4935	177	139	9.16	1	
J151245-573906	T13	320.955	0.189	0.018	2.33	0.89	0.41	4911	211	180	9.42	1	
J151249-583555	T13	320.476	-0.628	0.022	4.44	1.32	0.45	4970	326	281	9.71	1	
J151252-575049	T13	320.868	0.013	0.005	0.19	0.20	0.33	5260	90	83	8.40	1	

GA-GPS galaxy catalog continued

name J2000 (1)	mosaic TXX (2)	ℓ deg (3)	b deg (4)	$S_{\rm peak}$ Jy (5)	$S_{\rm int}$ Jy km/s (6)	$\mathrm{err}_{S_{\rm int}}$ Jy km/s (7)	rms Jy km/s (8)	$V_{\rm hel}$ km/s (9)	W_{20} km/s (10)	W_{50} km/s (11)	$M_{\rm HI}$ $\log(M_{\rm HI}/M_\odot)$ (12)	flag 1/2 (13)	note
J151311-571959	T13	321.170	0.431	0.009	1.09	0.51	0.35	4959	211	181	9.10	1	
J151326-574900	T13	320.948	0.001	0.013	0.85	0.43	0.36	3050	83	69	8.58	1	
J151331-582633	T13	320.635	-0.542	0.015	0.84	0.58	0.42	11994	108	61	9.75	1	
J151331-581515	T13	320.733	-0.380	0.019	1.26	0.62	0.43	5420	45	45	9.24	1	
J151349-570119	T13	321.404	0.654	0.021	1.19	0.54	0.35	4939	90	60	9.14	1	
J151350-582552	T13	320.676	-0.553	0.016	1.90	0.99	0.45	6232	207	115	9.54	1	
J151356-564906	T13	321.524	0.819	0.038	6.01	1.22	0.41	4956	256	219	9.84	1	J1513-56
J151401-583936	T13	320.578	-0.762	0.007	0.86	0.61	0.42	11894	217	175	9.75	1	
J151406-564053	T13	321.614	0.924	0.012	1.09	0.61	0.40	6137	127	112	9.29	1	
J151420-581116	T13	320.858	-0.379	0.005	1.03	0.82	0.42	12807	578	476	9.89	1	
J151420-575459	T13	321.000	-0.148	0.009	0.38	0.37	0.37	4782	45	45	8.62	1	
J151421-560748	T13	321.930	1.378	0.009	0.42	0.47	0.58	5284	135	112	8.74	1	
J151422-572855	T13	321.229	0.221	0.008	0.64	0.64	0.38	10399	239	185	9.51	1	
J151426-565935	T13	321.490	0.635	0.006	0.26	0.26	0.26	4906	122	93	8.48	1	
J151427-585911	T13	320.457	-1.069	0.016	0.46	0.88	0.59	12070	81	50	9.49	1	
J151451-573517	T13	321.228	0.098	0.008	0.32	0.30	0.35	5315	62	33	8.64	1	
J151458-582906	T13	320.775	-0.676	0.010	0.69	0.55	0.41	13214	93	93	9.74	1	
J151513-585626	T13	320.565	-1.082	0.009	0.47	0.64	0.52	16316	176	103	9.76	2	
J151531-565924	T13	321.618	0.560	0.008	0.44	0.38	0.34	7172	135	103	9.02	1	
J151556-575060	T13	321.215	-0.201	0.017	0.82	0.59	0.40	5391	81	52	9.05	1	
J151711-581354	T13	321.155	-0.613	0.006	0.31	0.36	0.38	7700	182	182	8.93	1	
J151712-570428	T13	321.769	0.368	0.021	1.17	0.60	0.38	7044	82	68	9.44	1	
J151724-580948	T13	321.215	-0.570	0.006	0.22	0.32	0.39	6615	45	45	8.65	2	
J151738-573215	T13	321.572	-0.055	0.004	0.25	0.34	0.36	6717	162	116	8.72	1	
J151754-572156	T13	321.695	0.071	0.003	0.09	0.15	0.31	8014	83	69	8.43	2	
J151758-565527	T13	321.936	0.441	0.008	0.35	0.37	0.35	6408	91	74	8.83	1	
J151805-571152	T13	321.804	0.200	0.010	0.95	0.61	0.41	5225	131	116	9.09	1	
J151830-553858	T12	322.677	1.480	0.071	12.03	2.74	0.84	1510	257	237	9.12	1	J1518-55
J151846-585113	T13	321.000	-1.250	0.016	1.61	0.85	0.53	13415	165	122	10.13	1	
J151853-584354	T13	321.078	-1.155	0.015	1.24	1.09	0.57	6034	156	116	9.33	2	two sources?
J151931-563454	T13	322.298	0.617	0.005	0.34	0.40	0.33	23422	181	161	9.92	1	
J151944-590145	T13	321.011	-1.465	0.018	1.30	1.26	0.83	5457	197	125	9.26	1	
J151946-563117	T13	322.360	0.649	0.011	1.16	0.64	0.36	5597	217	188	9.23	1	
J152008-572644	T13	321.905	-0.157	0.014	2.41	0.87	0.41	4937	219	204	9.44	1	
J152018-561112	T12	322.602	0.892	0.009	0.40	0.34	0.38	2820	81	67	8.18	1	
J152023-582036	T13	321.450	-0.932	0.009	0.48	0.52	0.43	5667	152	97	8.86	1	
J152029-574035	T13	321.821	-0.377	0.007	0.20	0.18	0.31	5448	43	27	8.45	1	
J152036-554913	T12	322.836	1.177	0.009	0.46	0.40	0.42	9477	75	47	9.29	1	
J152057-570827	T13	322.163	0.040	0.007	0.44	0.41	0.35	5549	135	135	8.80	1	
J152107-580100	T13	321.708	-0.709	0.007	0.23	0.24	0.36	5367	45	45	8.49	1	
J152120-571618	T13	322.136	-0.098	0.005	0.11	0.18	0.32	5223	45	35	8.17	2	
J152134-572049	T13	322.121	-0.178	0.009	0.99	0.56	0.38	5087	135	135	9.08	1	
J152138-561613	T12	322.713	0.721	0.011	1.62	0.78	0.39	7385	256	221	9.62	1	
J152228-573544	T13	322.087	-0.453	0.006	0.45	0.43	0.36	10859	184	184	9.39	1	
J152240-575642	T13	321.919	-0.760	0.012	1.69	1.11	0.42	5374	441	101	9.36	2	two sources?
J152245-573047	T13	322.165	-0.405	0.005	0.17	0.20	0.31	5645	89	65	8.41	1	
J152306-575237	T13	322.006	-0.735	0.008	0.55	0.42	0.36	6014	169	151	8.97	1	
J152356-571756	T13	322.416	-0.313	0.007	0.49	0.43	0.33	5142	125	92	8.79	1	
J152404-583314	T13	321.740	-1.370	0.027	2.11	1.05	0.70	3389	127	113	9.06	1	
J152425-565509	T12	322.680	-0.032	0.023	4.50	1.35	0.42	5306	304	279	9.78	1	

GA-GPS galaxy catalog continued

name J2000 (1)	mosaic TXX (2)	ℓ deg (3)	b deg (4)	$S_{\rm peak}$ Jy (5)	$S_{\rm int}$ Jy km/s (6)	$\mathrm{err}_{S_{\rm int}}$ Jy km/s (7)	rms Jy km/s (8)	$V_{\rm hel}$ km/s (9)	W_{20} km/s (10)	W_{50} km/s (11)	$M_{\rm HI}$ $\log(M_{\rm HI}/M_\odot)$ (12)	flag 1/2 (13)	note
J152448-570610	T12	322.622	-0.213	0.010	0.93	0.62	0.37	6765	136	119	9.30	1	
J152450-560322	T12	323.203	0.656	0.010	0.41	0.35	0.34	7972	79	61	9.08	1	
J152502-552507	T12	323.579	1.172	0.005	0.12	0.19	0.37	16541	86	59	9.18	2	
J152528-580743	T13	322.128	-1.117	0.008	0.87	0.74	0.44	4307	238	173	8.89	1	
J152529-561620	T12	323.159	0.427	0.005	0.25	0.28	0.30	6986	181	162	8.77	1	
J152534-580047	T13	322.204	-1.029	0.013	1.14	0.70	0.43	5692	173	159	9.24	1	
J152559-570439	T12	322.770	-0.282	0.013	1.26	0.67	0.34	5330	164	143	9.23	1	
J152615-571822	T12	322.673	-0.492	0.035	1.55	0.56	0.37	6461	77	48	9.48	1	
J152622-564741	T12	322.970	-0.075	0.026	3.47	1.04	0.37	5365	205	149	9.67	1	
J152627-554910	T12	323.523	0.728	0.007	0.40	0.34	0.32	7960	136	120	9.07	1	
J152629-555608	T12	323.462	0.629	0.017	1.27	0.70	0.32	5299	174	92	9.23	1	two sources?
J152634-563346	T12	323.122	0.102	0.009	0.77	0.55	0.32	14437	358	299	9.87	1	
J152635-581313	T13	322.199	-1.275	0.007	0.14	0.23	0.50	5046	45	45	8.24	2	
J152635-574240	T12	322.485	-0.854	0.008	0.27	0.26	0.37	4913	45	45	8.48	1	
J152649-565704	T12	322.934	-0.240	0.008	1.01	0.55	0.33	6069	222	198	9.24	1	
J152700-563247	T12	323.182	0.081	0.005	0.54	0.37	0.31	14553	262	232	9.72	1	
J152722-550244	T12	324.064	1.297	0.022	2.43	1.20	0.55	2785	168	133	8.95	1	
J152734-571756	T12	322.825	-0.585	0.008	0.67	0.50	0.36	5409	171	157	8.97	1	
J152743-574825	T12	322.556	-1.018	0.007	0.20	0.21	0.36	5087	45	37	8.38	1	
J152819-572530	T12	322.836	-0.746	0.022	1.13	0.62	0.36	5383	103	58	9.19	1	
J152835-570209	T12	323.086	-0.445	0.005	0.19	0.22	0.29	5179	112	68	8.39	1	
J152900-570743	T12	323.081	-0.554	0.017	1.70	0.69	0.36	6598	178	146	9.54	1	
J152908-573340	T12	322.850	-0.920	0.017	2.05	0.92	0.36	5107	225	180	9.40	1	
J152919-565236	T12	323.259	-0.371	0.006	0.34	0.28	0.30	10374	131	94	9.23	1	
J152945-570653	T12	323.172	-0.600	0.008	0.48	0.33	0.31	4599	120	88	8.68	1	
J152950-571147	T12	323.135	-0.673	0.004	0.31	0.28	0.29	5225	214	177	8.60	1	
J153001-580438	T12	322.654	-1.412	0.025	1.27	0.95	0.73	5538	90	68	9.26	1	
J153034-554622	T12	324.027	0.441	0.006	0.64	0.54	0.33	7086	268	251	9.18	1	
J153037-554053	T12	324.085	0.512	0.056	14.65	2.20	0.41	5000	335	240	10.24	1	J1530-55
J153045-580625	T12	322.718	-1.492	0.050	3.03	1.51	0.90	4983	90	90	9.55	1	J1530-58
J153059-554628	T12	324.074	0.406	0.009	0.83	0.70	0.35	14625	314	296	9.91	1	
J153113-545247	T12	324.614	1.120	0.007	0.31	0.32	0.40	8324	91	91	9.00	1	
J153115-560152	T12	323.958	0.174	0.033	1.43	0.39	0.31	1856	39	24	8.37	1	
J153123-545518	T12	324.609	1.073	0.010	1.08	0.89	0.43	19051	235	197	10.25	1	
J153123-572009	T12	323.228	-0.908	0.011	0.67	0.50	0.35	14200	103	77	9.79	1	
J153125-555213	T12	324.069	0.293	0.022	2.39	0.79	0.38	4900	131	116	9.43	1	
J153146-574202	T12	323.061	-1.235	0.007	0.38	0.41	0.41	10426	183	168	9.28	1	
J153149-553838	T12	324.246	0.445	0.050	4.08	0.91	0.34	1466	119	85	8.62	1	J1531-55
J153151-570406	T12	323.432	-0.724	0.017	0.74	0.36	0.34	4902	45	33	8.92	1	
J153213-574659	T12	323.063	-1.338	0.017	0.62	0.49	0.48	5486	85	53	8.95	1	
J153214-560042	T12	324.082	0.111	0.006	0.84	0.57	0.32	4956	328	275	8.99	1	
J153231-563513	T12	323.783	-0.382	0.010	0.60	0.37	0.34	5372	119	91	8.92	1	
J153258-555431	T12	324.226	0.136	0.004	0.24	0.24	0.30	9828	183	167	9.04	1	
J153320-554726	T12	324.337	0.202	0.007	0.50	0.35	0.32	5033	127	109	8.78	1	
J153334-544713	T12	324.942	1.003	0.020	1.16	0.48	0.37	2691	45	45	8.60	1	
J153429-560942	T12	324.252	-0.193	0.035	4.45	0.88	0.41	2884	170	136	9.25	1	J1534-56B
J153512-564945	T12	323.944	-0.794	0.013	0.40	0.28	0.30	1400	75	47	7.57	2	
J153516-542147	T12	325.389	1.205	0.029	5.39	1.68	0.55	5696	260	240	9.92	1	J1535-54
J153520-550207	T12	325.006	0.652	0.016	0.66	0.54	0.36	2759	105	60	8.38	1	
J153525-571159	T12	323.751	-1.111	0.007	0.41	0.40	0.38	4660	128	108	8.62	1	

GA-GPS galaxy catalog continued

name J2000 (1)	mosaic TXX (2)	ℓ deg (3)	b deg (4)	$S_{\rm peak}$ Jy (5)	$S_{\rm int}$ Jy km/s (6)	$\mathrm{err}_{S_{\rm int}}$ Jy km/s (7)	rms Jy km/s (8)	$V_{\rm hel}$ km/s (9)	W_{20} km/s (10)	W_{50} km/s (11)	$M_{\rm HI}$ $\log(M_{\rm HI}/M_\odot)$ (12)	flag 1/2 (13)	note
J153529-553408	T12	324.711	0.207	0.006	0.35	0.25	0.31	5404	90	90	8.68	1	
J153537-551035	T12	324.956	0.515	0.006	0.30	0.32	0.33	7338	91	91	8.88	1	
J153542-551656	T12	324.903	0.422	0.017	0.74	0.43	0.34	15985	47	47	9.94	1	
J153601-565327	T12	323.998	-0.908	0.005	0.30	0.29	0.31	14235	130	116	9.45	1	
J153625-543228	T12	325.422	0.962	0.016	2.10	0.74	0.39	10433	225	196	10.03	1	
J153630-562544	T12	324.322	-0.572	0.087	18.00	2.03	0.43	2706	179	179	9.80	1	J1536-56
J153636-543914	T12	325.376	0.856	0.017	2.27	0.90	0.39	10394	183	165	10.06	1	two sources?
J153658-563846	T12	324.247	-0.786	0.018	3.18	1.33	0.40	5077	346	316	9.59	1	
J153712-542517	T12	325.583	0.992	0.006	0.17	0.20	0.32	21888	95	45	9.57	1	
J153728-554334	T12	324.846	-0.085	0.003	0.09	0.14	0.30	5795	72	42	8.13	2	
J153736-542754	T12	325.605	0.923	0.009	0.63	0.39	0.34	5674	90	90	8.98	1	
J153757-570048	T12	324.139	-1.163	0.008	0.26	0.27	0.38	3331	45	31	8.14	2	
J153803-544859	T12	325.450	0.600	0.005	0.17	0.16	0.26	10496	92	92	8.94	2	
J153809-571412	T12	324.029	-1.359	0.007	0.39	0.40	0.47	16201	125	101	9.67	1	
J153815-540623	T11	325.894	1.155	0.010	0.77	0.37	0.33	9192	137	137	9.48	1	
J153846-555147	T12	324.912	-0.303	0.014	1.29	0.59	0.38	5806	128	114	9.31	1	
J153848-544617	T12	325.564	0.572	0.030	3.78	0.82	0.37	2620	187	145	9.09	1	
J153853-542140	T12	325.817	0.896	0.003	0.09	0.14	0.28	21529	95	70	9.26	1	
J153921-554142	T12	325.077	-0.216	0.012	1.40	0.74	0.38	11126	265	248	9.90	1	
J153958-563531	T12	324.612	-0.988	0.026	4.25	1.32	0.46	5475	226	213	9.78	1	
J154034-540015	T11	326.228	1.035	0.012	1.17	0.53	0.38	9243	221	207	9.67	1	
J154052-564049	T12	324.658	-1.132	0.012	1.11	1.09	0.47	6201	136	136	9.30	1	
J154105-551503	T12	325.540	-0.007	0.006	0.14	0.18	0.31	6465	73	45	8.45	2	
J154108-554414	T12	325.254	-0.401	0.009	0.79	0.90	0.40	5803	163	123	9.10	2	
J154210-540421	T11	326.375	0.839	0.005	0.28	0.29	0.37	16152	172	134	9.53	2	
J154302-533100	T11	326.812	1.205	0.015	0.95	1.06	0.51	10320	247	169	9.67	2	2 interacting galaxies?
J154306-551947	T11	325.721	-0.243	0.031	2.14	0.62	0.40	5411	142	77	9.47	1	J1542-55
J154318-560902	T12	325.246	-0.913	0.006	0.53	0.45	0.37	5867	136	121	8.93	1	
J154337-555405	T12	325.432	-0.741	0.007	1.26	0.86	0.39	5698	309	278	9.29	1	
J154404-532444	T11	326.999	1.194	0.017	1.29	0.65	0.45	10415	138	129	9.81	1	
J154417-555233	T12	325.522	-0.778	0.003	0.09	0.16	0.33	10365	46	46	8.65	2	
J154419-553709	T12	325.682	-0.578	0.016	1.04	0.63	0.39	5582	114	71	9.19	1	
J154421-532457	T11	327.029	1.166	0.013	0.81	0.52	0.41	9006	137	109	9.49	1	
J154437-543819	T11	326.314	0.173	0.014	1.85	0.71	0.40	5972	267	247	9.49	1	
J154512-545328	T11	326.226	-0.078	0.027	6.70	2.07	0.45	6565	563	310	10.13	1	
J154515-561616	T12	325.388	-1.174	0.023	2.90	1.50	0.57	5479	207	162	9.61	1	J1545-56
J154519-550344	T11	326.135	-0.224	0.016	2.52	0.82	0.42	6472	217	189	9.70	1	
J154524-532812	T11	327.120	1.028	0.006	0.77	0.38	0.34	8851	319	319	9.45	2	
J154605-541402	T11	326.732	0.362	0.006	0.53	0.42	0.38	17793	320	306	9.89	1	
J154657-542632	T11	326.703	0.120	0.015	2.08	1.56	0.49	16701	209	99	10.42	2	
J154705-535808	T11	327.010	0.480	0.007	0.49	0.36	0.38	17731	235	195	9.85	1	
J154805-554958	T12	325.969	-1.072	0.007	0.48	0.47	0.40	12631	180	118	9.55	1	
J154811-560411	T11	325.834	-1.267	0.018	0.98	0.58	0.50	5264	90	77	9.11	1	
J154827-554146	T11	326.094	-0.997	0.020	2.76	1.46	0.49	10446	367	330	10.15	1	
J154843-554709	T11	326.068	-1.091	0.009	0.47	0.43	0.47	5617	90	89	8.85	1	
J154914-532948	T11	327.551	0.655	0.011	0.76	0.42	0.38	8688	127	96	9.43	1	
J154916-544124	T11	326.811	-0.282	0.007	0.37	0.31	0.40	10655	138	138	9.28	1	
J154949-532314	T11	327.688	0.686	0.015	0.55	0.33	0.35	10834	46	33	9.48	1	
J154950-560940	T12	325.956	-1.481	0.051	7.37	3.65	0.95	5256	433	403	9.98	1	
J155009-532052	T11	327.751	0.685	0.005	0.14	0.15	0.31	8860	46	46	8.72	2	

GA-GPS galaxy catalog continued

name J2000 (1)	mosaic TXX (2)	ℓ deg (3)	b deg (4)	$S_{\rm peak}$ Jy (5)	$S_{\rm int}$ Jy km/s (6)	$\mathrm{err}_{S_{\rm int}}$ Jy km/s (7)	rms Jy km/s (8)	$V_{\rm hel}$ km/s (9)	W_{20} km/s (10)	W_{50} km/s (11)	$M_{\rm HI}$ $\log(M_{\rm HI}/M_\odot)$ (12)	flag 1/2 (13)	note
J155059-541853	T11	327.242	-0.146	0.008	0.21	0.32	0.54	9080	137	30	8.90	2	
J155145-542051	T11	327.307	-0.241	0.004	0.30	0.32	0.43	16079	140	140	9.54	2	
J155205-533807	T11	327.795	0.281	0.010	0.43	0.39	0.44	10060	92	64	9.31	1	
J155249-535258	T11	327.723	0.020	0.021	1.33	0.74	0.44	5972	82	64	9.35	1	wide DH?
J155327-550850	T11	326.992	-1.016	0.032	3.83	2.21	0.60	5678	329	221	9.77	2	
J155334-544935	T11	327.207	-0.778	0.005	0.36	0.42	0.49	12576	171	85	9.42	2	
J155334-545518	T11	327.148	-0.852	0.006	5.00	2.19	0.63	12436	502	468	10.55	1	
J155431-525047	T11	328.576	0.660	0.005	0.69	0.48	0.33	6186	348	258	9.10	1	
J155440-532329	T11	328.246	0.226	0.034	8.09	1.36	0.43	6082	475	444	10.15	1	
J155442-553036	T11	326.898	-1.409	0.016	1.01	0.78	0.71	2654	121	90	8.53	2	
J155444-530556	T11	328.440	0.444	0.015	0.73	0.36	0.37	10458	46	46	9.57	1	
J155449-515951	T11	329.153	1.285	0.008	0.65	0.47	0.53	6311	226	206	9.08	1	
J155508-530514	T11	328.494	0.415	0.008	0.31	0.25	0.35	10564	78	40	9.21	1	
J155525-520823	T10	329.134	1.115	0.011	1.99	1.05	0.44	6390	264	250	9.58	1	
J155615-534711	T11	328.173	-0.228	0.012	0.89	0.60	0.47	7920	165	135	9.42	1	
J155646-522241	T10	329.139	0.800	0.007	1.23	0.93	0.39	6437	317	296	9.38	1	
J155723-522117	T10	329.225	0.758	0.024	7.35	1.94	0.43	6190	488	457	10.12	1	
J155726-514535	T10	329.616	1.206	0.015	2.84	1.95	0.52	6653	476	410	9.77	1	
J155742-530912	T11	328.746	0.117	0.007	0.18	0.21	0.38	10299	37	23	8.95	2	
J155744-535616	T11	328.243	-0.485	0.008	0.43	0.39	0.42	7711	261	218	9.08	2	
J155816-523922	T10	329.134	0.440	0.018	2.15	0.93	0.39	6080	191	145	9.57	1	
J155824-514727	T10	329.710	1.086	0.009	0.29	0.27	0.36	6179	36	23	8.71	2	
J155827-535530	T11	328.331	-0.543	0.031	6.64	1.54	0.50	5359	429	385	9.95	1	J1558-53 A
J155843-540025	T11	328.308	-0.631	0.025	3.30	1.15	0.47	5418	251	236	9.66	1	J1558-53 B
J155856-533547	T11	328.600	-0.340	0.009	0.35	0.30	0.38	16975	86	71	9.66	1	
J155857-520212	T10	329.615	0.844	0.010	1.53	0.92	0.40	6313	217	201	9.46	1	
J155905-534316	T11	328.536	-0.449	0.015	1.88	0.95	0.52	10243	355	322	9.96	1	
J155918-543608	T11	327.986	-1.139	0.025	3.40	1.59	0.58	5582	232	176	9.70	1	
J155953-530508	T10	329.039	-0.044	0.019	4.19	2.13	0.44	5542	333	276	9.78	1	
J160000-540902	T11	328.359	-0.863	0.016	0.83	0.56	0.43	5727	82	58	9.11	1	
J160117-531138	T10	329.127	-0.263	0.007	0.56	0.54	0.40	5479	127	113	8.90	1	
J160124-532600	T10	328.984	-0.456	0.013	1.75	0.79	0.41	5472	203	162	9.39	1	
J160133-532940	T10	328.961	-0.517	0.010	1.12	1.41	0.45	10417	271	204	9.75	2	
J160143-530724	T10	329.223	-0.253	0.005	0.60	0.64	0.39	5986	248	193	9.01	1	
J160211-522441	T10	329.744	0.237	0.007	0.56	0.44	0.40	6657	177	161	9.06	1	
J160220-512602	T10	330.406	0.957	0.020	2.89	1.77	0.45	5968	207	160	9.69	1	two sources?
J160234-511356	T10	330.566	1.085	0.008	1.35	0.82	0.42	10214	321	269	9.82	1	
J160307-531754	T10	329.265	-0.523	0.033	3.56	1.00	0.38	5790	157	103	9.75	1	J1603-53
J160316-511701	T10	330.614	0.974	0.011	0.56	0.38	0.36	6428	45	45	9.03	1	
J160346-512045	T10	330.632	0.875	0.013	1.79	0.99	0.38	16685	187	159	10.36	1	
J160419-513418	T10	330.545	0.651	0.011	1.36	0.63	0.35	5959	181	181	9.36	1	
J160429-514230	T10	330.474	0.531	0.012	1.04	0.72	0.38	8688	182	147	9.57	1	
J160502-523119	T10	329.996	-0.132	0.007	1.07	0.62	0.37	14462	221	187	10.01	1	
J160508-523621	T10	329.952	-0.205	0.013	1.56	0.98	0.40	6038	181	152	9.43	1	
J160511-514636	T10	330.510	0.408	0.017	3.03	1.78	0.42	16883	262	218	10.59	1	
J160523-522354	T10	330.119	-0.076	0.008	1.34	1.01	0.40	6177	359	326	9.38	1	
J160547-511331	T10	330.946	0.757	0.017	4.48	2.18	0.44	5716	383	334	9.84	1	J1605-51
J160623-532430	T10	329.556	-0.928	0.010	0.70	0.45	0.36	5891	110	80	9.06	1	
J160625-502618	T10	331.547	1.275	0.010	1.70	1.94	0.59	16152	187	187	10.31	1	
J160648-525135	T10	329.971	-0.564	0.009	0.47	0.40	0.35	5692	77	57	8.86	1	

GA-GPS galaxy catalog continued

name J2000 (1)	mosaic TXX (2)	ℓ deg (3)	b deg (4)	$S_{\rm peak}$ Jy (5)	$S_{\rm int}$ Jy km/s (6)	err$_{S_{\rm int}}$ Jy km/s (7)	rms Jy km/s (8)	$V_{\rm hel}$ km/s (9)	W_{20} km/s (10)	W_{50} km/s (11)	$M_{\rm HI}$ $\log(M_{\rm HI}/M_\odot)$ (12)	flag 1/2 (13)	note
J160710-514941	T10	330.704	0.164	0.013	1.35	0.76	0.45	5929	201	137	9.35	1	
J160722-534156	T10	329.469	-1.242	0.012	1.10	0.69	0.53	5665	130	108	9.22	1	
J160728-503429	T10	331.581	1.061	0.008	0.75	0.79	0.44	6371	147	90	9.15	2	
J160732-534914	T10	329.406	-1.349	0.039	6.95	3.43	0.76	5483	342	265	9.99	1	J1607-53
J160736-523311	T10	330.266	-0.417	0.009	0.47	0.45	0.38	14404	46	46	9.65	1	
J160744-530122	T10	329.965	-0.779	0.011	2.08	0.87	0.37	5667	313	292	9.50	1	
J160747-522509	T10	330.377	-0.338	0.005	0.54	0.39	0.36	5637	135	135	8.90	1	
J160748-510447	T10	331.280	0.652	0.054	8.71	2.09	0.52	6036	212	181	10.17	1	J1607-51
J160756-504534	T10	331.511	0.875	0.013	1.43	0.99	0.47	5825	172	158	9.36	1	
J160802-505204	T10	331.449	0.785	0.009	0.97	0.76	0.45	6287	135	115	9.25	1	
J160855-530935	T10	330.003	-0.999	0.017	3.70	1.54	0.40	10464	321	313	10.27	1	
J160912-501849	T10	331.960	1.068	0.034	3.80	1.33	0.48	6450	158	121	9.87	1	
J160927-504618	T10	331.680	0.704	0.011	3.50	2.03	0.49	5740	497	491	9.74	1	
J160937-501628	T10	332.035	1.053	0.014	2.27	1.97	0.51	14565	307	150	10.34	1	
J160942-503332	T10	331.853	0.833	0.015	2.28	0.87	0.41	6384	177	162	9.64	1	
J160957-515226	T10	330.991	-0.160	0.006	0.21	0.23	0.39	5865	45	31	8.54	2	
J161003-525106	T10	330.339	-0.889	0.010	1.64	1.28	0.40	14207	371	335	10.18	1	
J161008-501124	T10	332.152	1.059	0.032	5.68	2.64	0.58	6245	222	184	10.02	1	J1609-50
J161037-511135	T10	331.528	0.270	0.006	0.48	0.52	0.48	5394	149	101	8.82	1	
J161124-502402	T10	332.158	0.767	0.008	0.50	0.39	0.42	9349	137	115	9.31	1	
J161246-524516	T10	330.705	-1.097	0.025	2.80	1.26	0.45	5678	155	114	9.63	1	J1612-52
J161431-521457	T10	331.246	-0.913	0.009	0.93	1.06	0.42	10614	242	63	9.69	2	
J161530-521221	T10	331.384	-0.985	0.010	1.01	0.88	0.44	5641	194	143	9.18	1	
J161622-520039	T10	331.615	-0.937	0.009	0.42	0.36	0.39	5153	84	69	8.72	1	
J161711-521634	T10	331.520	-1.214	0.019	2.76	1.72	0.60	5153	203	167	9.54	1	
J161741-520101	T10	331.758	-1.084	0.014	1.05	1.00	0.44	5232	119	89	9.13	1	
J161833-520837	T10	331.764	-1.267	0.017	2.51	1.82	0.58	10995	230	230	10.15	1	

[1]Consists of a galaxy A ($V_{\rm hel} \simeq 16\,483 - 16\,532$ km/s), which could be a close pair, plus an offset neighbour B ($V_{\rm hel} \simeq 16\,928$ km/s).

[2]Special case: very extended on-sky. The dispersed emission does not appear clear in the moment maps.

GPS Atlas

The first four entries of the GPS atlas. The images are in ascending order of RA, going down the columns. The full atlas is available on Google Drive:
https://drive.google.com/drive/folders/16g0frJHkbDKLOB1_2lMqhn5qwqbOxM4X?usp=sharing .

Left panel: moment-0 map in Galactic coordinates, with a 3σ-contour — measured in the corners of the map (this value is also displayed in the top-right), the unique name in the top-left, the beam size in the bottom-left, and a scale-bar measuring 10 kpc in length (bottom-center). Middle panel: moment-1 in Galactic coordinates, with contours spaced $44.1\,\mathrm{km\,s^{-1}}$ (one spectral channel) apart, and the heliocentric velocity in the top-right. Right panel: HI profile showing the line widths at 20% and 50% (as measured by SoFiA) in the top right.

Figure B3: GPS Atlas Extract